Correlating Rapid Solidification Microstructure Morphology and Mechanical Properties in Hypo-eutectic Al-Cu Alloy

by

Mohammed Tariq M Alamoudi

B.S. in Mechanical Engineering, King Abdulaziz University, 2010

M.S. in Materials Science and Engineering, Lehigh University, 2017

Submitted to the Graduate Faculty of the

Swanson School of Engineering in partial fulfillment

of the requirements for the degree of

Doctor of Philosophy

University of Pittsburgh

2022

UNIVERSITY OF PITTSBURGH

SWANSON SCHOOL OF ENGINEERING

This dissertation was presented

by

Mohammed Tariq M Alamoudi

It was defended on

May 25, 2022

and approved by

M. Ravi Shankar, Ph.D., Professor, Industrial Engineering

Guofeng Wang, Ph.D., Professor, Mechanical Engineering and Materials Science

Tevis DB Jacobs, Associate Professor, Mechanical Engineering and Materials Science

Dissertation Director: Jörg M.K. Wiezorek, Ph.D., Professor, Mechanical Engineering and Material Science

Correlating Rapid Solidification Microstructure Morphology and Mechanical Properties in Hypo-eutectic Al-Cu Alloy

Mohammed Tariq Alamoudi, PhD

University of Pittsburgh, 2022

Scanned laser melting (SLM) and subsequent re-solidification results in the formation of solidification microstructures that form under continuously changing conditions.

This study aims to advance our understanding of the mechanical properties and plastic deformation behavior for the non-equilibrium multiphase microstructures that can be accessed by Al-10at.%Cu hypo-eutectic alloy during rapid solidification (RS) after SLM. We combined nanoindentation with microstructural analyses by SEM and TEM to study processing-microstructure-property relationships. At low scan laser velocity (V_L=3mm/s), a microstructure gradient develops as the solidification rate (V_{SL}) increases from initially V_{SL}=0mm/s at the bottom to a maximum of $V_{SL}\approx V_L$=3mm/s at the top of the melt pool. The cellular α-Al(Cu), located centrally in the melt pool, consistently showed Cu-solute supersaturation by 20% relative to the equilibrium solid solubility limit of ~2.5at% and exhibited 36% hardness increase relative to the α-Al(Cu) in the as-cast state. The experimentally observed solute trapping in the α-Al(Cu) cells of the RS microstructure was found to be consistent with predictions from solidification theory using a cellular/dendritic growth model.

By increasing V_L to higher scan velocities, i.e., 1m/s≤V_L≤4ms, the maximum solidification rates achieved during RS of the alloy melt pools increase accordingly to the m/s range. At these large solidification rates different microstructure morphologies are revealed. They included columnar grain morphologies with continuous θ-Al_2Cu, columnar grains with discontinuous θ/θ'-Al_2Cu and banded morphology region. The nanoindentation of these characteristic RS

microstructure morphologies revealed hardness increases relative to α-Al in the as-cast state (1.1GPa) and the supersaturated cellular primary α-Al(Cu) (1.5GPa) observed for RS microstructures after scanned laser melting at low scan speed (V_L=3mm/s). Hardness values of up to 3.32GPa and 2.98GPa have been determined for the columnar grains with continuous θ-Al_2Cu and discontinuous θ'-Al_2Cu, respectively. The banded region showed hardness values between 2.95 to 3.35GPa.

Isothermal annealing of the RS microstructures obtained after scanned laser surface melting at scan speeds of 2m/s and 4m/s at temperatures of 180˚C, 230˚C and 280˚C showed transformations with rapid kinetics establishing unusual populations of second phase Al_2Cu related particles with fine scale and high density. The mechanical property evolution for morphologically distinct regions in the alloy microstructure during annealing has been determined.

Table of Contents

List of Tables

List of Figures

Preface

In the beginning, I would like to express my ultimate appreciation to my parents for their continues support and prayers during my study aboard. Also, I would like to extend special thanks and appreciations to my lovely wife for her endless support and patience all the time.

I would like to express my deepest gratitude to my advisor Professor Jörg Wiezorek for his unconditional support, gaudiness and extreme patience during my Ph.D. study who made this possible. Also, I would like to thank my committee members Professor M. Ravi Shankar, Professor Guofeng Wang and Professor Tevis Jacobs for their constructive feedback and comments. Further, I would like to thank the staff of MMCL and NFCF, especially, Dr. Rocco Cerchiara, Dr. Erica Erickson and Dr. Daniel Lamont for helping out in my experiments. I, also, would like to thank my colleagues; Dr. Bathula Vishwanadh, Mr. JaeHyuk Jo and Mr. Yuzhe Liu for the scientific discussion, collaboration and good times I had with them.

Parts of this work received support from the National Science Foundation, Division of Materials Research, Metals & Metallic Nanostructures program through Grant No. DMR 1607922 award number NSF.

Finally, an extended thanks my employer King Abdulaziz City for Science and Technology (KACST) for providing the financial support that was essential to complete my Ph.D. Degree.

1.0 Introduction

Solidification processing under extreme conditions, i.e., rapid solidification (RS), is a phase transformation process driven far away from equilibrium by large undercooling. In multicomponent alloy systems RS typically leads to the phenomenon called solute trapping, effectively extending solid solubility limits beyond equilibrium prediction, formation of metastable phases, and microstructure scale refinement, as well as microstructure morphology changes. Laser surface remelting (LSM) is an effective way to impart RS to materials. In LSM rapid heating and cooling rate can be accomplished, and novel microstructures can be produced. In LSM, laser irradiation of a spot on the surface of a material substrate by a laser pulse or a continuously moving laser source melts the surface region. The melted surface layer can range in dimensions from single to hundreds of micrometers in depth into the bulk metal substrate. The un-melted bulk material acts as heat sink to ensure rapid heat extraction from the melt, and to seed the growth of the solidification products [1]. Rapid solidification by LSM or any other means is an active research field [1]. Most previous studies are focused on studying the microstructure evolution and/or development of predictive models [2]–[7]. Different alloys systems have been investigated, such as Al-Cu [2], [6], [8], [9], Ag-Cu [10], Al-Li-Cu [11], Si-As [12] and multi-component concentrated alloys [13]. Al-Cu alloy has been extensively studied and served as textbook alloy for which excellent reference data of thermophysical and microstructural data exists. Using Al-Cu binary alloys on the Al-rich side of the phase diagram, i.e., between Al and Al_2Cu, which represent a typical eutectic system and have served as models for precipitation hardening alloys with a multiphase microstructure, prior studies of the microstructure formation

and the effects of laser power and speed have been performed [3], [9], [14], [15]. For instance, some studies focused on the morphologically lamellar eutectic microconstituent regarding effects of LSM conditions on scale refinement and the influence on overall mechanical properties [3], [9], [14], [15]. Increasing the solidification velocity has direct effect on the microstructure evolution. Gill and Kurz constructed a solidification microstructure selection map for the Al-Al_2Cu system [16]. The solidification morphology of eutectic alloys in the Al and Al_2Cu system changes as growth rate increased from that of a regular lamellar eutectic to a wavy lamellar eutectic and then at highest rates to banded morphology region [16]. In alloys of off-eutectic compositions, hypo-eutectic and hyper-eutectic, the resulting solidification microstructures are expected to comprise a solid-solution phase as primary microconstituent and the eutectic as a secondary microconstituent. As has been shown in prior studies of off-eutectic alloys, RS microstructures can exhibit multiphase microstructures with a range of morphologies and scales [3]. Using laser melting prior studies of RS in off-eutectic Al-Cu has been shown to enable extreme supersaturations in the primary α-Al phase, as well as formation of unique multiphase microstructures comprising metastable phases with unusual morphology and highly refined scale and extreme density. It has been reported that the solid/ liquid interface velocity (v_{SL}) during solidification has direct relation with microstructure morphologies transition [3]. The morphology of the solid-liquid interface or the growth mode changes from planar to cellular, cellular to dendritic, dendritic to cellular, and cellular to planar, as V_{SL} increased. When the V_{SL} in Al-11 at.% Cu alloy reaches the critical value of the velocity of absolute stability, V_a= (0.80±0.05) m/s, transition from coupled two-phase growth to the single-phase growth occurred in this hypoeutectic alloy [3]. A recent study [17] has investigated the total effect of rapid solidified Al–Al_2Cu eutectic on mechanical properties. Here the mechanical properties were measured by in situ micro-pillar compression testing in SEM. At

20 nm interlamellar spacing, the maximum flow strength reached 1.63 GPa and compression plasticity increased by 17.9% compared to as-cast Al–Cu eutectic alloy [17]. Notably, regular lamellar eutectic with an interlamellar spacing of 17nm has been reported as the minimum scale that can be achieved in Al-Cu alloys. The formation of lamellar eutectic is a diffusion limited solidification microstructure morphology. This implies that a maximum solidification rate exists at which the minimum scale lamellar eutectic is established in Al-Cu. Assuming eutectic solidification at T≈821K (548˚C) with a lamellar wavelength λ=20nm, literature data for diffusion of Cu in liquid Al give a diffusion coefficient of $D_L(Cu) \approx 3.15x10^{-9}$ m^2/s [18] and therefore a maximum growth rate of v=D/(λ)= 0.16 m/s ≈ 0.2m/s. At solidification rates that exceed this critical value for the regular lamellar eutectic changes to irregular eutectic morphologies, e.g., wavy, are expected since solute diffusion can no longer establish local equilibrium at the solid-liquid interface [16]. Under conditions driven sufficiently far away from equilibrium during the RS, off-eutectic and even eutectic composition alloys will reach different critical interface velocity magnitude, the composition dependent velocity of absolute stability. Then the transition from the coupled two-phase growth of α-Al-phase and Al_2Cu-phase to single-phase growth of the maximally supersaturated α-Al-phase is predicted [16]. While the effects of scale refinement achievable in eutectic Al-Cu for regular lamellar morphology eutectic microstructures on the mechanical properties have been determined, the mechanical properties of the irregular eutectic microstructures forming for super-critical RS interface velocities beyond that achievable for regular lamellar eutectic remain unknown. Similarly, for the more complex range of morphologies and scales of the RS microstructures obtaining in binary Al-Cu alloys with off-eutectic compositions, to date detailed understanding and experimental data on mechanical properties is lacking.

In addition to solidification microstructure selection maps for the Al-Cu system as a function of solidification rate and alloy composition, knowledge of the associated mechanical properties would be useful. Establishing processing-microstructure-property relationships would then be possible for a given alloy composition in the Al-Cu system. In this study, the hypoeutectic Al- 10at%Cu (Al-10Cu) is utilized to locally investigate the mechanical properties of morphologically distinct non-equilibrium microstructures that can be established during RS for solidification rates sufficient to induce the banded region morphologies. The Al-10Cu hypoeutectic composition gives rise to approximately equal fractions of primary α and eutectic microconstituents. The effects of the increased solidification rates on both the eutectic lamellar refinement and on the primary α-Al-phase from can be ascertained. The eutectic can then act as an internal standard for comparison with the recent published work, like the work done by using the micropillar compression testing experimenters, to elucidate the mechanical properties of eutectic microconstituent [15], [19]. The role of the non-equilibrium features established in the RS microstructure morphologies of Al-Cu alloys have not been studied regarding the mechanical properties. Using the Al-10Cu alloy the mechanical properties of RS microstructures developing for solidification rates beyond the 0.2m/s for the then no-longer lamellar eutectic microconstituent and even for solidification rates associated with interface migration for v⩾ velocity of absolute stability can be investigated. The focus of this study will be the determination of relationships between the mechanical properties with the solidification conditions that allow the solidification rates to reach the maximum ranges of critical interface velocities associated with the changes between the different alloy RS microstructure morphologies, such as the α-cells, banded region and α-phase plane front [16].

1.1 Hypotheses

The following major hypotheses will be evaluated:

1) The strengthening behavior in the concentrated supersaturated α-Al (Cu) with Cu concentrations ≥ ≈4at.% Cu will significantly differ from the prediction of the existing scaling law for solute strengthening in dilute α-Al solid solution alloys, i.e., for solute concentrations ≤ ≈2 at.% Cu.
2) The mechanical properties of the non-equilibrium multi-phase microstructure region of the columnar grains of α-cells and the banded region will change with the scale of the distributions and morphology of the secondary Al_2Cu related phases and can be compared with scaling laws for strengthening established for regular lamellar α-Al/θ-Al_2Cu eutectic.
3) Solidification microstructure selection maps, which describe the relationships between the local solidification interface velocity and associated interfacial supercooling with the resulting solidification microstructure morphology, for Al-xCu alloys, where x≤≈33at.%Cu, can be extended to include the mechanical properties of the respective RS alloy microstructures by selective local mechanical property measurements using nanoindentation and accompanying SEM imaging.

To investigate these hypotheses, different evaluation steps need to be taken. The formation of the rapid solidification microstructure can be addressed via laser surface melting (SLM) using the powder-bed SLM system EOS DMLS M290. To evaluate the hypotheses, it is necessary to study the effect of the scale within the morphologically distinct non-equilibrium rapid solidification microstructures on mechanical properties. To obtain mechanical property measurements on the respective relevant microstructural length scale of one to two micrometers

here nano-mechanical testing by instrumented indentation will be performed at room temperature using the Triboindenter, Hysitron TI900 system. Spatial arrays or nanoindentation matrices will be created for select and representative regions in the RS microstructures. Post-indentation imaging will be obtained by SEM. This permits direct correlation of the specific locations within the scale refined RS microstructures with the indentation and associated measurements. As a result, locally resolved and observation-based and -verified relationships between the microstructure microconstituent and mechanical properties will be determined. To examine the effects of the scale and nature of the Al_2Cu-based population of second phases (i.e., θ' and θ) in RS microstructure annealing of the RS microstructure at different isotherm will be conducted. Then, applying nanoindentation hardness measurement enables analysis of the effect of changes in the Al_2Cu-based population of second phases on mechanical properties. Past research has shown that metastable phase particulates in the α-Al cells have structural characteristics (elastically strained coherent and semi coherent interfaces, tetragonal chemically ordered crystal structure) that suggest that it would be reasonable to expect them to exhibit the characteristics of strong obstacles for dislocation glide. Subsequent TEM studies can be conducted using site-selective extraction of specimens to reveal the nature of the interactions between gliding dislocations and the respective obstacle particles, i.e., to distinguish between dislocation morphologies consistent with a by-passing (bowing, Orowan) behavior and those associated with shearing (cutting) behavior (Due to experimental difficulties, time and financial constraints imposed by the project budget, it was not possible to include the TEM experimentation here as part of this dissertation). Results from the nano-mechanical measurements, associated SEM imaging, and heat treatment studies would support the evaluation of hypothesis 2, hypothesis 3 and hypothesis 4, albeit for the later only for the selected Al-10Cu alloy composition.

1.2 Research Objectives

The aim of this study is to advance our understanding of the mechanical properties of the morphologically different and alloy specific characteristic non-equilibrium multiphase microstructures that can be accessed by multicomponent alloys in the Al-Cu system during RS. The proposed research will utilize a model alloy system, namely, Al-10Cu hypo-eutectic alloy to enable comparisons with existing literature [3], [15], [17]. The mechanical properties associated with the morphologically distinct non-equilibrium microstructures that characteristically develop in hypo-eutectic Al-Cu alloys at composition dependent critical values of the solidification rate remain to be ascertained. The correlation between the changes in the morphology and scale of the solidification microstructure and properties will be explored by location specific and spatially resolved mechanical property measurements. Objectives of this study include the following items:

1. Demonstrate the feasibility of producing non-equilibrium solidification microstructure via scanned laser surface melting for hypo-eutectic Al-10Cu alloy.
2. Establish the different types of characteristic morphologies of RS microstructures that develop at certain solidification speed in Al-10 at% Cu hypo-eutectic alloy up to banded morphology grains forming at the transition from two-phase to single-phase growth, i.e., when the non-equilibrium solute partition coefficient approaches unity.
3. Demonstrate the feasibility of measuring the spatially resolved mechanical properties of different morphological regions of the RS microstructure by using nano-indentation tests.

4. Establish locally correlation between the solidification conditions (e.g., solidification rate, V_{SL}) relative to microstructure scale and morphology and the associated mechanical properties.
5. Develop understanding of the plastic deformation behavior of supersaturated solid solution α-Al(Cu) and other metastable phases present in Al-10Cu alloy after RS on the mechanical properties using the hardness values obtained nano-indentation.
6. Determine the changes of the non-equilibrium RS microstructure morphologies in the Al-10Cu alloy during iso-thermal annealing and ascertain their affects to the mechanical properties.

1.3 Future Impact

Establishing ideally quantitative correlations between the respective features and metrics of the morphologically distinct regions that develop in the RS microstructure of Al-Cu alloys for a range of solidification rates is of merit because it facilitates development of relationships between the RS processing conditions with the respective microstructure and associated properties. Essentially, solidification microstructure selection maps (SMSM) can then be extended to include the relationship to properties. Performing scanned laser surface melting experiments for a large range of laser scan speeds allows an assessment of the role of the solid substrate microstructure on the constitutional effects and compositional mixing in the transient liquid state on the development of RS microstructure. This has implications for the behaviors related to compositional mixing in the melt pool during for example SLM additive manufacturing and laser joining. Single laser traces

performed at fast laser scan velocity are associated with short durations of the transient liquid state and the RS microstructure can be affected by composition inhomogeneity. The resulting RS microstructure formation is no longer strictly determined only by the thermal field encountered by the growing solid and local variations in the composition fields become an important factor. In the additive manufacturing, much research interest is dedicated to characterizing the melt pool behavior powder bed SLM and e-beam selective melting. The powder particles sizes are typically in the range of 10 ~ 50 μm, and each particle has slightly different composition, i.e., the smaller particles cool faster than bigger ones. In SLM powder bed AM the melt pool is typically about 250μm wide and 150 deep, i.e., about 15~20 particles across and 8~12 particles deep. After a single laser trace, depending on the scan speed and laser power and material used, differences from compositionally different particles could persist in the resolidified microstructure. While such differences in the microstructure of AM alloy components is usually undesirable and avoided or mitigated via post-solidification treatments, if these differences where better understood and controlled, it could open future opportunities for deliberate exploitation and gradient microstructure formation in components with complex geometries and greatly varying external dimensions.

Aside from contributions to expand the basic scientific understanding and knowledge of relationships between the non-equilibrium multiphase RS microstructure morphologies in hypoeutectic Al-10Cu and related alloy systems and the respective mechanical properties, this work could, also have an impact on the surface remelting technologies. For example, understanding processing conditions influence on the resulting microstructure and properties in alloy surface remelting can be useful to improve locally pitting corrosion in Al alloys or fatigue and potentially tribological performance. One way to improve pitting resistance is by refining the

microstructure. Based on the substrate microstructure scale, morphology and alloy composition suitable laser scan velocity and schema can be used for tailored mechanical properties of the new surface.

2.0 Background and Literature Review

During near-equilibrium solidification under slow cooling, the as-cast microstructure of the hypoeutectic Al-10 at% Cu alloy formed primary α-Al solid solution dendrites as the melt temperature crossed the liquidus line, and the remnant liquid transformed into regular lamellar eutectic when the melt undercooled just below eutectic temperature. However, for rapid cooling under conditions of rapid solidification (RS), the microstructure shows different microstructure scale, morphology transitions and composition changes relative to the as-cast state. During rapid growth of hypoeutectic (off-eutectic) Al-10Cu after scanned laser surface remelting the microstructure evolution is controlled by the epitaxial growth that is seeded by the as cast substrate. Nucleation of solid is not necessary but still possible. The rapid cooling via heat extraction from the liquid melt through the solid-liquid interface into the massive solid substrate results development of highly undercooled liquid adjacent to the solid alloy and produces a steep acceleration of the solidification interface migration rate, its velocity. Interface velocity dependent transitions of the growth modes from planar to cellular, cellular to cellular/dendritic growth, and then from dendritic to eutectic-cell growth are expected to occur [3], [14]. These growth mode transitions lead to changes in the morphology and scale of the resulting rapid solidification microstructure.

This chapter provides some general background on Al-Cu system and relevant strengthening mechanisms for age-hardening Al-Cu alloys in section 2.1. In section 2.2 background information related to the effect of deviation from equilibrium to non-equilibrium solidification on microstructure evolution is presented. Subsequently, the microstructure

morphology developing during rapid solidification for hypoeutectic alloys of the Al-Cu binary system will be reviewed in section 2.3. Lastly, section 2.4 discuses some prior research studies that have used nanoindentation techniques to examine the mechanical properties in metals with a focus on Al alloys.

2.1 Aluminum Copper Alloy System

Aluminum (Al) is one of the most abundant metallic elements accessible on earth and the second most after iron in terms of industrial production tonnage. Aluminum alloys are used in many industrial fields, such as automotive, aeronautical and aerospace industries, as well as electrical and electronic technologies, due to its unique properties. Aluminum alloys offer a high strength to weight ratio, excellent thermal and electrical conductivity, and outstanding corrosion resistance. Among wrought and castable aluminum alloys two main classes are distinguished. Namely, first, heat treatable alloys, also known as age-hardening alloys, which can be strengthened via precipitation of intragranular/ and or intergranular phases and, second, alloys that are not heat treatable, which are also known as solid solution strengthened alloys and cannot be strengthened via precipitation [20]. The latter class of alloys can be strengthened by cold working [20].

Commercial aluminum alloys have complex multicomponent compositions containing at least two major solute elements and often several additional minor solute elements. In basic research often simplified compositions are used as model alloys to evaluate the effects of the principal alloying additions and possible interplay between solute elements during solid-liquid and solid-state processing. The binary Al – Cu alloy is a classic example of a model system for heat

treatable aluminum alloys and can undergo precipitation hardening or strengthening [21]. Figure 1 shows the Al-Cu phase diagram and an enlarged section of the Al-rich side. Cu has maximum solid solubility of 5.65 wt.% (2.48 at%) at 548 oC but only 0.04 wt.% Cu (0.02 at.%) dissolves in Al at room temperature (RT). Most commercial alloys based on the Al-Cu system contain less than about 2 at.% Cu solute and can be considered a-Al(Cu) solid solution alloys. Al-Cu alloys with Cu solute content in the range of 2.48 at.% (5.56wt.%) < XCu < 17 at% (33wt%) are considered hypo-eutectic alloys. Rapid cooling of Al alloys with solute fractions of Cu < 5.65 wt% to 20˚C, i.e., room temperature (RT), after solutionizing heat treatments at temperatures above the solvus and below the solidus, typically in the vicinity of 450˚C to 550˚C, results in formation of supersaturated solid solutions of alpha-Al (SSSS) without forming of the equilibrium θ-Al2Cu phase (see dashed vertical line in Fig. 1b). While the SSSS alloy is thermodynamically unstable at RT, the rapid quenching is capable to prevent the nucleation of the secondary θ-Al_2Cu phase precipitates. This indicates that the nucleation barrier for θ-Al_2Cu phase precipitation is significant. This is consistent with the high interfacial free energy of the incoherent interfaces between the Al matrix lattice and the chemically ordered intermetallic θ-Al_2Cu phase, which has a tetragonal crystal structure [21]. During natural aging, e.g., at RT, of the rapidly quenched Al (SSSS) the excess vacancy concentration facilitates solute Cu atoms diffusing to form Guinier-Preston (GP) zones within days to weeks depending on the exact alloy composition, solutionizing temperature and quenching rate. Increasing the temperature for aging treatments to intermediate levels within the two-phase field for α-Al and θ-Al_2Cu (Figure 1), metastable phase precipitates start forming. Eventually, at sufficiently long times of such artificial aging treatments the thermodynamically stable θ-Al2Cu phase forms [22]. The full sequence of precipitation of intermediate and eventually the stable phases in the Al-Cu system is described as [21]:

SSSS ➔ solute cluster ➔ GP1 ➔ GP2 (θ") ➔ θ' ➔ Al_2Cu (θ)

To observe the full sequence of precipitation the aging temperature has to be below the solvus temperatures for the respective intermediate phases [21].

For hypoeutectic alloys with Cu% in the range of 2.48 at.% (5.65wt.%) < X_{Cu} < 17.5 at% (33.3wt%), e.g., Al-10at.%Cu (~22wt.%Cu), solidification under near-equilibrium conditions results in the formation of a primary solidification product of α-Al(Cu) solid solution and a secondary solidification product of eutectic comprised of α-Al(Cu) and θ-Al_2Cu (Figure 1). The evolution of the primary product is essentially equivalent to that of the solid α-Al(Cu) forming in solid solution alloys with Cu content below 2.48 at.% (5.56wt.%), with the initial liquidus and solidus depending on the alloy composition. Note that the liquidus of hypoeutectic Al-Cu alloys decreases as Cu fraction increases from about 923K (650˚C) to 821K (548˚C) at the eutectic composition (Figure 1). The fraction of the secondary solidification product, the eutectic microconstituent of the solidification microstructure, increases as Cu concentration increases for the hypoeutectic alloys (Figure 1).

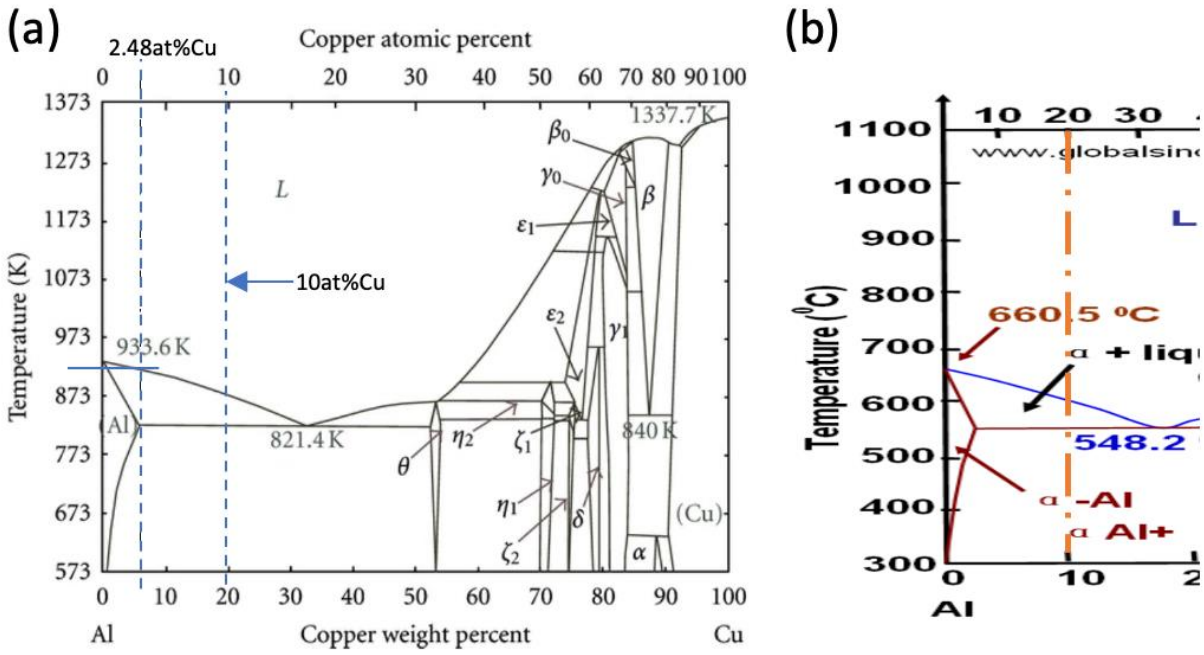

Figure 1: a) standard Al-Cu phase diagram, b) an enlarged section of the Al-rich side [23]

2.1.1 Strengthening Mechanisms in Al-Cu System

Supersaturated solid solution (SSSS) can be formed by rapidly cooling of an age-hardening alloy, e.g. Al-4.5 wt.% Cu, equivalent to about Al-2.0 at.% Cu. As a result of the rapid cooling from a solution treatment temperature in the vicinity of the eutectic isotherm, an excess concentration of vacancies is preserved in the as-quenched state at room temperature. These excess concentrations of vacancies help in nucleation processes required to initiate precipitation reactions to form the various possible intermediate phases (see previous section). Carling, Karin, et al. [24] estimated the vacancy concentration at 550ºC in Al-Xat.%Cu alloys to be ≈0.01 per Cu solute atom. This is equivalent to 1 vacancy per 100 solute atoms and corresponds to a vacancy concentration, $x_V \approx 2x10^{-4}$ for Al-2at.%Cu. The equilibrium vacancy concentration reduces to about $x_V \approx 1x\ 10^{-10}$ as the temperature drops to 20˚C, RT. Thus, quenching from 550ºC to RT can

be used to establish a huge excess of vacancies relative to the equilibrium state. Aided by the excess vacancy concentration solute Cu atoms in the supersaturated solid solution state can form solute atom clusters at RT (natural ageing), which reduces the Gibbs free energy of the supersaturated alloy by eliminating excess vacancies. Clusters are defined as homogenous decomposition (local aggregation) of alloying atoms without a detectable structure or ordering [25]. These solute clusters cause mechanical hardening or strengthening of the alloy. In the Al-Cu system, solute Cu atoms are smaller than the host lattice Al atoms. They are causing local strains in Al matrix lattice and resulting solute hardening (strengthening). Solute hardening increases strength due to an elastic interaction of the solute atoms with the slip accommodating dislocations, resulting in local pinning events, which hinder the glide motion of dislocations in the glide plane. Thus, the energy barrier for dislocation mobility increases and an incrementally increased resolved shear stress is required to move the dislocations to achieve plastic deformation as the density of these pinning obstacles increases [25]. The potency of the substitutionally incorporated solute elements, e.g., Cu in Al alloys, for strengthening is primarily related to the atomic size misfit relative to the host lattice atoms. The total magnitude of the strength increment scales typically linearly or nearly linearly with the solute concentration [26].

The precipitation sequence in age-hardening Al-alloys is affected by the solute amount, the ageing temperature and the addition of other trace elements. Figure 2 shows the metastable solvi of the Al-rich end of the Al-Cu phase diagram [21] and schematic depictions of the unit cells of the fcc Al and the Alx-Cu related precipitate phases [27]. In Al-Cu SSSS, i.e., at appropriate aging time and temperature, GP1 zones start forming as the first metastable phase in the precipitation sequence since they required the smallest activation energy to nucleate. The GP1 zone structure in Al-Cu system is a layer of Cu atoms replace Al atoms in a region of the $\{100\}_{\alpha}$ planes. The next

step in the precipitation sequence is the formation of GP2 zones (θ″). θ″ precipitates consist of two or more Cu planes in parallel $\{001\}_\alpha$ separated by three atomic layers of Al. They have an Al_3Cu composition and a tetragonal structure (a = 0.404 nm and c = 0.768 nm). θ″ precipitates have an orientation relationship with the aluminum matrix such that $(001)_{\theta''}//(001)_\alpha$ and $[100]_{\theta''}//[100]_\alpha$. GP1 and GP2 are fully coherent with the Al matrix. The next step in the precipitation sequence forms θ′ phase, which has tetragonal structure with Al_2Cu composition. It has full coherency with Al matrix in their broad basal plane surface and semi-coherency with the prismatic side surfaces. Relative to the Al lattice, θ′-phase extends into two Al cells with only 6 atoms. Thus, the phase transformation from θ″- to θ′-phase involves replacement of two Al atoms by Cu and two more by vacancies. This means that formation of θ′-phase required involvement of vacancies and lattice diffusion of Cu. The final stage in the precipitation sequence is the formation of equilibrium θ-phase. It is incoherent with Al lattice and has Al_2Cu composition with body-centered tetragonal structure [21], [22], [28] (Figure 2).

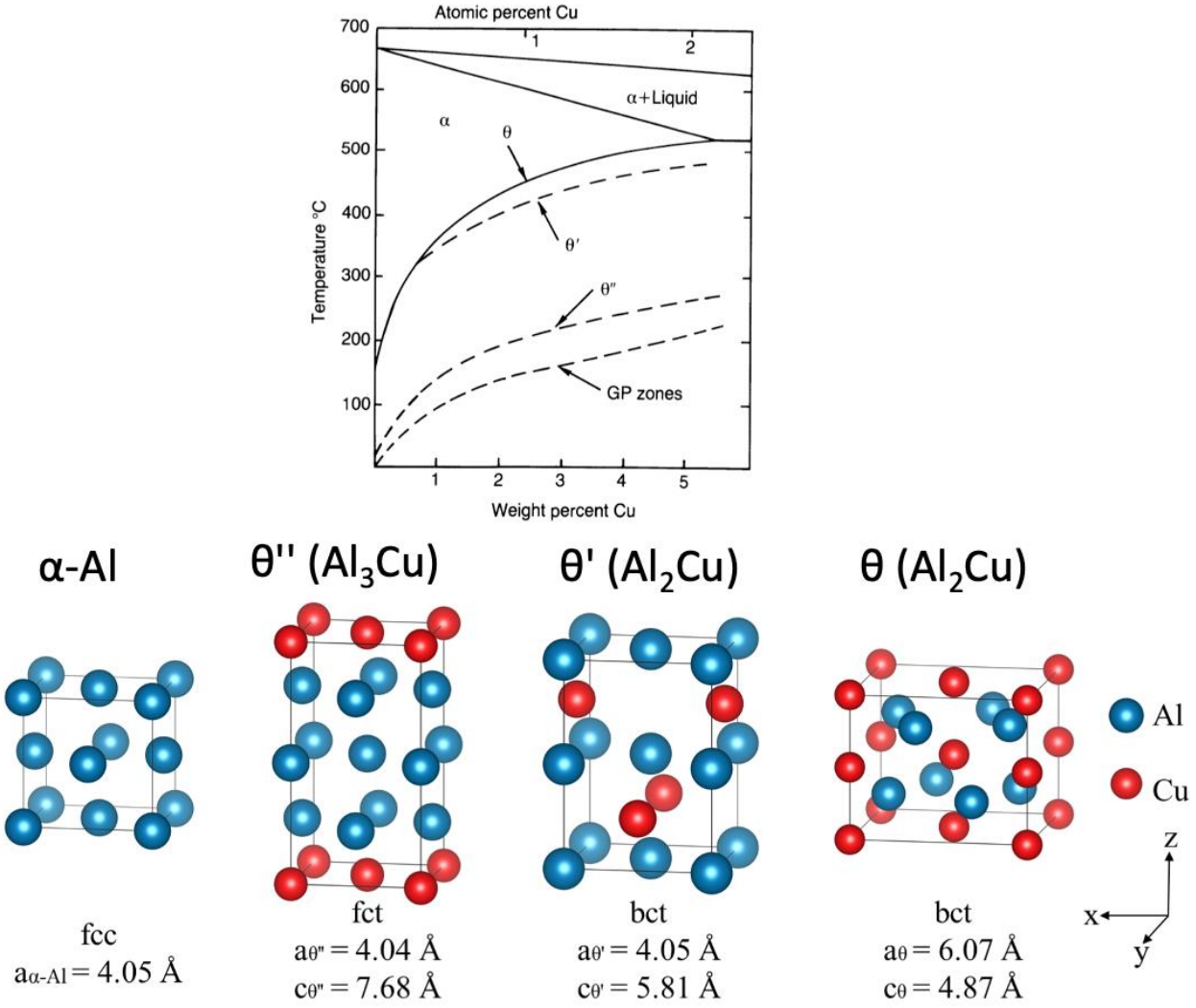

Figure 2: metastable solvi of the Al-rich end of the Al-Cu phase diagram [21] and schematic depictions of the unit cells of the fcc Al and the Alx-Cu related precipitate phases [27].

Age hardening (precipitation hardening) plays a vital role in Al-Cu alloy strengthening mechanisms. Thus, the precipitation sequence and the associated transitions phases, GP zones, θ'' and θ', have been studied significantly where they show various effects on the mechanical properties [29]–[32]. Figure 3 shows an example of how the hardness is affected during isothermal aging at 130˚C for different compositions in the range of 2.0 wt.% Cu to 4.5 wt.% Cu due to formation of the transition phases (GP zones, θ'' and θ') in Al-Cu binary system. The main

strengthening mechanism after quenching is solid solution strengthening which has a relatively low impact on the increments in micro-hardness measurements. During aging, GP zones start forming first and are responsible for a linear increase in hardness in the semi-log plot against aging time (Figure 3). Notably for the highest Cu solute content alloys a plateau in the age-hardening curve can be detected, which implies that the fraction of GP zones formed has reached a maximum. The increased hardness can be attributed to retardation of the external stress or loading induced dislocation movements, which is required to cut through the misfitting coherent GP1 zones. At longer aging time, θ''-phase then subsequently θ'-phase precipitates form, leading to further hardness increases. A maximum in the hardness measurements is observed typically when a combination of θ''- and θ'-phase precipitates are present. Further aging for times longer than those for the observed maximum or peak hardness increases the size of the θ' precipitates and dissolves the θ'' phase. This coarsening of θ'-phase precipitates increases the spacing between precipitates, which act as obstacles and pining points for dislocation glide motion. As the inter-precipitate spacing increases this eventually allows the dislocations to bow between them for decreasing amounts of resolved shear stress. As a result, the hardness decreases [33]. As aging times are prolonged well beyond the peak-aged state θ'-phase precipitates dissolve and are being replaced by the equilibrium phase, θ-phase, resulting in further coarsening of the precipitate size and thus reduced hardness. This final stage in the precipitation sequence and its effect on hardness are not captured in the data displayed in Figure 3.

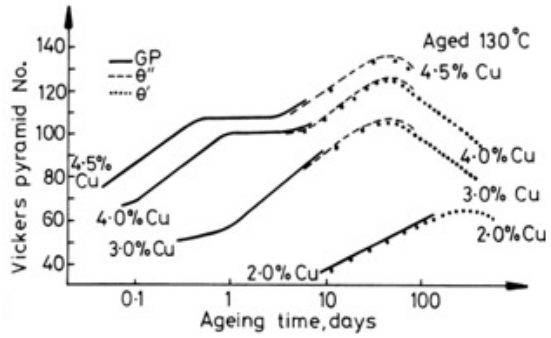

Figure 3: Hardness vs time for different Al-Cu alloys aged at 130°C (After J.M. Silcock. T.J. Heal and H.K. Hardy, Journal of the Institute of Metals 82 (1953-1954) 239)

2.2 Solidification at Non-Equilibrium Conditions

In the context of the proposed research solidification relates the phase transformation from the liquid to a crystalline solid state of metallic multi-component alloys. Here we are not concerned with formation of amorphous solid from the liquid melt. Examples of important processing methods where solidification is the dominant transformation phenomenon include casting, welding, soldering, melt-spinning, surface remelting etc. [34]. Solidification phenomena are very important in materials science and engineering. For metals and metallic alloys solidification represents the first opportunity to manipulate the material microstructure and typically is the first major processing step in fabrication of materials stock for manufacturing of components and devices across a wide range of technological sectors of industry. Solidification theories have been developed to predict and rationalize the development of different alloy microstructures observed for changes in the solidification conditions [35]. Notably, conditions for solidification, such as cooling rates, crystal growth or solidifications rates and temperature gradients, vary across

multiple orders of magnitude when comparing sand casting (cooling rates about 10^1-10^2 K/s.) and electron beam welding (cooling rates about 10^7-10^{11} K/s) for instance [36]. As a result, for a given alloy the weld microstructure and properties differ dramatically from that of a casting. Since mechanical properties of metals and metallic alloys are strongly depended on the microstructure scale and morphology, an understanding of solidification microstructure evolution is highly desirable. For example, in casting products defects in the cast microstructure often persist during subsequent solid state processing and influence mechanical properties and deformation behavior [35][37]. Increasing the solidification rate, like in laser surface remelting, results in changing the microstructure morphology, e.g., a decrease of the lamella spacing in regular lamellar eutectic structures. The microstructural scale refinement and morphological changes alter the mechanical properties of the final products [6]. Thus, controlling the solidification process is vital to ensure that the required materials properties can be achieved. The key features in microstructure evolution during solidification processes are mainly driven by the rate of transferring heat from the melt to the solid and interfacial undercooling [34].

All solidification processes require heat extraction by removing heat from the melt. During heat extraction the enthalpy (ΔH) of solid and liquid phases changes. The enthalpy decreases due to cooling and due to transformation from the liquid to the solid state [34]. Since the formation of solid from the liquid during solidification is associated with the evolution of the latent heat of crystallization or freezing it is an exothermic process. The latent heat evolves at the interface between solid and liquid and must be transported away into the adjacent phases. If the heat extraction balance is such that the excess of latent heat is extracted on balance into the solid, migration of the interface between soldi and liquid is biased towards the liquid, i.e., implying growth of the solid by solidification. Typically, solidification, i.e., the transformation of the liquid

phase to the solid phase of an alloy, is a process described by distinct stages of nucleation and subsequent growth of the solid [21]. The physical atomic structure of the two phases (solid crystalline and atomically disordered liquid) is different, where the solid crystalline state has long range order and liquid states have only short-range order (amorphous). This atomic structure difference creates a distinct interface between crystalline solid and melt. In some solidification processes, e.g., fusion welding, this interface pre-exists since melt remains in direct contact with the bulk substrate material, while in other processes it must be formed via the nucleation stage. The excess free energy of the solid-liquid interface creates an energy barrier (ΔG^*) that must be overcome for nucleation. As the undercooling (ΔT) increases, the ΔG^* decreases. Once ΔG^* is lowered sufficiently, at certain time, a solid nucleus at critical nucleus size (r^*) is going to form, Figure 4.

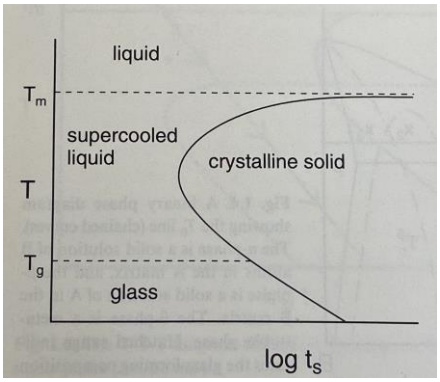

Figure 4: T-T-T diagram for liquid to crystal transformation [1]

For alloy solidification we have a multi-component system. The solute (second component) addition renders the transformation more interesting. Composition related changes in the chemical potentials, i.e., solutal or constitutional effects, must be considered and can become important in addition to the thermal effects dominating solidification behavior in single component systems. This leads to the concept of constitutional undercooling. Figure 5 represents a left side of

hypothetical binary phase diagram. C_0 is the alloy composition and after melting represents the starting liquid composition that is going to solidify into a single-phase solid solution. Here, T_L is the liquidus temperature, T* is the solid-liquid interface temperature at some point in time (temperature) during solidification, and T_S is the solidus temperature. At the T*, at solid-liquid interface, the solid composition is C^*_S and the liquid composition is C^*_L. The relation between the compositions of the two phases at the interface is called the equilibrium partition coefficient (k),

$$\boldsymbol{k = \frac{C_S^*}{C_L^*}} \qquad \textbf{(2-1)}$$

The difference in equilibrium solubility of the alloying element in solid and liquid is causing additional undercooling called constitutional undercooling (ΔT_c). This solute concentration difference (ΔC_0) at T_S in Figure 5 is the reason for development of solute segregation in alloys [38].

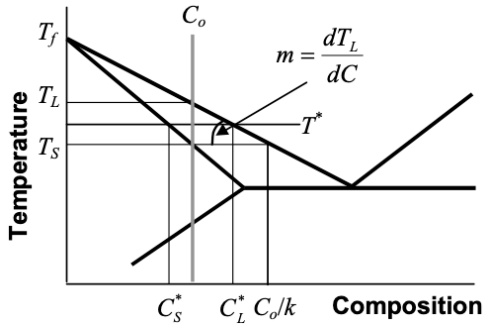

Figure 5: Schematic region of a phase diagram for a solid solution alloy [38]**.**

A diffusion boundary layer (δ_C) forms at solid-liquid interfaces at solidus temperature (T_s) because the liquid composition at interface (C_0/k) is higher than bulk liquid composition ($C_L=C_0$), as seen in composition - distance (x) diagram in Figure 6 (a). As a result of this the constitution

(composition) of the liquid adjacent to the solid-liquid interface changes as a function of distance into the liquid. A compositional thermal gradient (solutal thermal gradient, G_L) develops over the distance δ_C; i.e. the solute content decreases from C_0/k in the liquid at the interface to C_0 at a distance δ_C into the liquid, while the liquidus temperature in the diffusion boundary layer of width δ_C increases from T_S at the solid-liquid interface to the bulk liquid temperature T_L, Figure 6 (b). In addition to the compositional gradient, there is thermal gradient (actual thermal gradient, G_T) in the liquid as the heat flows out from the liquid to the solid. The comparison between G_T and G_L gives two situations: i) G_T is bigger than G_L, implying that temperature of the liquid ahead of the interface is higher than the liquidus temperature of the alloy, and ii) G_L is bigger than G_T. In case ii) the liquid at the interface is undercooled below the liquidus temperature of the alloy liquid for some distance, due to the increased solute concentration reaching at maximum, C_0/k, while the bulk liquid temperature is above the liquidus temperature at larger distances, Figure 6 (c). This region in the liquid adjacent to the solid-liquid interface is constitutionally undercooled and is often simply called the constitutional undercooling [38]. If the growing solid can access regions of constitutional undercooling in the alloy liquid that develop adjacent to the solid-liquid interface morphologically planar interfaces become unstable and transition to cellular and dendritic growth morphologies evolve the solidification microstructure (see section 2.3).

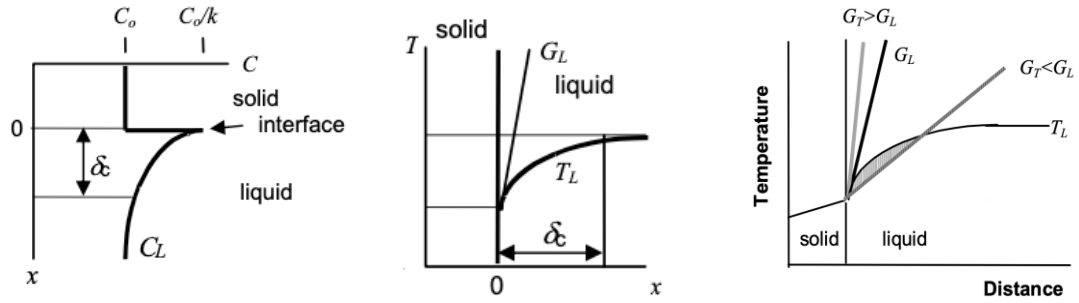

Figure 6: The (a) solutal and (b) thermal fields in front of the solid/liquid interface, (c) constitutional undercooling diagram comparing thermal (G_T) and liquidus (compositional) (G_L) gradients [38]**.**

2.3 Microstructural Development in Rapid Solidification

A solid–liquid interface velocity (V_{SL}) develops different patterns, depending on the solute concentration and undercooling conditions it encounters. For example, in a binary alloy when a solute solidified with applying small amount of constitutional supercooling, the planar interface can be destabilized favoring the onset and the development of cellular patterns at the interface [39], [40]. In general, the solidified microstructure can be categorized into two main groups: cells/dendrites (single phase growth) and eutectic morphologies. Al-Cu alloy is one of the model systems that showed interesting rapidly solidified microstructure morphologies. The lamellar spacing of eutectic constituent refined to tens of nanometer [41], [42], wavy lamellar structure [41], banded structure [41], solubility extension [41], [42] and microsegregation in dendritic to cellular structure [42].

During equilibrium solidification of Al-Cu binary system, the excess of solid solubility of Cu (2.48 at.%Cu) forms a eutectic constituted by an Al-rich primary phase and intermetallic Al_2Cu

(θ) phase. However, for rapidly non-equilibrium solidification of the alloy, which is driven by large undercooling developing in response to rapid heat extraction, results in formation of metastable GP zones, θ''- and θ'- phases. The rapid solidification affects, beside the extension of solute concentrations beyond the equilibrium solubility limits, the cellular/dendritic growth as well as of eutectic constituent and distribution of intermetallic particles.

Many studies have discussed the evolution of microstructure during rapid solidification [2], [3], [6], [9], [10], [14], [16], [43]. The microstructure and microstructural transitions of Al-Cu alloy has been explored in some detail and a solidification microstructure selection map (SMSM) has been developed [2], [16]. At the eutectic composition (Al-32.7 wt% Cu) three microstructure morphologies had been observed based on solid/liquid interface growth velocity (V_{SL}). If $V_{SL} \leq 0.2$ m/s, regular lamellar eutectic growth that follows the relationship $\lambda^2 V_{SL} = \text{const.}$ [44] where λ^2 is the interlamellar spacing has been reported, Figure 7 (a). When, $0.2 < V_{SL} < 0.5$ m/s, the metastable θ'-starts to replace the thermodynamically stable θ-phase, and the regular lamellar morphology of the eutectic is modified, becoming wavy and λ increased, Figure 7 (b). Banded region morphologies have been observed at velocities higher than 0.5 m/s. At hypoeutectic alloy of Cu wt.% between 25 – 28 wt%, the microstructure observed was reported as oscillatory structures of the lamellar eutectic. Above 0.1 m/s, cellular growth started and was followed by banded structure at solidification interface velocity higher than 1 m/s. At composition lower than 25 wt% Cu, dendritic/cellular structure was observed which was replaced by banded at ~1 m/s [16].

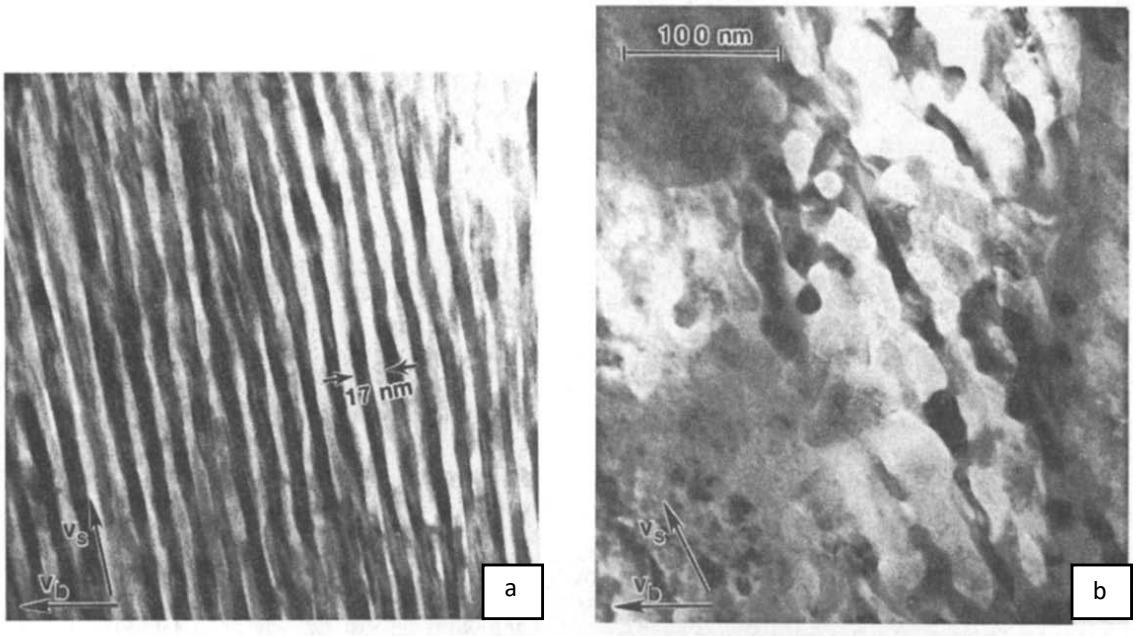

Figure 7: The structure appears in Al-32.7 wt% Cu. (a) Fine eutectic spacing at V=0.2 m/s. (b) Wavy eutectic structure at 0.2 m/s < V < 0.5 m/s. [16]

In recent studies, direct observation of microstructure formation during rapid solidification after laser melting has been achieved for hypoeutectic Al-Cu alloy thin films by using experiments performed with the dynamic transmission electron microscope (DTEM) [3]–[5], [9], [14]. The microstructure of rapidly solidification Al-11 at% Cu thin film showed four distinct zones, Figure 8. As the solid-liquid interface velocity, V_{SL} accelerates, the microstructure morphology changes. Coupled growth regime of α-Al and θ-Al_2Cu were observed at V_{SL} < 0.3 m/s and α-Al and θ'-Al_2Cu at 0.5 m/s < V_{SL} < 0.8 m/s [3]. On another study [45], the rapid solidification microstructure of hypoeutectic Al-26wt% Cu alloy produced by imposing a 29 Tesla super high static magnetic field (SHSMF) showed refinement of primary α-Al (Cu) and interlamellar spacing of eutectic structure. Also, the content of Cu increased from 8wt.% to 10wt.% after rapidly solidified [45]. This higher Cu explained by the high dislocation density which facilitate solute trapping. The

immense scale refinements and the characteristic morphologically distinct regions observed as a result of these microstructure changes during rapid solidification should have direct effects on the mechanical behavior of the solidified alloy.

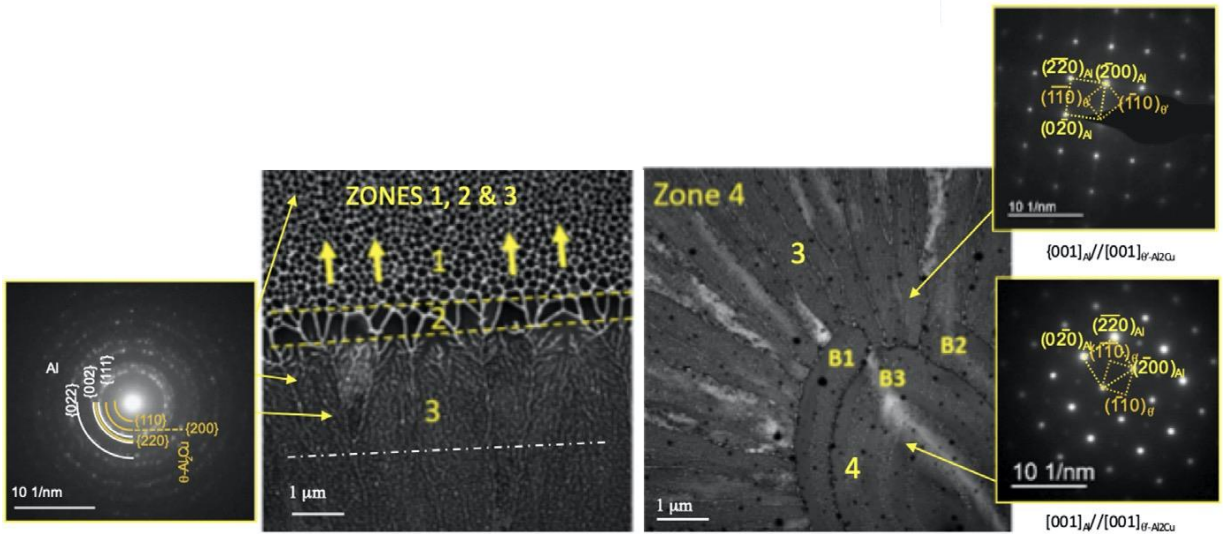

Figure 8: Morphology of the solidification microstructure in the distinct zones of the heat affected zone (label 1), the transition region/zone (label 2), the columnar growth zone (label 3), and the banded morphology zone (label 4), inclusive of representative example selected area diffraction pattern. [3]

2.4 Nanoindentation

Nanoindentation is widely utilized as a powerful method to examine nano- and micro-scale surface mechanical properties in very small volumes. Nanoindentation is a depth sensing technique at continues load monitoring. Unlike the conventional hardness tester, nanoindentation does not require a microscope to measure the impression of indents to compute the hardness, as the tip contact area is measured with the depth of the indent and the indenter geometry.

Several studies used nanoindentation techniques to measure the hardness H. Bhoi and his group [46] used nanoindentation to explore the mechanical properties of aluminum yttrium oxide (Al–Y_2O_3) composite material. They added Y_2O_3 nanoparticles to Al as reinforcement at various wt%. They obtained the nano-hardness changes at different Y_2O_3 wt% by applying 2000 μN maximum force. Increasing the Y_2O_3 amount resulted a significant rise in hardness by 134.6%. Another group of researchers [47] investigated the mechanical properties of intermetallic phases in Al-Si alloys. Here nanoindentation was performed with maximum load of 20mN on large, micro-scale intermetallics phases. The results showed H differences for different phased based on the phase composition and strucrture. For example, the H values of Al_7Cu_4Ni phase varies as Ni content changes. Hidetoshi Somekawa and Christopher A. Schuh [48] have conducted nanoindentation study on five types of Mg–0.3 at.% X (X = Al, Ca, Li, Y or Zn) binary alloys to assess the solid solution strengthening in these alloys. They have applied 1000 μN maximum load at different loading rates. The hardness values determined by nanoindentation differed from hardness values obtained by mechanical testing on a larger length scale, which was attributed to differences in the size of the respective activation volumes producing different deformation mechanisms. Also, the solid solution strengthening tested via nanoindentation resembled the plasticity shown in single crystal of other alloys tested by conventional hardness tests [48].

3.0 Materials and Experimental Procedures

3.1 Alloy Preparation

Hypoeutectic alloy with a target composition of Al-10 at% Cu (Al-10Cu) was prepared using vacuum arc-melting with an Arc Melt Furnace ABJ-338 (Materials Research Furnaces, LLC). High purity elemental Al (99.99% pure) and Cu (99.9999% pure) metal were used. The weight ratio of aluminum shot and copper wire was 22.5g/6.55g. The materials were placed inside the furnace crucible and melted under argon environment after three cycles of evacuation and purging with argon gas. The Al-10Cu button was remelted multiple times (6 times) to ensure compositional homogeneity of the sample, then it was solidified in a water-cooled copper mold. The resulting alloy button had dimensions of approximately 15 mm thick and about 35 mm in diameter as measured from the mechanically ground top surface. The chemical composition of the as-cast button was measured using energy-dispersive x-ray spectroscopy (EDS), Ametek EDAX, with a scanning electron microscope (SEM), Thermo Fisher Scientific/FEI Apreo high-vac. The composition measurements have been performed using spot and scanned area modes of SEM EDS for systematically varied electron accelerating voltages of 5kV, 10kV and 20kV, respectively. This permitted assessment of possible effects of the analytical volumes probed in spot mode on the standardless quantification of the EDS measurements.

3.2 Laser Surface Remelting

To prepare the alloy buttons for laser surface remelting, the specimen surfaces have been prepared by mechanically grinding with SiC abrasive paper up to grade 1000 grit. The sample surfaces have been abraded to introduce deliberately some roughness to enhance the laser energy absorption. Notably, Al metal and alloy exhibit large reflectivity for laser wavelengths in the near infrared to the near-UV range [49]. The surface remelting has been performed on the metallographically prepared alloy samples using two different scanned laser systems: i) the LENS 450 3D direct laser deposition system (Optomec, Inc) and ii) the EOS M290 laser powder-bed fusion system (EOS GmbH). Both systems were equipped with 400W Yb-fiber lasers operating in continuous wave mode at a wavelength of 1060-1100 nm in the near-infrared. Single pass laser traces were created using the LENS 450 system at 370W laser power and 270μm diameter spot size at 3mm/s laser scan velocity. Using the EOS system offers access to higher laser scan velocity at smaller spot size of ≈ 100μm diameter. Using the EOS 290M three single pass laser traces were created at scan velocities of 1 m/s, 2 m/s and 4 m/s, respectively. Additional sets of laser traces using the EOS system have been performed for systematically different remelting conditions. A total of nine (9) additional scanned laser traces were applied to the vacuum arc-melted button of the Al-10Cu alloy for systematically varied conditions (see summary in Table 1). The three traces labeled as Trace#1, #2 and #3 (Table 1) were obtained for a single scan velocity of 2 m/s at a constant power of 370W for two, four and six laser scanning passes, respectively. Application of multiple, two to six, laser scan passes to a given trace results in multiple melting-solidification cycles. This approach enabled exposing the alloy to systematically varied total durations in the liquid state prior to the final solidification. Each of the multiple laser melting events provides

opportunity for convection, turbulence and diffusion assisted mixing to create a compositionally homogeneous liquid prior to solidification by epitaxial growth of crystals from the surrounding solid substrate of the Al-10Cu alloy. The effects of the number of subsequent passes by the scanned laser on the resulting melt-pool dimensions, and the morphology and scale of the solidification microstructure can be evaluated. The scanned laser melting traces labeled as traces#4 to #9 have been obtained by applying an initial set of either three (3) or six (6) laser scan passes at a scan velocity of 1m/s at 370W to create a melt-pool with relatively large dimensions. Subsequently, a single (1), two (2) or three (3) additional scan passes have been performed at higher scan velocities of 2 m/s and 4 m/s, respectively, to create smaller dimension melt-pools within the solidification microstructures obtained from the larger melt-pools obtained at scan velocity of 1 m/s. Table 1 summarize the conditions associated for the nine traces. In all scanned laser beam melting experiments the laser beam incidence was normal to the sample surface, which has been shielded by a continuous Ar gas flow to prevent excessive oxidation during remelting.

Table 1: EOS nine laser traces conditions

Single laser trace				
Trace #	laser scan speed	# of passes		
1	2 m/s	2		
2		4		
3		6		
Two laser traces on top each other				
	larger melt pool		smaller melt pool	
Trace #	laser scan speed	# of passes	laser scan speed (m/s)	# of passes
4	1 m/s	3	2 m/s	1
5		6	4 m/s	
6		3	2 m/s	2
7		6	4 m/s	
8		3	2 m/s	3
9		6	4 m/s	

3.2.1 Laser Trace Cross Sectioning Procedure

To study the rapid solidification (RS) microstructure, the buttons containing the laser traces have been sectioned to reveal the dimensions and shape of the melt pools, as well as to enable study of the solidification microstructure. A schematic representation of the scanned laser surface remelting process with respect to the alloy substrate and the melt race is shown in Figure 9d. The coordinate system shown in Figure 9d by green arrows defines the laser scan direction as the x-direction, the laser beam direction of incidence as the z-direction and the cross-section from right-to-left as the y-direction. Two types of cross sections were obtained: i) a short transverse or simply a transverse cross section, which is the (y-z)-plane in the graphic of Figure 9d, i.e., perpendicular to the laser beam scan direction (x-axis in Figure 9d), and ii) a long transverse or simply longitudinal cross section, which is the (x-z)-plane in Figure 9d, i.e., parallel to the laser beam scan direction (x-axis in Figure 9d). In the transvers section, the (y-z)-plane in Figure 9d, the button was cut using a precision low speed saw (TechCut 4™, Allied HighTech Products, Inc) using a blade (diamond metal bond) of thickness (0.15 mm). The resulting sections of the buttons, typically with dimensions of 22 mm long, 7 mm high and 5 mm thick, were then prepared by following the standard metallography preparation methods for Al alloys. These included, first, mechanical grinding using SiC abrasive grinding foil #1000 and subsequently mechanical polishing by using diamond paste of decreasing sizes of 6 μm, 3 μm and 1 μm. A colloidal silica (0.04 μm) suspension was used for the final polishing step. To remove any residual silica the sample surface was washed under DI water, then wiped with cotton and soap, washed again in DI water, rinsed with alcoholic solvent, and then dried with warm air using a hair dryer. Then the sample was polished with only

DI water, rinsed with alcoholic solvent, and dried. All metallographic preparations were done by using an automated polishing/ grinding wheel and manually applying a down force.

A different sectioning procedure of the button is necessary to enable analysis of the solidification microstructures in a longitudinal cross-sectional view, the (x-z)-plane in Fig. 9d. Samples obtained from the button should ideally include a trace with sufficient length to facilitate microstructural analyses. Therefore, a PELCO® Precision Wire Saw™ (Ted Pella, Inc.) has been utilized for sectioning. A stainless-steel wire blade, cross-sectional diameter 0.015"≈ 380µm, with abrasive slurry has been used to excise a suitable sample from the button Figure 9a. The recipe for the abrasive slurry was 1 part of BC abrasive powder, 4 parts glycerin and 1 part H_2O (all parts are by weight). To reveal each laser trace for microstructural analysis, additional metallographic preparation by precision grinding and polishing is necessary to remove the unaltered as-cast matrix material volumes between adjacent traces, and to remove just enough of the solidification microstructure of the laser trace of interest to observe the central section of the trace. The central region of the solidification microstructure resulting from the scanned laser surface remelting is marked by black dashed lines in the graphic of Figure 9d. The preparation of sections oriented parallel to the laser trace scanning direction, (x-z)-plane sections in Figure 9d and revealing the center of the laser traces requires high precision sample alignment and fine scale control of the material removal rate. To control the geometry during metallographic grinding and polishing relative to the orientation of the laser traces the sectioned sample from the alloy button was mounted to a reference-edge cross-section paddle in an orientation where the (x-z)-planes of the laser traces are parallel with the surface of the grinding/polishing wheel, i.e., the laser scan direction is parallel to the grinding/polishing wheel surface, Figure 9c. The paddle was attached to a precision sample preparation system, the MultiPrep™ System (Allied High Tech Products, Inc).

The grinding/polishing process was executed by following the standard metallography preparation methods discussed before. During the grinding/polishing process, the sample was inspected frequently under the optical microscopy (OM) until the laser trace center line was reached. To ensure the center line of the laser trace has been approached, the sample was checked by inspections using two orthogonal directions of views. The width of the trace when viewed from the top (parallel to the laser incidence on the alloy sample surface, the (x-y)-plane in Figure 9d, and depth of the trace in transverse cross section when viewed from the side, the (x-z)-plane in Figure 9d, have been measured. The location of the center line of the melt pool prior to solidification after scanned laser trace melting should be at the middle of the total width from the top view, i.e, when viewed parallel to the z-axis defined in Figure 9d and at the maximum depth measured from the side view (transverse cross section depth), i.e., when viewed along a direction parallel or antiparallel to the y-axis defined in Figure 9d.

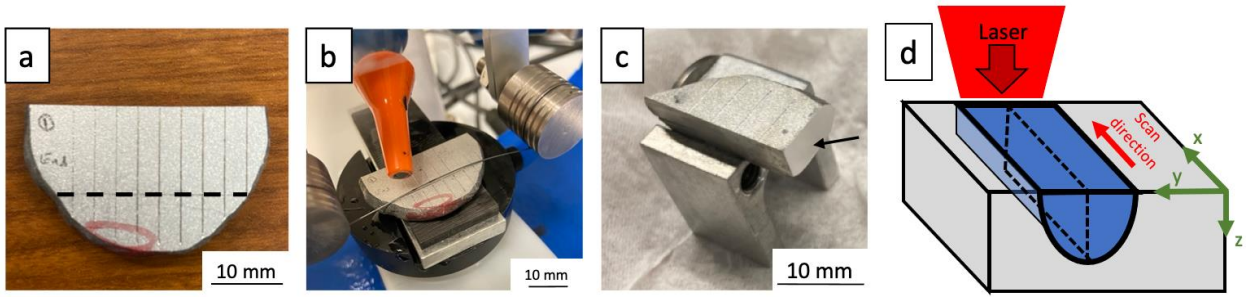

Figure 9 Picture of the sample used for longitudinal section. a) the dashed line indicates the sectioning line. b) the button set up in PELCO® Precision Wire Saw. c) the sample after sectioning and the arrow indicates the polishing side for revealing the longitudinal cross section, d) schematic representation of the scanned laser surface remelting process with respect to the alloy substrate and the melt race.

3.3 Nanoindentation Method

Nanoindentation is a depth-sensing, instrumented indentation technique, where continuous monitoring of depth of penetration and the applied load are recoded [50]. The depth-sensitive data recording permits generating the load – displacement (h) diagram based on the loading-unloading data recorded. From the load - penetration depth (displacement) diagram, three characteristic depths are acquired: 1) maximum indentation depth (h_{max}) results at the peak load (P_{max}) where plastic and elastic deformation exist, 2) final indentation depth (h_f) is the depth of residual impression when the load has been removed and only plastic deformation is present, and 3) contact depth (h_c) is the actual depth at which there is a contact with the indenter tip during the indent; i.e. h_c is not necessarily equal h_{max}. The contact depth considers any sink-in (h_s) that happens at the perimeter of the indent during material deformation, Figure 10a. The Oliver and Pharr method [51] is adopted to find the values of h_c. Here the stiffness (S) needs to be calculated first by measuring the slop at P_{max} of the unloading curve; $S = dP/dh$. Then, according to the Oliver-Pharr method,

$$h_c = h_{max} - \varepsilon P_{max}/S \quad \textbf{(3-1)}$$

Where, ε is a geometric constant, which is ε = 0.75 for a Berkovich indenter. A schematic of a typical compliance curve for nanoindentation is shown in Figure 10.

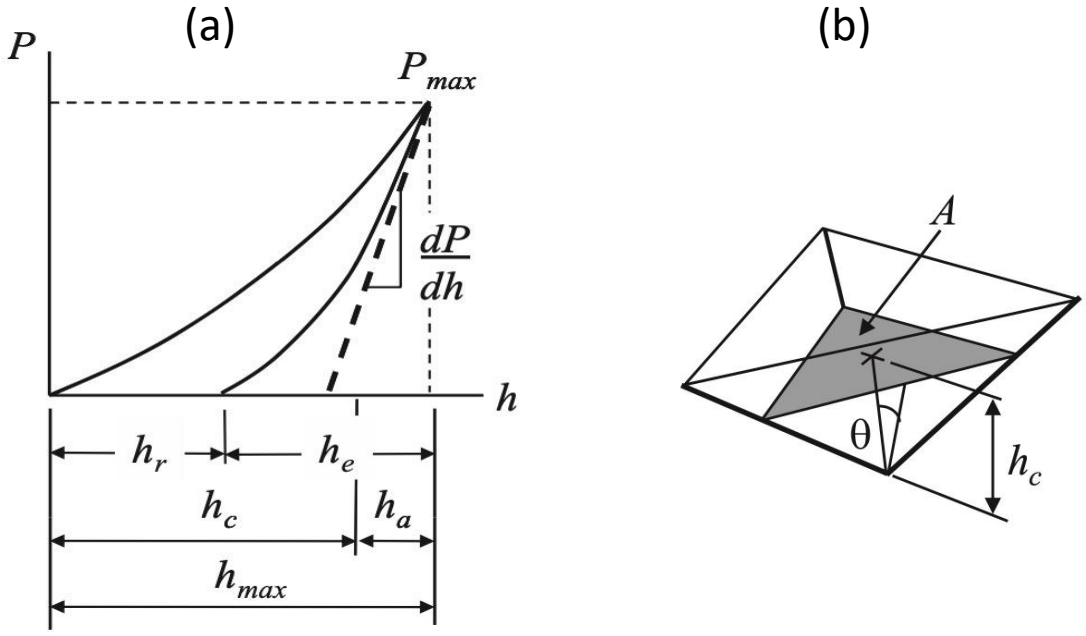

Figure 10 (a) loading and unloading curve of typical nanoindentation. (b) Berkovich indenters indentation parameters, θ =65.27° [52]

The Berkovich indenter is a three-sided pyramid indenter which has the advantage relative to other indenter types, such as the four-sided Vickers pyramid, that the pyramid edges can be constructed relatively easily to meet at a single point. The most common face angle used for Berkovich indenters is θ=65.27° (Figure 10b), which gives a similar ratio of projected area to depth as the Vickers indenter [52]. To find the hardness (H) of nanoindentation measurements using a Berkovich indenter the projected area of contact (A) needs to be calculated by:

$$A = 3\sqrt{3}h_c^2 tan^2\theta$$

$$A \approx 24.5h_c^2$$

(3-2)

Thus, the hardness, H, from the peak load (P_{max}) and projected area of contact (A) is:

$$H = \frac{P_{max}}{A}$$

(3-3)

The specimen surface was prepared for nanoindentation experiments following the standard metallurgy procedure for Al alloys (also see section 3.2.1). Instrumented nanoindentation hardness measurements have been performed with the nano-mechanical test system (Hysitron TI900 Triboindenter) using a diamond Berkovich indenter tip in load control mode. The three segments of the quasi-static trapezoidal loading function comprised of loading to maximum load (P_{max}) followed by holding time then unloading to zero at room temperature. The loading – unloading was carried out at constant rate of P_{max}/10 sec. The thermal drift threshold for all indents was set at 0.05 nm/s. Arrays of indentations have been acquired for various spatial matrices on the as cast microstructure and characteristic regions of the RS microstructures established from the scanned laser surface remelting induced melt pools. Individual indentations were separated by at least 3 μm to avoid artifacts from prior neighboring indents on the hardness measurements. For each hardness measurement reported here for a given phase, microstructural constituent or characteristic morphology established in the RS microstructures of the alloy at least 5 independent indentations have been performed to ensure reproducibility and measurement accuracy. The nanoindentation data processing was performed using the Oliver-Pharr methodology [51]. The TriboScan^{TM} 9 software (Hysitron, Inc.) was used for data acquisition and post-acquisition processing.

3.4 Scanning Electron Microscopy

The scanning electron microscopy (SEM) investigations and analyses have been performed using a Schottky Field Emission Scanning Electron Microscope (FESEM), Apreo High-Vac (Thermo Fisher Scientific), equipped with Octane Elite SDDs Energy Dispersive X-ray Spectroscopy (EDS) and EDAX Hikari Electron Backscatter Diffraction (EBSD) from EDAX, AMETEK, Inc. The elemental composition and crystal structure post-acquisition data analysis for EDS and EBSD was conducted with the TEAM™ software (Edax, Ametek Inc.). The Scios™ 2 DualBeam™ FIB SEM system (Thermo Fisher Scientific) (DB-FIB) was used for site-specific TEM lamella samples preparation.

The microstructural morphology and scale have been studied by SEM imaging using the back-scatter-electron acquisition modes, while the chemical composition analysis has been performed by EDS for the cast specimen and surface laser remelted transverse and longitudinal cross sections to measure the chemical composition of each phase. The EBSD technique was used to provide statistically significant and representative data sets of the phase and crystal orientation distributions of the single phase grains of the RS microstructures developed across the laser scanning induced melt-pools. Thin lamella samples obtained by DB-FIB preparation have been plasma-cleaned using a low-energy argon-oxygen plasma with the Fischione Model 1070 NanoClean system to remove any organic contamination prior to investigation by transmission electron microscopy (TEM) and scanning TEM (STEM).

3.5 Transmission Electron Microscopy

The FEI Tecnai G2 F20 TEM was operated a 200 kV accelerating voltage to obtain representative data by bright field (BF) and dark field (DF) imaging, selected area electron diffraction (SAED) and spot-spectra EDS elemental analysis. The TEM studies have been performed to supplement larger scale analyses performed with the SEM with data sets that offer nano-meter scale spatial resolution for quantitative measurements for composition analysis and grain size. Additionally, imaging and diffraction studies enabled of nano-scale phases regarding actual size, morphology, crystal structure and composition.

3.6 Heat Treatment

Annealing heat treatments have been performed to assess the thermal stability and transformation pathways of the metastable alloy microstructures established by the non-equilibrium processes of RS in the laser trace irradiated melt pool of the Al10Cu alloy. Specimens for isothermal annealing studies were sectioned from the Al-10Cu button as thin slices using the wire saw. The slices had initial dimensions of ≈ 5 mm length, 2 mm width and 500 μm depth. The relatively small size of these specimens and the good thermal conductivity of the Al-alloy facilitates rapid heating and cooling cycles while establishing a homogenous temperature profile across the sample. Each thin slice specimen was cleaned using ultrasonic cleaner prior to the annealing heat treatment. The annealing has been performed using a rapid thermal annealing system (ULVAC-RIKO, MILA-3000) in a high vacuum at isotherms of 180˚C, 230˚C and 280ºC

for times between 2 minutes and 8 minutes. The heating rate was 10ºC/s from room temperature (RT) to the desired annealing temperature, then furnace cooled to RT.

4.0 Results and Discussion

4.1 As Cast Hypo-Eutectic Al-10at%Cu Alloy

The as cast Al-10Cu microstructure was comprised of primary α-Al(Cu) dendrites surrounded by regular lamellar eutectic of two phases (α-Al+θ-Al_2Cu). These are the microconstituents expected for a hypoeutectic alloy. The microstructure is depicted in Figure 11, where the dark region is α-Al(Cu) and the bright region is θ-Al_2Cu. The α-Al dendrites have secondary arm spacings on the order of approximately 20 μm and the regular lamellar α-θ eutectic has average lamellar spacing of $\lambda \approx 0.75 \pm 0.2$ μm. The volume fraction of α-Al has been determined as ≈ 45% from image analysis of SEM micrographs, using the area fraction as a stand-in metric. Thus, the as-cast Al-10Cu alloy microstructure was consistent with predictions based on the Al-Cu equilibrium phase diagram [18]. The SEM-EDS measurements showed an average alloy composition of Al-10 at% Cu for the as cast structure with 2.30±0.05 at.% Cu solute in the α-Al dendrites. Within the certainty limit of the EDS measurements the Cu solute concentration in the primary α-Al dendrites closely approaches the maximum equilibrium solubility of Cu, 2.5 at% Cu, observed for the eutectic isotherm, which indicates that the specimen was cooled relatively fast.

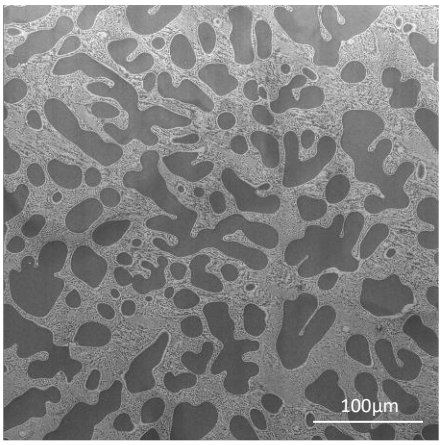

Figure 11 As-cast hypereutectic Al-10Cu alloy. The dark regions represents α-Al phase in the primary dendrites and in the eutectic, and the bright regions represent the θ-Al_2Cu phase in the eutectic microconstituent.

4.2 Rapid Solidification at Low Scan Velocity via Single Track Melt Trace

The Al-10Cu alloy has been exposed to single-trace laser scanning surface remelting using the direct-metal-deposition platform LENS 450 System. Figure 12 shows cross sections (transverse and longitudinal) of the laser traces made by near-infrared laser irradiation using a power of 400 W, scanning speed of 3 mm/s = 0.3cm/s = 0.003m/s, and beam spot size of nominally ~250 μm. The laser scanning direction points into the plane of the transverse cross section of the solidification microstructure shown in Figure 12a. The melt pool exhibited a semielliptical shape with transverse cross-sectional dimensions of 100 μm in depth and 300 μm in width, (Figure 12a). With reference to the schematic of Figure 9d, the micrograph of Figure 12a represents the (y-z)-plane section as viewed along the x-direction.

Directional solidification proceeded via seeded epitaxial growth from the bulk substrate microstructure of the as-cast Al-10Cu alloy that can be seen at the perimeter of the region for which a melt pool was established by the scanned laser irradiation in Figure 12a,b. The solidification interface migrated on average in a direction perpendicular to the isotherms, which are marked qualitatively as dashed lines in the longitudinal cross-section micrograph of Figure 12b. With reference to the schematic of Figure 9d, the micrograph of Figure 12b represents the (x-z)-plane section as viewed along the y-direction.

The solidification interface migration rate, its velocity, V_{SL}, increased from zero at the perimeter of the melt pool to a maximum in the center at the top of the melt pool, where the last liquid solidified. Considering a vertical line bisecting the semi-elliptical transverse cross section of the former melt pool shown as the RS microstructure in Figure 12a the solidification interface migrated with an increasing rate from the bottom to the top. The rapid heat extraction from the melt into the adjacent solid bulk alloy substrate resulted in significant scale refinement of the primary α-Al phase, which adopted the shape of dendritic cells, and of the eutectic constituent in the solidification microstructure of the alloy.

The section marking the centrally located rectangle in Figure 12a is depicted at enhanced magnification in Figure 12c, where morphological differences can be discerned for three characteristic regions. The three distinct microstructure regions identified in the transverse cross-section (Figure 12c) can, also, be discerned in the longitudinal cross section of the melt pool (Figure 12b). The microstructure changes from the bottom to the top of the melt pool as the solidification rate changes. The bottom part of the melt pool, where the solidification started by directional growth from the as-cast microstructure of the un-melted bulk alloy substrate and solidification interface velocity is relatively slow, primary a-Al and lamellar eutectic present. The

middle part of the melt pool has a structure comprised of equiaxed α-Al (Cu) grains forming a cellular structure with intercellular regions containing θ phase or eutectic (α + θ) with a refined scale relative to the as-cast state. The solidification completed in the center at the top of the melt pool. The top region is characterized by formation of heterogenous eutectic network structure with nano-scale refinement, labeled fine scale eutectic (Figure 12c). The crystal orientation map shown adjacent to the BSE micrograph in Figure 12c has been obtained from the middle part of the transverse cross section of the RS microstructure with the cellular α-Al phase. Large numbers of neighboring α-Al cells form groups of cells with identical or very similar orientations. This would be consistent with the reasonable conclusion that many of the cells grew epitaxially from the primary α-Al dendrites of the as-cast microstructure adjacent to the laser irradiation induced melt pool in the heat affected zone of the bulk metal substrate. Here, primary Al solid solution grains and the eutectic microconstituent can act as the seeds for growth of the cells behind a solidification interface that migrates along trajectories perpendicular to the isotherms in the melt-pool formed by the moving heat sources of the scanned laser beam.

As a major effect of the increase in the solidification rate a refinement of the microstructural features is observed. The cross-sectional size of the primary α-Al cells established by RS from the melt pool has been reduced by up to about 20-fold compared to the primary α-Al grains in the as-cast structure. Furthermore, the area fraction of the α-Al grains increased from 45% in the as-cast state to 58% after laser melting and rapid re-solidification. Conversely, the fraction of eutectic microconstituent decreased for the laser melted and re-solidified microstructure. These changes in the fractions of the primary and secondary solidification products can be attributed to the faster solidification velocity imposed by the condition established during laser surface remelting relative to the casting process. In the cellular region of the melt pool the

average diameter of the Al-phase cells is 2.7 μm and the intercellular regions with eutectic have dimensions of between 300-500 nm. SEM and TEM based EDS measurements performed by collecting spot spectra for the Al-phase cells in the central region of the RS microstructure consistently determined Cu supersaturation with an average content of 3.0 ± 0.4 at% Cu relative to the as-cast state with 2.3 ± 0.1 at% Cu and the equilibrium maximum solubility of 2.5 at% Cu.

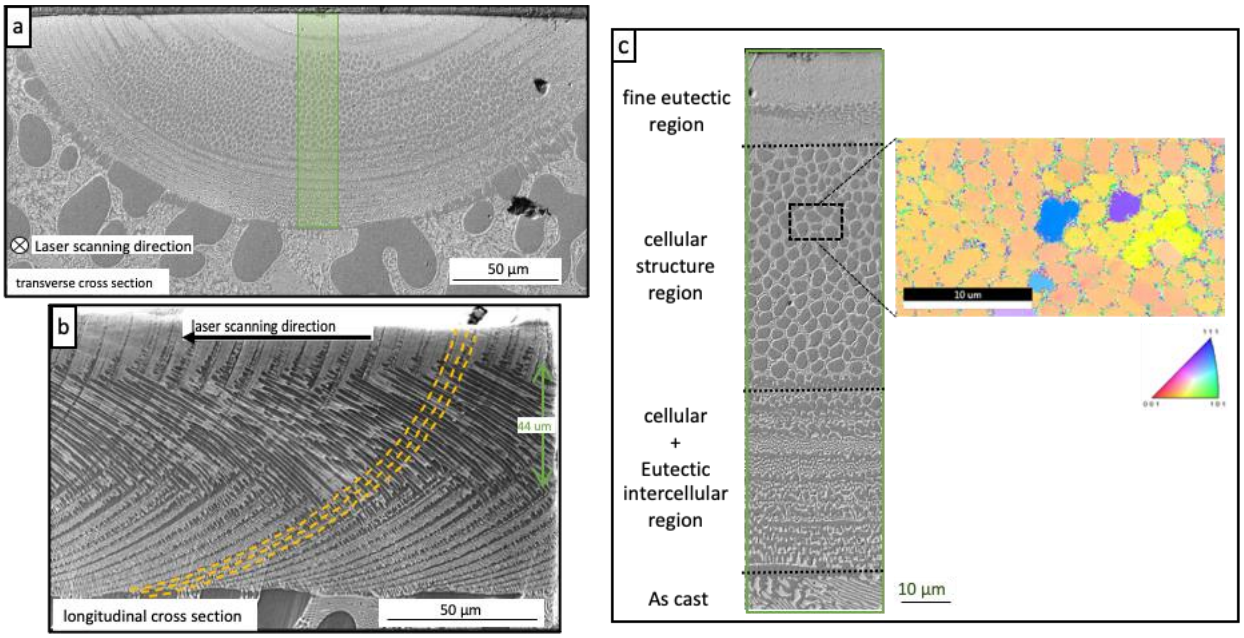

Figure 12 a) SE-SEM micrograph of transverse cross section of the melt pool, b) SE- SEM micrograph of longitudinal cross section indicating the isotherm.c) High magnification SEM image from the center of the pool showing the microstructure transition from bottom to top associated with orientation map of the cellular area.

4.2.1 Solidification Front Velocity Calculations

Microstructural analysis from the cross-sections of the scanned laser irradiation induced melt pool and the surrounding substrate of the Al-10Cu alloy showed that the scale of the

morphologically lamellar eutectic microconstituent changed in the scanned laser remelted regions relative to the as-cast state. The interlamellar spacing, λ, of the eutectic is affected by the scanned laser irradiation parameters, such as the laser scanning speed, the laser power and the laser spot size [15]. The lamellar eutectic wavelength, λ, decreased as the solidification front moved forward at increasing velocity, v, from the bottom towards the top of the melt pool, i.e., as the distance from the melt pool bottom, z, increases (e.g., Figure 12). From the longitudinal cross section, the lamellar eutectic wavelength, λ, was measured for the finer scale eutectic microconstituent formed by RS of the laser irradiation induced melt pool. For the eutectic in the as-cast state and for the heat affected zone λ values have been determined as 750 nm and 700 nm, respectively. For the eutectic regions located at the lower part of the longitudinal cross section of the melt pool the values of λ decrease from 620 nm to 230 nm as the distance from the melt pool edge at the bottom, z, increases, Figure 13. The numerical relationship between the interlamellar spacing, λ, vs. melt pool depth from bottom to top, z, is shown graphically in Figure 14a. The lamellar eutectic wavelength λ decreased rapidly, by about 50%, in the first 10 μm, $0 \leq z \leq 10\mu m$, then. For $z > 10\mu m$, wavelength λ decreased at a lower rate. This would be qualitatively consistent with a model where lamellar eutectic wavelength λ is inversely proportional to the square root of the melt pool depth, magnitude of z, giving $\lambda^2 = B\ z$, where B is a proportionality constant [8]. The rapid decrease in λ with increasing z correlates with the expected rapid increase of the solidification rate, v, from zero at the bottom of the melt pool as solidification ensues. A classic model for the diffusion controlled lamellar eutectic growth has been described by Jackson and Hunt [44] and gives the relationship between the characteristic lamellar scale, λ, and the average growth velocity, v, as:

$$v\lambda^2 = A$$

(4-1)

Here A is a constant, which has been determined previously as A=88 $\mu m^3/s$ for Al-Cu eutectic alloy [53]. The solidification rate, v, has been calculated using equation (4-1) and is plotted versus z in Figure 14b, where λ was measured from the longitudinal cross section with respect to z. A monotonic increase in the solidification interface velocity is associated with the continuous decrease of λ with increasing z, the distance from the bottom of the melt pool. For the minimum value of the experimentally measured eutectic wavelength, λ≈0.2μm, which is observed at z≈ (90±5) μm, a maximum solidification velocity of v=0.25 cm/s is estimated (Figure 14). This is consistent with prior research on laser induced RS microstructure evolution in eutectic Al-Cu alloys [16].

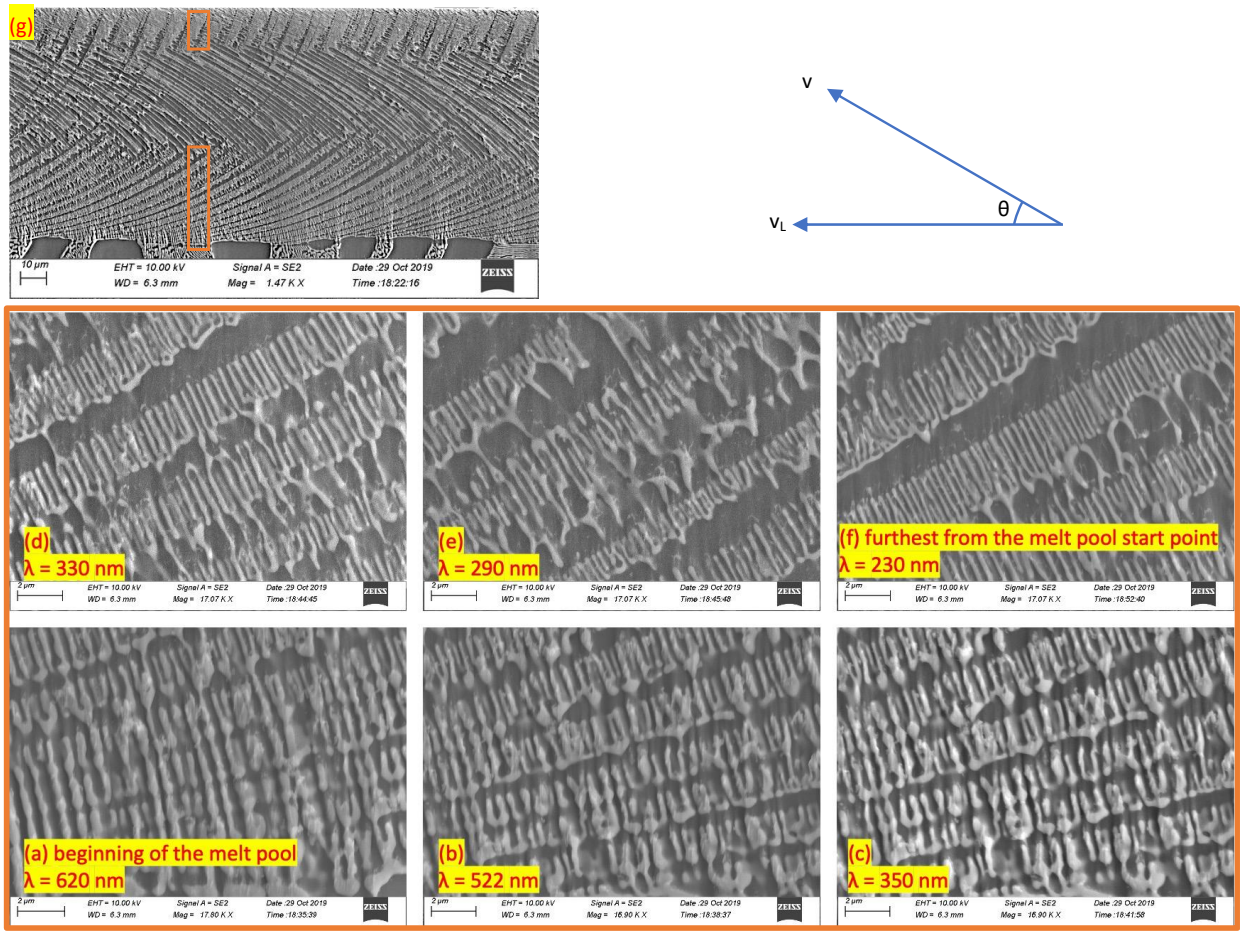

Figure 13 Secondary electron SEM images from bottom to top of the melt pool at longitudinal cross section where the interlamellar spacing is decreasing as the solidification front moves away from solidification onset. Images from (a) to (f) are taken from discontinous eutectic region highlighted in image (g).

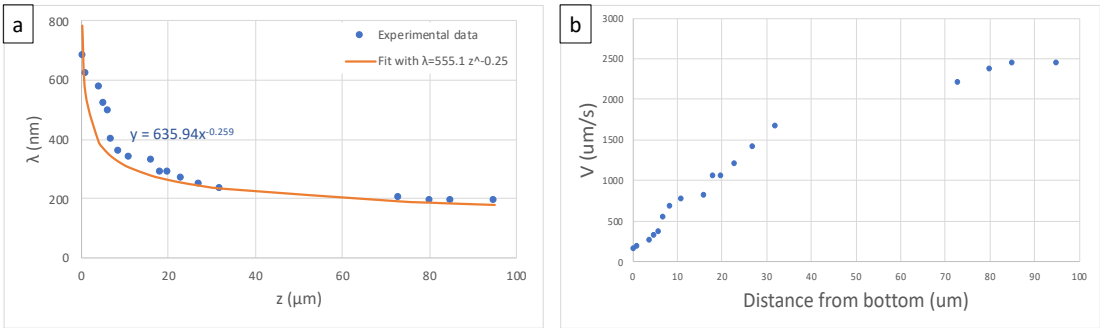

Figure 14 a) Interlamellar spacing, λ, versus melt pool depth from bottom, z, and the fit with λ=555.1-0.25, b) solidification front velocity verses melt pool depth from bottom.

The maximum solidification interface velocity, solidification rate or crystal growth velocity, v, is limited to the laser scanning speed, v_L, employed for the laser surface remelting, which here was v_L = 0.3cm/s. According to prior research on a cellular growth model during laser surface remelting [6], the crystal growth velocity, v, can be related to the laser scan speed as:

$$v = v_L \cos\theta$$

(4-2)

where θ is the angle enclosed between the normal of the isotherms in the melt pool, the nominal growth direction for the cell tips, and the laser scanning direction parallel to the surface (see inset in Figure 13). The ratio of the maximum crystal growth velocity derived from the scale refinement-based measurements of the lamellar spacing λ in the eutectic to the laser scan speed is $v / v_L = \cos\theta = 0.25/0.3 = 0.83$ and would imply a value of θ=33.6˚. In Figure 13 the angle θ for the part of the α-Al cell is narrowing from ≈ 70˚ at the lower part of the melt pool during the early stages of solidification related crystal growth to 25˚ at top of the melt pool. Hence, the solidification rate, v, estimated from the eutectic wavelength changes as function of location in the

melt pool, z, is at least qualitatively consistent with the expected growth direction change underlying the relationship $v / v_L = \cos\theta$. Notably, for an angle $\theta=70^\circ$ the solidification interface velocity is estimated as $v = v_L \cos(70^\circ)= 0.30*0.34$ cm/s ≈ 0.11 cm/s. For $\theta=25^\circ$ the increased solidification velocity is estimated as $v = v_L \cos(25^\circ)= 0.30*0.91$ cm/s ≈ 0.27 cm/s. According to equation (4-1) these solidification rates, v=0.11 cm/s and v=0.27 cm/s would correspond to eutectic wavelengths of $\lambda(v=0.11cm/s) \approx 0.28\mu m$ and $\lambda(v=0.27cm/s) \approx 0.18\mu m$, respectively. These microstructural scale metrics of the eutectic, λ, are in good agreement with the observations for z≈20μm in the early stages of α-Al cellular growth and z≈95μm at the very top of the melt pool (e.g., see Figure 14). Therefore, based on the microstructural analysis of the RS microstructure formed after scanned laser surface remelting with v_L=0.3 cm/s, it can be concluded that the solidification rate, v, for the region dominated by cellular α-Al has been in the range of 0.1 cm/s ≤ v < 0.3 cm/s (Figure 14).

Based on the dendritic growth model, an estimate of solute trapping during rapid solidification can be computed [40], [54]. For cellular/dendritic growth of the α-Al solid the solute trapping during rapid solidification is a function of dendrite radius tip, R, which, in general, has an inverse relationship with solidification velocity, v; i.e., $R = 2\pi\left(\frac{D\Gamma}{\Delta T_o kv}\right)^{1/2}$ in the high v range [40]. By adopting the prediction curve of R for dendritic growth as function of v and extending the curve to lower velocities [2], the tip radius of curvature for 0.1 cm/s ≤ v < 0.3 cm/s would be predicted to be in the range of 600 nm ≥ R ≥ 320 nm, Figure 15. The ≈ 50% reduction in R results in an associated increase in the velocity dependent solute portioning coefficient (k_v) from k_v=0.21 to 0.25 (i.e., a change by ≈14%). Therefore, an increase in the concentration of Cu solute in the growing solid Al solid solution crystal, C_s, is expected from C_s = 2.48at.% at v = 0.1cm to

C_s = 2.97at% at v = 0.3cm. The increased solute trapping predicted by the dendritic growth model for the α–Al cell growth rates observed during RS is in good agreement with the experimental composition measurements by EDS, 3.0 ± 0.4 at% Cu (see section 4.2). Table 2 shows the parameters used in the dendritic growth model calculations to predict the solid composition as function of solidification velocity, v, in detail along with the required interfacial undercooling.

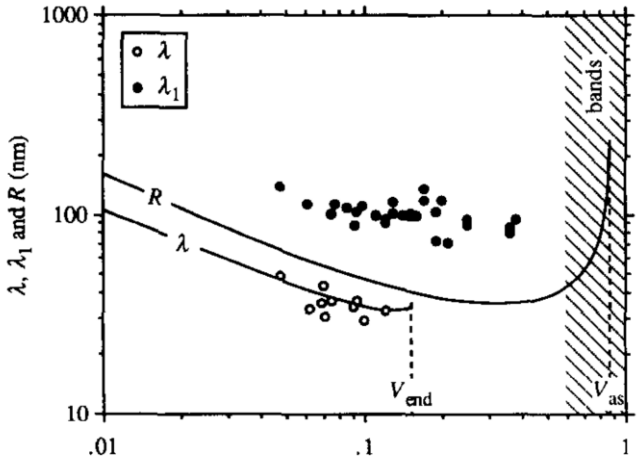

Figure 15 Predicted curve of dendrite radius of curvature, R. lamellar wave length scales for eutectics, l, as function of solidificaiton rate, v [m/s], from [2]**.**

Table 2 Solute trapping and undercooling predictions calculated as a function of grawth rate, v; Angle in the first column refers to θ in equation (4-2), $v=v_L \cos\theta$.

Angle (degree)	growth rate,v (m/s)	Dendrite tip radius,R (m)	Peclet number (Pe)	Portioning coefficient (kv)	Liquid composition (CL)	Solid composition (Cs)	Interface Temperature Ti(K)	Under cooling, 868-Ti
70	0.0010	6.00E-07	0.089	0.213	11.64	2.48	853.66	14.34
65	0.0013	5.10E-07	0.094	0.216	11.63	2.52	853.49	14.51
60	0.0015	4.70E-07	0.102	0.222	11.71	2.60	852.64	15.36
55	0.0017	4.40E-07	0.110	0.228	11.78	2.68	851.86	16.14
50	0.0019	4.10E-07	0.115	0.231	11.84	2.74	851.27	16.73
45	0.0021	3.90E-07	0.120	0.235	11.85	2.78	850.94	17.06
40	0.0023	3.70E-07	0.123	0.237	11.91	2.82	850.34	17.66
35	0.0025	3.50E-07	0.125	0.238	11.91	2.83	850.25	17.75
30	0.0026	3.40E-07	0.128	0.240	11.96	2.87	849.78	18.22
25	0.0027	3.35E-07	0.132	0.243	12.00	2.91	849.34	18.66
10	0.0030	3.20E-07	0.137	0.246	12.06	2.97	848.70	19.30

4.2.2 Probing the Mechanical Properties of RS Melt Pool

Nanoindentation hardness measurements have been performed on the as-cast structure as well as for the morphologically cellular region developed from the scanned laser melting induced melt pool. Figure 16 shows examples of SEM images depicting the locations and shapes of nanoindentations performed on the as-cast α-Al dendrites and the lamellar α-Al/θ-Al_2Cu eutectic microconstituent. The average hardness (H) values of the α-Al phase dendrites and the eutectic have been determined as 1.1±0.1 GPa and 2.8±0.7 GPa, respectively. Since the indent sizes are on the same scale as the size of the interlamellar spacing in the eutectic, the respective hardness measurements, H, vary over a relatively wide range depending on the exact indent location. Figure 16b shows typical load-displacement curves from some indents in Figure 16a with peak load of 1mN at room temperature. The as-cast α-Al curves exhibit large displacement with peak depth of ≈ 180nm. However, when the indent partially encounters θ-Al_2Cu phase the displacement reduced

significantly to about 110nm depth which translated to higher H values. The eutectic microconstituent exhibited hardness values ranging from as low as 1.7 GPa to as high as 6.2 GPa with an average of 2.8 GPa. The highest H value of 6.2 GPa was obtained when the indent is completely contained in and centered on θ-Al_2Cu phase (e.g., indent number 16 marked in Figure 16c and correspondingly Figure 16d). On the other hand, the hardness measurements of α-Al lamellae in the eutectic were as low as 1.7 GPa and up to about 2.6 GPa (e.g., indent numbers 5, and 10, respectively, as marked in Figure 16c and d, respectively by the correspondingly color-coded circles). Within the lamellar eutectic microconstituent the nanoindentation derived hardness values, H, of the α-Al lamellae are likely influenced by the effects from the neighboring and confining adjacent θ-Al_2Cu lamellae with their higher hardness. After inspection of the locations of the respective indents by SEM imaging it was possible to account for these possible effects from the microstructure on the hardness measurements. Only considering measurements obtained from regions associated with θ-Al_2Cu phase the corresponding hardness values have been determined to fall into the range of 4.5 GPa ≤ H ≤ 6.2 GPa. Hardness of single particle intermetallic phase of Al_2Cu have been investigated previously by instrumented nanoindentation and were found to be H=5.77±0.91GPa [47]. Also, using conventional micro-hardness and hardness tests (i.e. Vickers, Brinell etc.), the hardness values for θ-Al_2Cu phase have been reported to fall in the range of 4 – 6 GPa [55]. The nanoindentation hardness values determined here are consistent with published hardness values of θ-Al_2Cu. The nanoindentation hardness measurements performed for the as-cast microstructure of the Al-10Cu hypoeutectic alloy provide reference benchmark values for the α-Al phase of H=1.1±0.1 GPa, the coarse lamellar eutectic of 2.8±0.7 GPa, and for the θ-Al_2Cu phase of a hardness in the range of 4.5 GPa ≤ H ≤ 6.2 GPa.

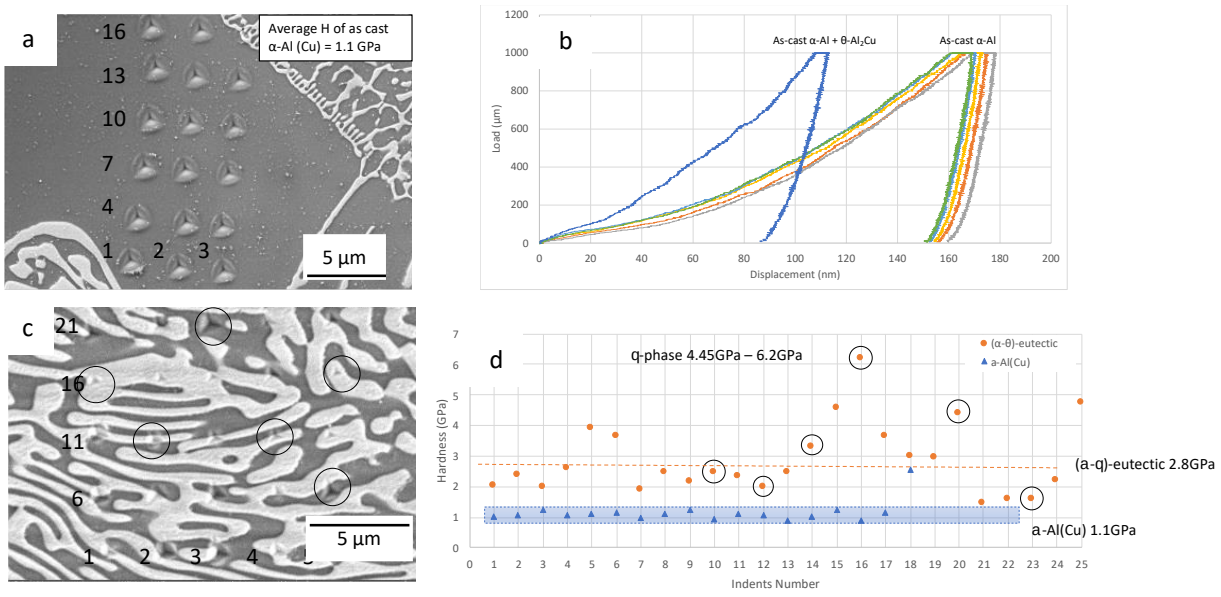

Figure 16 a) Secondary electron SEM images of a nanoindentation matrix on as-cast α-Al, were the numbers represent indvidual indentaion experiments, b) Typical load–displacement curves for the as-cast structure, c) SEM image of nanoindentation matrix on as-cast eutectic structure, d) chart showing Hardness vs Indentation experiment number performed for as-cast α-Al dendrites (blue triangles, i.e., from indentations shown in part a)) and the eutectic microstructure (solid lighter orange circles, i.e., from indentation locations shown in part c)). The colored semi-transparent circles in c) correspond to the same color encircled indentation hardness values shown in d).

Nanoindentations of the microstructure in the scale refined solidification microstructure of the melt pool were performed for the cellular morphology in the central region with a focus on the α-Al cells as shown in Figure 17 for example. Using multiple arrays of indents, the individual measurements were probing the cellular α-Al phase or the intercellular eutectic or both. The hardness values obtained from indentation experiments that have been confirmed via SEM imaging to probe to good approximation only the cellular α-Al fell into the range of 1.3-1.7 GPa with an average of 1.5 GPa ± 0.1 GPa, where the error is ± one standard deviation for at least ten

separate measurements. Here the error is a statistical standard deviation. The average H value measured for the intercellular fine scale eutectic was on average 2.7 GPa. For the indents probing both α-Al cell and intercellular α/θ -eutectic the hardness was on average 2.2 GPa. The α-Al phase in the cellular regions of the rapid solidification microstructure showed a significant hardness increase of about 0.4 GPa ± 0.2 GPa from the hardness of the as-cast coarse-scale α-Al phase with 1.1GPa ± 0.1 GPa. An increase of 0.4 GPa corresponds to about 36% of the hardness of the as-cast α-Al phase with Cu concentration of 2.3at% in solution. Figure 18 shows the longitudinal cross section of the laser trace with indents from nanoindentation experiments taken along an α-Al cell. Only indents fully located on α-Al cells were considered for the hardness measurements reported here for the longitudinal cross-section. The average hardness of the α-Al cell is 1.5 GPa ± 0.5 GPa, which is consistent with the hardness values, H, obtained for the cellular α-Al from the transverse cross section. However, there is an increased variability in the measured hardness for the longitudinal cross section of the cellular α-Al relative to the transverse cross-section measurements. The increase in variability of the hardness measurements from ±0.1 to ±0.5 GPa is attributed here to effects of the differences in the distances of the cellular grain boundaries for the volumes of the probed α-Al cells relative to the indentation volume. In transverse cross section the α-Al cells exhibit an equiaxed cross-sectional shape and the nanoindentation volume probed for an indent centrally located in the α-Al cell is always about equidistant from the cell (grain) boundaries. However, in the longitudinal cross section, the cells size (diameter) varies based on the cross-section angle, i.e., usually the cell size from the longitudinal cross section does not represent the true maximum cell diameter. Consequently, during nanoindentation, the indent fits the apparent size of the cell interior but for some fraction of the material volume probed below and adjacent to the indent the deformed material flow is hindered by a nearby cell boundary with the

intercellular θ-phase that is located below the surface of the metallographically prepared section, leading to an increase in the measured value of hardness, H. Notably, the hardness values along the α-Al cell remained constant with increasing distance from the melt pool bottom for both the measurements obtained from the transverse and the longitudinal cross-sections. Thus, it is concluded that the α-Al phase of the cells observed in the solidification microstructure after laser melting exhibits an increase in hardness by $\Delta H = 0.4\text{GPa} \pm 0.2\text{GPa}$ or about 36% relative to the hardness of the α-Al in the as-cast reference state.

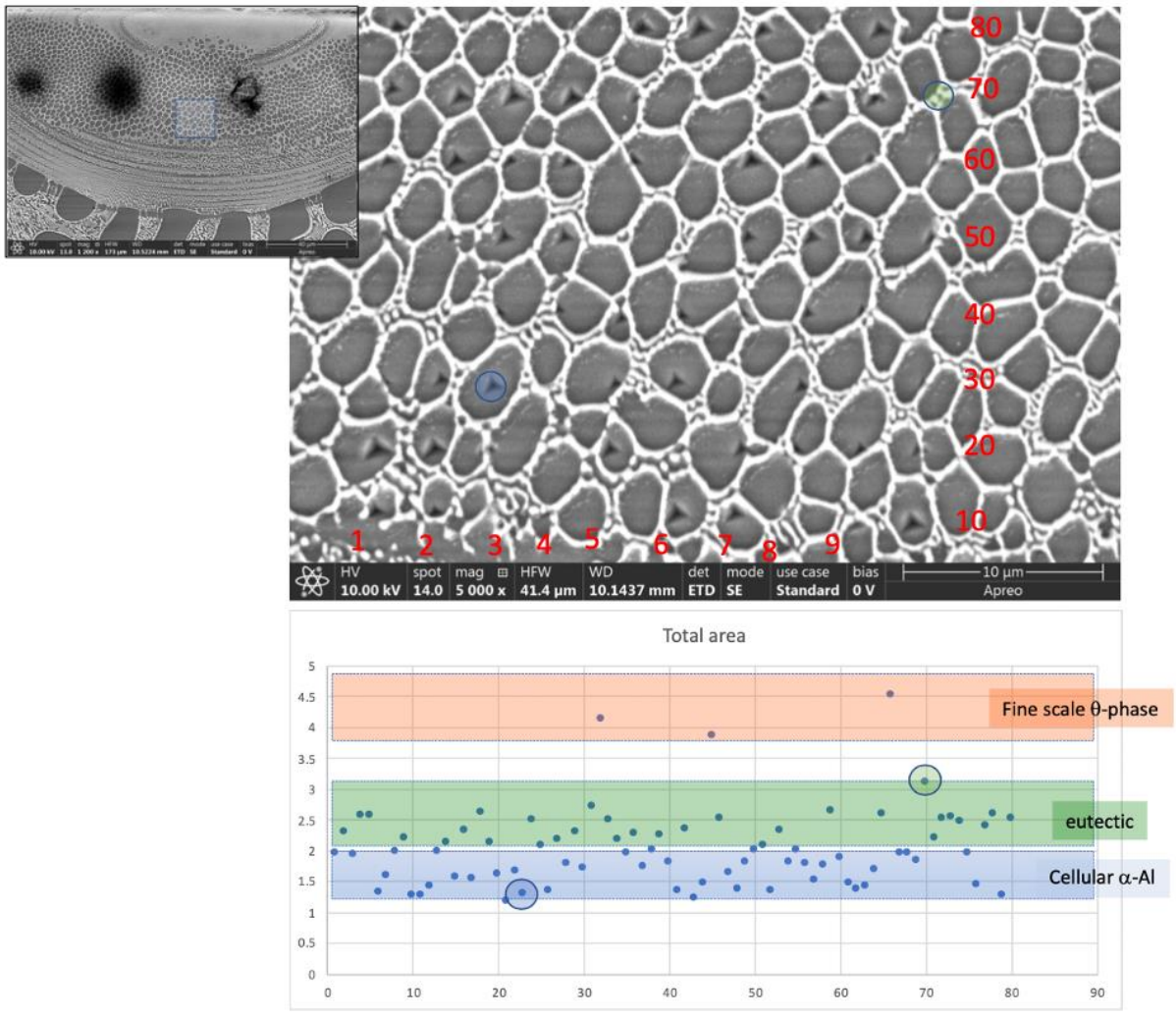

Figure 17 Secondary electron SEM image of a nanoindentation matrix (6x6) in the RS microstructure for the regions od cellular structure in the transverse cross section and respective hardenss charted for each indent. Mcroconsitutent or phase related locations identified by SEM imaging are marked by three color coded bands for the fine scale θ-phase and eutectic in the intercellular regions, and cellular α-Al solid solution grains.

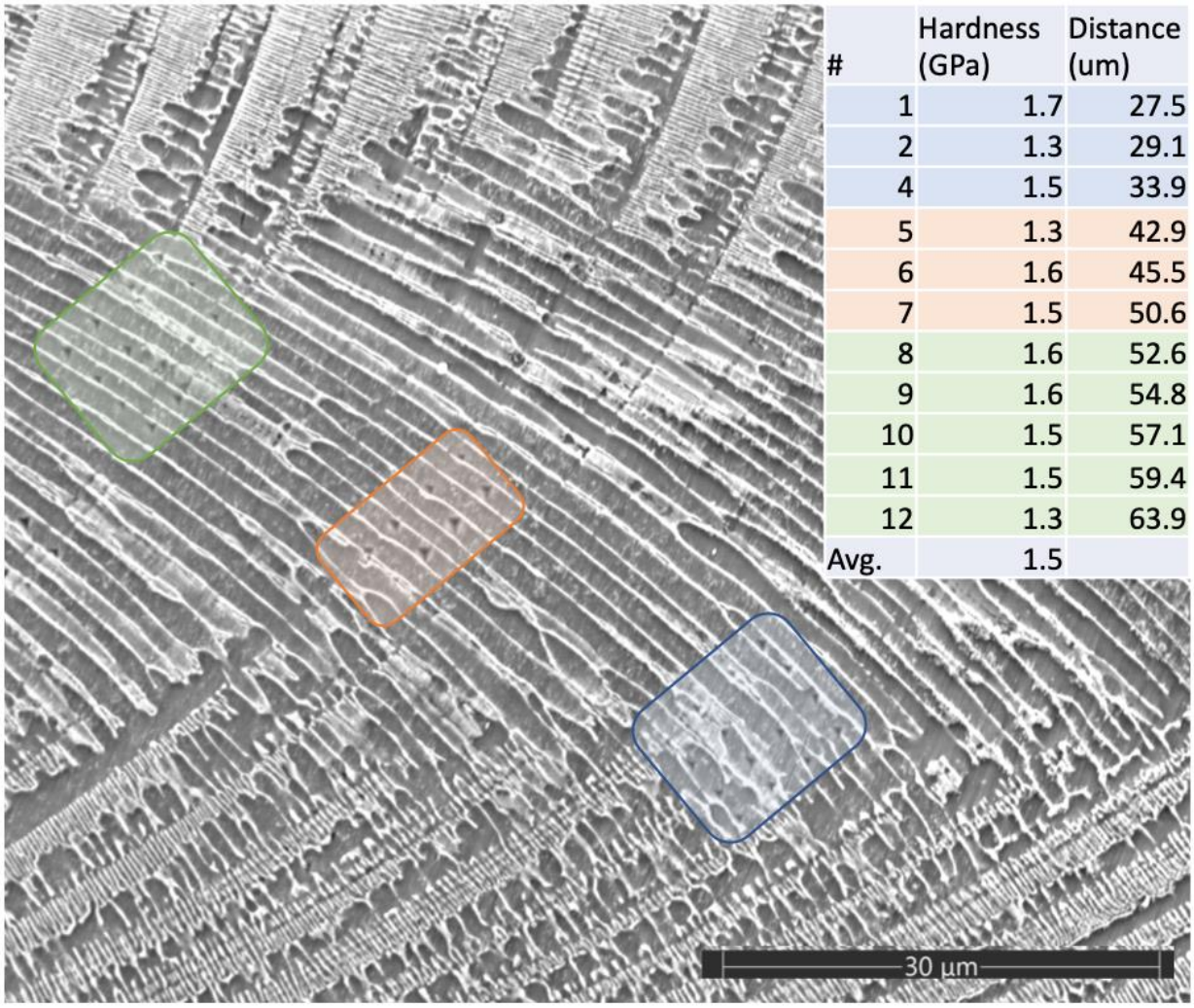

#	Hardness (GPa)	Distance (um)
1	1.7	27.5
2	1.3	29.1
4	1.5	33.9
5	1.3	42.9
6	1.6	45.5
7	1.5	50.6
8	1.6	52.6
9	1.6	54.8
10	1.5	57.1
11	1.5	59.4
12	1.3	63.9
Avg.	1.5	

Figure 18 Secondary electron SEM image of nanoindentation matrices on the cellular regions in the RS microstructure for the longitudinal cross section. Three matrices of indent sets located on the cellular structure.

4.2.3 Effects of Solute Trapping on Nanoindentation

Based on the location specific nanoindentation measurements conducted in Al-10Cu RS microstructure it has been shown that the hardness increased in the α-Al(Cu) cells established after scanned laser melting in the solidification microstructure relative to the α-Al(Cu) grains in the as-cast structure. Possible strengthening mechanisms responsible for the experimentally observed hardness increase in the α-Al phase after directional rapid solidification include precipitation hardening, solid solution (solute) strengthening and grain size strengthening. The possible contributions of these different strengthening mechanism to the increased hardness will be discussed in this section. The Al-10Cu alloy is hypoeutectic composition and therefore comprises two fundamentally different microconstituents; namely, the primary α-Al (Cu) solid solution phase and the eutectic, which is typically of lamellar morphology and comprised of α-Al(Cu) and θ-Al_2Cu. The size of the indent used in the nanoindentation measurements is too small to capture a single representative lamella in the eutectic microconstituents. Thus, in this analysis, the focus of nanoindentation measurements will be on the primary product of solidification from the alloy melt, the solid-solution microconstituent of α-Al(Cu) phase.

Supersaturated α-Al(Cu) solid solutions has face-centered cubic crystal structure and can be age-hardened very effectively by annealing in the temperature range of about 100˚C to 400˚C. Typically, the full sequence of precipitation during age-hardening of the Al-Cu alloys can be described as: Supersaturated Solid Solution (SSSS) ➔ plate like coherent GP-zones ➔ plate like coherent θ'' ➔ plate like semi-coherent θ' ➔ noncoherent θ (CuAl2) [56]. The age-hardened states that result in microstructures with large volume fractions of both θ'' and θ' have been found

to exhibit the maximum available increase in the alloy strength from precipitation strengthening mechanisms [57].

Figure 19 shows an SEM BSE image of the TEM lamella extracted from the central region of the solidification microstructure with the cellular morphology in the transverse cross-section, and the associated bright field TEM images. The α-Al(Cu) cells exhibit equiaxed shape in transverse cross-section view with an average diameter of 2.7 μm. The intercellular region has an average thickness of about 250 nm to 300 nm. Here Cu solute enriched liquid is expected to transform to eutectic α- and θ-phase as the secondary solidification product. Typically, single grains, crystals of θ-phase are found here, rather than the familiar lamellar morphology eutectic. The formation of a fine scale lamellar eutectic structure is also observed, but it is less common. Since the scale of the eutectic wavelength is larger or at best on the same order of magnitude as the width of the intercellular region, the formation of recognizable lamellar morphology is geometrically hindered. The relative scarcity of formation of lamellar morphology in the intercellular eutectic and the small scale of the intercellular regions are both attributed to conditions at the solidification interface deviating significantly from equilibrium during formation of the cellular morphology region in the solidification microstructure.

The α-Al(Cu) cells exhibit very similar contrast behavior in the TEM bright field image of Figure 19b. This implies that the diffraction conditions are likely similar or almost identical for the different α-Al cells and would be consistent with them having similar orientations relative to the electron beam. Nanoscale mottled dark contrast features can be discerned in the diffraction contrast images of the α-Al grains in Figure 19. These mottled features have been confirmed to be Ga enriched clusters or precipitates by EDS composition analysis. These features are therefore identified as artifacts introduced by ion implantation associated with irradiation damage during the

DB-FIB sample preparation. These features are an artifact from specimen preparation and are not indicating formation of GP zones or other precipitation of possible intermediate phases typically forming during aging of Al-Cu alloy SSSS. Selected area diffraction patterns (SADP) taken from the α-Al(Cu) cells confirmed their identical orientations, which is consistent with results from the SEM EBSD based crystal orientation mapping (Figure 12). The SADP of the α-Al cells only displayed diffraction maxima from the fcc lattice of the α-Al(Cu) solid solution. Weak maxima or streaks, which would indicate formation of GPZ or other transition phases, were not present. The TEM imaging, diffraction and EDS confirm that no precipitation occurred within the α-Al(Cu) cells formed in the solidification microstructure. In addition, precession electron diffraction (PED) based crystal orientation mapping has been with high spatial resolution (5nm step size). The resulting orientation maps and phase maps failed to reveal any diffraction signatures of the GP-zones or the possible precipitate phases. Some example PED patterns extracted from the region scanned (see rectangle in the BF image) are shown in Figure 20. The absence of precipitation in the supersaturated α-Al(Cu) cells, average Cu solute concentration of about 3at% Cu, implies that the rapid heat extraction during solidification after the melting by application of the scanned laser was sufficient to suppress the nucleation and growth of precipitates observed for typical solid-state ageing treatments in Al(Cu) alloys. Therefore, precipitation strengthening cannot have contributed to the measured increase in the hardness of the supersaturated α-Al(Cu) cells in the cellular region of the solidification microstructure.

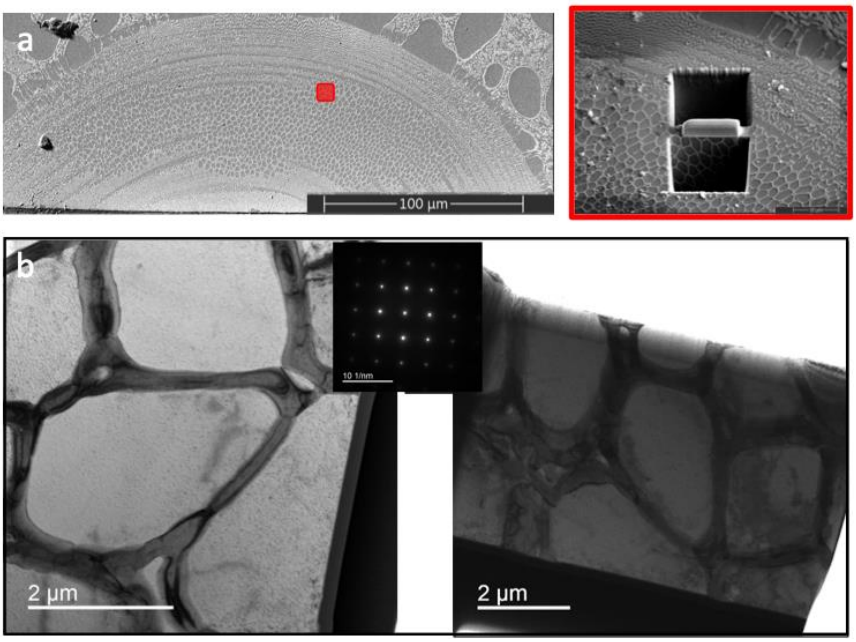

Figure 19 a) SEM image of transverse cross section showing the position of TEM lamella extraction, b) TEM bright field images and inset selected area diffraction pattern for [001] Al.

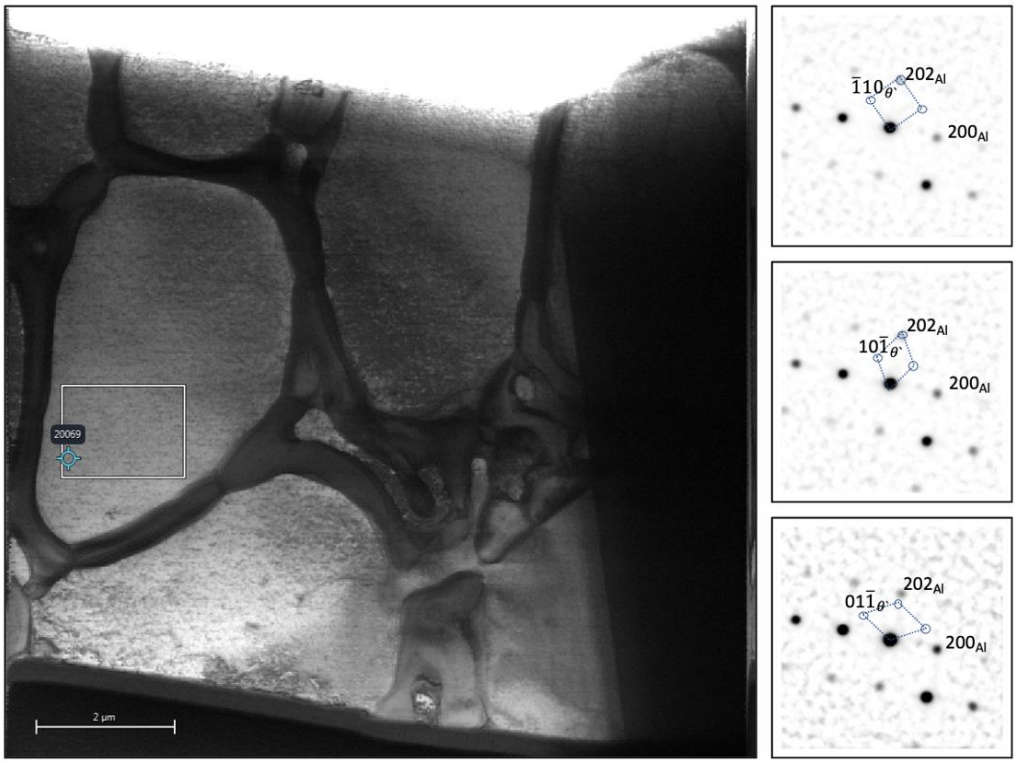

Figure 20 Precession electron diffraction (PED). The three possible equivalent variants of θ` phase are highlighted on the PED patterns [58]

The high cooling rate during the solidification after laser melting results in enhanced solute trapping and increased Cu content in the α-Al(Cu) solid solution [59]. The composition measurements determined a solute concentration in the α-Al(Cu) cells of the solidification microstructure of about 3 at% Cu. This is about 0.5at% or about 20% larger than the maximum Cu solubility of 2.5at% for the α-Al(Cu)-phase at the eutectic isotherm under equilibrium conditions. This non-equilibrium increase in Cu solute is expected to have effects on the hardness values of the α-Al(Cu) cells via the solid solution hardening mechanism. On a basic level, solid solution hardening is attributed to the attractive interaction between solute atoms and mobile dislocations [26]. The solute atoms create local stress fields in the host lattice. The interaction of the stress

fields of the dislocation and the solute atoms impede the dislocation movements and therefore cause an associated increase in the resistance to plastic flow and, thus, a hardness increase [60]. The local stress field associated with the solute atoms (i.e., Cu) substituted for the Al matrix atoms is primarily due to the size misfit parameter ε between the solvent and solute atoms [26]. Different models had been proposed to predict the solute strengthening effect [60], [61]. In general these models describe an increment in the resolved shear stress required for dislocation glide, $\Delta\tau_{SS}$, as a function of the solute concentration for a given host and solute atom combination, and are of the form [60], [62]:

$$\Delta\boldsymbol{\tau_{ss}} \approx \boldsymbol{\varepsilon^{p}\, c^{q}}$$

(4-3)

Here $\Delta\tau_{ss}$ is the increase in the resolved shear stress or flow stress due to solid solution hardening, ε is the misfit strain, and c is the atomic fraction of the solutes. p and q are model-dependent exponents. Labush's [60] and Leyson et al. [63], [64] developed models that have predicted an increase of flow stress that is proportional with $c^{2/3}$ in substitutional solute. They have related the volumetric misfit (υ_m) of Cu solute in Al matrix in predictions of the flow stress at yielding, $\Delta\tau_y$, as a function of solute concentration, c, [64] as in equation (4-4),

$$\frac{\tau_{y0}}{c^{\frac{2}{3}}} \approx \left(31.1 \pm 6.3 \frac{MPa}{\text{Å}^{-14}}\right) \Delta\, \upsilon_m^{\frac{4}{3}}$$

(4-4)

where τ_{y0} (MPa) is the yield stress at 0 K and υ_m is the volumetric for Cu solute in Al solvent and is given as υ_m = -5.57 Å^3. To estimate the percentage increase in yield stress by increasing c from 2.48 to 3.00 at% Cu, the predicted data from Leyson et al. [9] were used for the

extrapolations as shown in Table 3. Here the column labeled as '% increase' lists the relative increment in flow stress for each step relative to the prior lower level of solute concentration, e.g., the increase in solute concentration from 0.09at. % to 1.65at.% Cu is associated with a predicted increase in tensile yield stress by 864%, i.e., from 5.3MPa to 51.1MPa.

Table 3 Extrapolation Data

c %	Tensile yield tress (MPa)	
	Predicted	% increase
0.09	5.3	
1.65	51.1	864
2	61.9	21
2.48	76.8	24
3	92.9	21

From the results of the extrapolations for the solute strengthening effect for Cu in Al(Cu), which are based on the work by Leyson et al [9] and are shown in Table 3, the yield stress increase by 21% would be expected due to the Cu solute increase from 2.48 to 3 at%. Notably, the model by Leyson et al [9] was developed for the flow stress at yielding for T=0K, while the nanoindentation hardness is measured at room temperature, T≈298K. Assuming that the hardness increment measured in the experiments performed here for the Al(Cu) solid solution follows the same numerical behavior for solute strengthening as the resolved shear stress at yielding by Leyson et al [9], an increment by about 20% to 25% relative to the hardness of the α -Al(Cu) dendrites in the as-cast state would be a reasonable expectation for the increase in Cu solute concentration from 2.3at% to 3.0at% in the α-Al(Cu) cells of the solidification microstructure. The nanoindentation hardness measurements showed an increase of average hardness for the α-Al(Cu) cells relative to as-cast state α-Al(Cu) dendrites by ≈400MPa , i.e., from 1.1 GPa to 1.50 GPa. Since 0.4 GPa ≈ 0.36 x 1.1 GPa, it appears reasonable to conclude that about half of the 36% increase in hardness

observed experimentally, i.e., ≈200MPa, can be attributed to solution strengthening from the excess amount of Cu trapped during the rapid solidification crystal growth of the α-Al(Cu) cells of the solidification microstructure.

Grain size strengthening in polycrystalline metals can be described numerically by the relationship discovered by Hall [65] and Petch [66] according the following type of equation:

$$\sigma_y = \sigma_o + k\, d^{-1/2}$$

(4-5)

where σ_y is the yield stress in MPa, σ_o is the intrinsic strength of a hypothetical infinite size single grain (or a very large grain or single crystal in practice) in MPa, k is a constant that accounts for the contributions from the grain boundaries (GB) to increase in the strength measured in MPa $\mu m^{1/2}$, and d is the grain size in μm. Mathematically equivalent expression are used to describe this Hall-Petch effect or grain-size-effect for the hardness for most polycrystalline metals, including Al. Prior studies reported on the Hall-Petch effect in aluminum alloys [67]–[71]. For the yield stress the following values have been determined for the intrinsic material constants, σ_0 and k, for pure Al, $\sigma_o = 16\ MPa$ [72], $k = 65\ MPa\ \mu m^{-0.5}$ [73]. The average grain size (d) of the α cells in the central region of solidification microstructures has been determined as d=2.7 μm. According to equation (4-5), the total contribution to strengthening from a grain size effect for the yield stress increment for pure aluminum with a grain size of d=2.7μm would be estimated to be 55 MPa. The α-Al(Cu) cells of the RS microstructure and the dendrites in the as-cast state of the Al-10Cu alloy are solid solutions of Al with Cu rather than pure Al. However, effects on the between 2.3at% to 3.0at% of Cu solute present in the α-phase of the alloy on the stacking fault energy and thus on the dislocation glide morphology are not expected to be significant. Hence, it

appears reasonable to conclude that increments of the yield stress from the grain size reduction would be of similar magnitude for the α-Al phase in the alloy as are estimated for pure Al polycrystals.

The numerical relationship between the hardness (*HV*) and yield strength (σ_y) in fcc metals, such as Al, has been shown to be [62],

$$5.24 \cdot \sigma_y = HV \qquad \textbf{(4-6)}$$

Based on equation (4-6) an increment in the yield strength of 55 MPa is equivalent to a hardness increment of ≈ 290 MPa. The magnitude of this strength increment represents 19% of the total hardness measured for the α-Al cells, i.e., 1.5±0.1 GPa, and about 26% of the hardness measured for the α-Al(Cu) dendrites in the as-cast state, i.e. 1.1±0.1 GPa. The 400 MPa hardness increase of the α-Al (Cu) cells in solidification microstructure represents ≈36% of the hardness measured for the reference value measured for the cast α-Al. The hardness increase estimated to result from a grain-size-effect can account for a significant fraction of the experimentally measured hardness increment but not all of it.

No evidence for Cu-related precipitates has been found for the α-Al (Cu) cells in solidification microstructure (e.g., Figure 19, Figure 20). Hence, contributions from precipitation strengthening to the experimentally observed hardness increase for the α-Al phase in the solidification microstructure of the Al-10Cu alloy can be ruled out. Consequently, the origins for the experimentally observed increase in hardness must be associated with the solid solution strengthening mechanism and the grain size effect. Based on the numerical and theory-based assessments presented above, each of these strengthening mechanisms would be expected to

contribute significant fractions to the experimentally measured hardness increase of about 400 MPa. The estimated increase attributed to solid solution strengthening from an increase of Cu solute concentration from 2.5at.% to 3.0at% and grain-size strengthening due to reduced cell diameters of on average 2.7μm were found to be ≈220MPa and ≈290MPa, respectively. The simple addition of these estimates would give a hardness increase of ≈510MPa. This summed total hardness increase estimate exceeds the experimentally determined hardness increase of 400 MPa by about 110 MPa or 28%, i.e., 110 MPa = 0.275 (400 MPa). Considering the absolute error in the nanoindentation based hardness measurements for the α-Al cells in the RS microstructure and the α-Al dendrites in the as-cast state, both ±0.10 MPa, gives a hardness increment measured as (1.50 ± 0.10) GPa – (1.10 ± 0.10) GPa = (400 ± 200) MPa. Therefore, the estimated hardness increment associated with the combined contributions stemming from solid solution and grain-size strengthening of ≈500 MPa is in good agreement with the experimental measurements. In conclusion, it is reasonable to attribute the experimentally observed hardness increase in α-Al cells of the rapidly solidified microstructure established by laser surface remelting of the Al-10Cu alloy fir the laser scan speed of 3 mm/s used with the LENS system to a combination of solute and grain size strengthening, with each of these strengthening mechanisms making significant and about equal contributions.

4.2.4 Summary

A laser scanning system of a DMD SLM additive manufacturing system has been used to introduce scanned laser melting traces to an as-cast hypoeutectic Al-10Cu alloy button using a laser scan speed of 3 mm/s. The re-solidification of the scanned laser melted alloy produced a

solidification microstructure that formed mostly via a cellular growth mode for the primary α-Al phase and exhibited signatures of rapid solidification associated with significant deviation from equilibrium at the solidification interface. This demonstrated the feasibility of preparing solidification microstructures in a certain processing regime that is suitable for establishing non-equilibrium deviations. In comparison to the as-cast state, the resulting solidification microstructure of the Al-10Cu alloy developed much finer microstructural scale for the primary α-Al(Cu) and secondary lamellar eutectic microconstituents. The morphologically cellular α-Al(Cu) solid solution phase constituent exhibited solute trapping of Cu, resulting in non-equilibrium solute concentrations exceeding the equilibrium solid solubility limit. Instrumented nanoindentation experiments have been conducted for the morphologically different and characteristic regions of the as-cast and rapid solidification microstructure of the hypo-eutectic Al-10Cu alloy. Inspection of the locations of the individual nanoindentation experiments and the characteristic features of the indents in the alloy by SEM imaging ensured that hardness measurements specific to a given microstructural constituent and/or phase could be established for the rapid solidification microstructure with improved accuracy. The combination of nanoindentation and SEM imaging facilitated an experimental study of the mechanical properties associated with the non-equilibrium microstructural changes developed during rapid solidification in the Al-10Cu alloy. The experiments confirmed a strong effect of the scale refinements in the lamellar eutectic microconstituent on the mechanical properties. Using microstructural metrics, e.g., the changes in lamellar wavelength of the eutectic and in crystal growth direction of the primary α-Al cells, the value of the solidification interface velocity, v_{SL}, i.e., the local and average crystal growth rates, have bene determined. This permitted comparison of prediction from alloy solidification theory calculations of the expected concentration of Cu solute in the α-Al phase as a function of

solidification interface velocity with experimental composition measurements. This study provided quantitative experimental evidence for the combined effects of solute strengthening and grain size strengthening on the mechanical properties for α-Al(Cu) established in the cellular growth regime during rapid solidification of the Al-10Cu hypoeutectic alloy. The solidification microstructure of the Al-10Cu alloy was formed for solidification interface velocity up to about v=2.7mm/s=0.027cm/s=0.0027m/s. The experimentally observed scale refinement, e.g., α-Al cell diameter ≈2.7μm and eutectic wavelength λ≈0.28μm, and the level of solute trapping, ≈0.5at.% Cu, determined here indicated relatively small but significant deviations from equilibrium during the solidification after the low-speed (v_L=3mm/s = 0.3 cm/s = 0.003m/s) scanning laser surface remelting. The relatively small effects from non-equilibrium deviations during rapid solidification observed experimentally are consistent with predictions from alloy solidification theory. The Berkovich indenter tip instrumented nanoindentation experiments probed volumes in the α-Al phase on the scale of ≈1-2μm diameter. The nanoindentation volumes are too large to probe the properties of the individual phases of the scale refined lamellar eutectic microconstituent of the RS microstructure of the Al-10Cu alloy, However, the about 1-2μm spatial resolution afforded by the instrumented nanoindentation performed here was sufficient to probe the mechanical properties of the cellular α-Al phase, the primary microconstituent of the RS microstructure of the Al-10Cu alloy. The projected area of contact (A) for the Berkovich indenter tip at highest contact depth (h_c) of 0.16μm performed on α-Al cells would be $A \approx 0.63\mu m^2$ (see equation (3.2). This would give a diameter of about 1.1μm as the larges cross-sectional length of the triangular shape projected indented area, which is taken here as an approximate metric for the scale of the mechanically probed material volumes. It can be concluded that the spatially resolved

local mechanical property measurements via the instrumented nanoindentation for the selected conditions of indenter tip type and maximum load and loading, dwell time and unloading rate, facilitated probing of Cu solute trapping related effects on mechanical properties of α-Al phase solid solution crystal after rapid solidification at rates in the range of 0.1 cm/s $\leq$ v < 0.27 cm/s. This demonstrates the feasibility to utilize the approach of combining nanoindentation and microstructural characterization by electron microscopy imaging, diffraction and composition analysis to determine the mechanical property changes associated with the morphologically distinct, scale-refined and elemental composition modified microstructural features evolving in multi-component alloys, such as the hypoeutectic Al-10Cu, under non-equilibrium conditions during RS after laser melting.

4.3 Rapid Solidification at High Scan Velocity via Single Track Melt Trace

Scanned laser surface remelting has been performed for the hypoeutectic Al-10Cu alloy also at laser scanning speed larger than 3 mm/s. Increasing the scan speed of the laser, v_L, by two to three orders of magnitude up to 1000 mm/s $\leq v_L \leq$ 4000 mm/s, that is 1 m/ s $\leq v_L \leq$ 4 m/s, is expected to result in proportional increases of the maximum solidification rate (e.g., equation (4-2)). The relationship between the laser scan speed, v_L, and the local solidification rate or equivalently the local crystal growth velocity, v, described in equation (4-2), i.e., $v = v_L \cos\theta$, where θ is the angle between the local crystal growth direction and the laser scan direction, predicts that increases of solidification rates into the regime of 0.5 m/s $\leq$ v $\leq$ 3 m/s as maximum rates are reasonably expected. Utilizing faster laser scanning speed experiments in that range of

1 m/s $\leq v_L \leq$ 4 m/s would offer the potential to access solidification rate regimes where the rapid solidification microstructure evolution of the Al-10Cu alloy can access morphologies that include the formation of metastable phases, eutectic cell growth and potentially even banded morphologies [6]. The power of the laser should be adjusted appropriately to obtain melt pools with as close as possible to a semicircular transverse cross section and to avoid artifacts that would be expected to result from excessive key-holing and turbulence or gas bubble ingress into the melt pool.

To achieve high solidification rate, $v \geq 0.5$ m/s, for large fractions of the rapid solidification microstructure, which would provide access to the different morphology changes expected in hypoeutectic Al-10Cu alloy for solidification rates in the range of 0.5 m/ s $\leq v \leq$ 2 m/s, single melt traces were generated at high laser scan velocity, i.e., 1m/s, 2m/s and 4m/s, with a constant laser power of 380W. The dimensions of the transverse cross-sections of the RS microstructures resulting from the melt pools are shown in Table 4. The melt pool dimensions at laser scanning speed of v_L=2m/s were reduced by 71% in depth and 55% in width compared to those achieved for laser scanning speed of v_L=1m/s (Table 4). The melt pool dimensions at laser scanning speed of v_L=4m/s were reduced by 30% in depth and 10% in width compared to v_L=2m/s. The increase of the laser scan speed from v_L=1m/s to v_L=4m/s dramatically reduced the melt pool depth, reduction from 150µm to 30µm or 80%, while the melt pool width reduced from 225µm to 90µm or 60% (Table 4). The changes in the dimensions of the melt pool induced by the scanned laser irradiation are related directly to the scan speed, v_L, since the laser spot size and laser power were held at constant value s of ≈100µm and 380W, respectively, for all experiments. The size of the melt pool increased as the scan velocity decreased. Keeping both the laser power and the area irradiated by the laser beam constant the decrease in the scan speed, v_L, results in an increased amount of time in a given unit volume of the alloy is exposed to the areal energy density delivered

by the laser. Thus, an increased amount of enthalpy or heat is imparted to a unit volume of the alloy material as the scan speed, v_L, decreases. For the lowest scan speed, v_L=1 m/s, the largest dimension melt pools formed and exhibited key-holing defects (Table 4, Figure 21). As the scanning speed increased, 2 m/s $\leq v_L \leq$ 4 m/s, the key-holing defects were reduced and especially the depth dimensions of the melt-pool decreased drastically, i.e., from 150μm at v_L=1 m/s, to 45μm at v_L=2 m/s, and to 30μm v_L=4 m/s, respectively (Table 4, Figure 21). The melt pool width is constrained by the laser spot size, which is constant in each of the experiments. The maximum width dimension of the melt pools imparted by the scanned laser irradiation decreased less rapidly than the depth dimension as the scanning speed increased. The melt pool width of 225μm exceeded the laser spot diameter ≈100μm by about a factor of two for the scanned laser surface remelting performed with the 1m/s scan speed (Table 4). This implies that for this scan speed the laser energy deposited per unit time and area resulted in very large superheating of the melt. Since the large amount of excess heat in the initial melt is transported effectively by conduction into the surrounding solid substrate significant melting of volumes of alloy located adjacent to the laser irradiated areas occurred. For the larger laser scan speeds of 2m/s and 4m/s the width dimensions of the melt pool are approximately equal to the laser spot diameter, Table 4. For the two largest laser scan speed limited melting or no melting was induced subsequently to the laser irradiation exposures during the time periods elapsing after the scanned laser irradiation and the onset of the re-solidification. It can be concluded that the duration over which the liquid state persisted for the regions which form the RS microstructures after the scanned laser irradiation passage were considerably longer for the 1m/s scanning speed processing than for the 2m/s and 4m/s scans.

Table 4 Melt pool dimensions created at different scan velocity

Laser scan velcity	1 m/s	2 m/s	4 m/s
Depth (µm)	150	45	30
Width (µm)	225	100	90

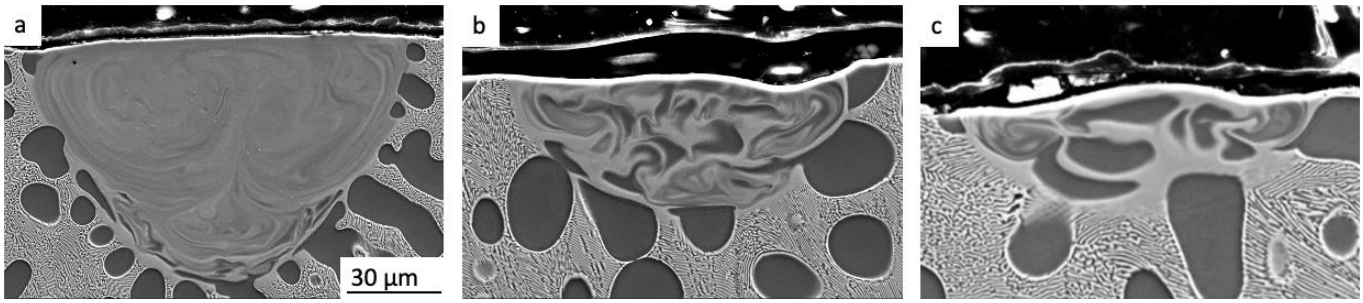

Figure 21 SEM micrograph of transverse cross section of example RS microstructures formed from melt pools created by a single laser pass at scanning velocity a) 1m/s, b) 2m/s and c) 4m/s.

The microstructure of the as-cast substrate of the Al-10Cu alloy comprises micron-scale size microconstituents in the form of the primary α-Al(Cu) solid solution dendritic grains and the lamellar eutectic in the interdendritic region (Figure 11 and Figure 21). The eutectic isotherm at ≈548˚C represents the melting temperature for the eutectic microconstituent, while, depending on exact Cu concentration, the α-Al(Cu) grains of the substrate would melt at a higher temperatures (T_m) of ≈580˚C < T_m < 660˚C [74]. Furthermore, the eutectic microconstituent has on average a composition with about 17at% Cu and the α-Al(Cu) grains are much leaner in solute concentration with on average 2.3at% Cu. The solidification process is directional and involves epitaxial growth from the substrate. Similarly, melting starts at the surface and extends laterally and in depth into the alloy substrate, creating a superheated alloy melt. Transport of the superheat from the liquid

alloy melt into the surrounding solid alloy substrate reduces the total amount of superheat in the liquid and the spatial thermal gradient in the liquid. While the solid substate warms up in the vicinity of the solid-liquid interface the spatial thermal gradient in the solid also decreases, albeit at a slower rate than in the liquid. This results initially in further melting of the substrate, an expansion of the melt pool after initial and extremely rapid conversion of the photon energy delivered by the scanned laser pass into heat (enthalpy) [75]. The post-laser-irradiation of the initial melt pool is quite pronounced for the 1m/s scanning speed laser trace (Figure 21, Table 4). While the maximum dimensions of the melt pool are established and before the onset of directional solidification, the temperature at the perimeter where the liquid alloy is in contact with the solid alloy substrate is the local melting temperature of the solid. As a result of the differences in the melting temperatures for the two characteristic microconstituents of the hypoeutectic Al-10Cu alloy, the melt pool extends a little bit deeper into to the solid alloy where the liquid is in equilibrium with the lower melting temperature eutectic microconstituent than in the regions where the α-Al(Cu) phase is in equilibrium with the liquid alloy. For example, Figure 22a shows two different melt pool depth at different phases. In the α-Al dendrite, the melt pool identified by a darker narrow line in the SEM BSE micrograph which indicates Cu depletion region (see Figure 22a) where the melt pool boundary at the eutectic microconstituent starts ≈ 3μm deeper. These local effects of the substrate composition on the solid-liquid interface that develops after laser irradiation melting is also reflected by the eutectic α-Al lamellae being longer than the eutectic θ-Al_2Cu lamellae (Figure 22b). Figure 23 depicts and enlarged SEM BSE micrograph of the depletion region at the onset of melt pool from α-Al dendrite phase. It also shows faint epitaxial growth of cellular morphology. Thus, the liquid alloy formed initially in equilibrium with the adjacent substrate prior to onset of solidification growth will exhibit Cu concentration variations

that stem from melting of the microconstituents of the as-cast substrate with the distinctly differing Cu solute content, giving rise to high Cu concentration when melting the eutectic and low Cu concentrations when melting the dendrites (Figure 22). The spatial scale of these high concentration and lower concentration regions in the alloy melt should at least initially correlate with the cross-sectional area of the respective microconstituents with the solid liquid interface. The scale over which diffusion in the liquid can homogenize the alloy melt can be estimated. The time, t, required to redistribute the Cu in the alloy melt over alloy a microstructure dimension of x≈50μm would be estimated by

$$t = \frac{x^2}{2D} \quad \textbf{(4-7)}$$

And the diffusion coefficient (D) is

$$D(T) = D_0 e^{\frac{-Q}{RT}} \quad \textbf{(4-8)}$$

where, D_o is temperature - independent diffusion of Cu in liquid Al = 1.07×10^{-9} m^2/s, Q is the respective activation energy for diffusion of Cu in liquid Al with Q= 24000 J/mol, R is the gas constant = 8.31 J/mol-K, T is the absolute temperature = 1173 K and t is diffusion time (s) [18]. Thus, the predicted time to homogenize composition over length scales of x≈50μm is t ≈ 0.35 seconds. This time is clary not sufficient to homogenize the 50μm before rapid solidification starts, since the BSE SEM micrographs of Figure 21 exhibit signatures of significant Cu concentration variations on that order of length scale. The time needed to complete the rapid solidification (RS) in thin films of Al-11Cu alloy after pulse laser melting is t_{RS}≈80μs=80×10^{-6} s ≈ 0.0001 seconds [3].

Even though, the volume in the scanned laser surface remelt traces is larger than a thin film and RS will take longer than in the nanometer thin films, comparison with the time required for diffusional mixing over ≈50μm length scales, $t=3.5x10^{-1}s$, shows that it is about 3500 times longer than reasonable estimates for time required to achieve RS. The mixing of the solute and solvent atoms in the liquid by convection and turbulence is associated with more effective mass transport than diffusional mixing in the liquid alloy. If the liquid state does not persist for sufficiently long times to permit complete mixing and homogenization of the Cu concentration gradient resulting over length scales of the dendrite arm spacing in the as-cast alloy substrate microstructure, then the solidification process would not involve crystal growth into a liquid with homogenous composition. This would result in rather heterogeneous conditions during solidification and would be expected to result in more complex solidification microstructures than those resulting from directional growth of the solid into a liquid with homogeneous composition. When the scale of the spatiotemporal composition variations in the liquid are smaller than the respective characteristic length scale of the growing solid, a homogenous liquid is established.

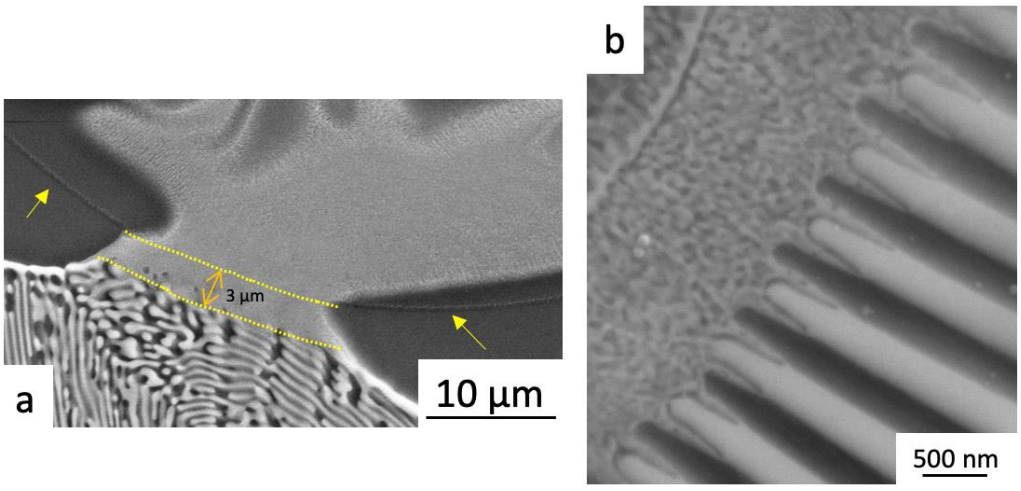

Figure 22: SEM BSE micrograph of RS microstructure formed at melt pool perimeter, a) the arrows show the boundry of meltpool with solid α-Al dendrites of substrate and the dashed lines enclose the additional melt

depth achieved for the lower melting temperature eutectic microconstituent of the solid substrate. b) shows the diffence melt depth between eutectic α-Al and θ-Al_2Cu phase and the change in eutectic growth morphology under RS conditions resulting in scale refined and morphlogically wavy ('free growth') eutectic product.

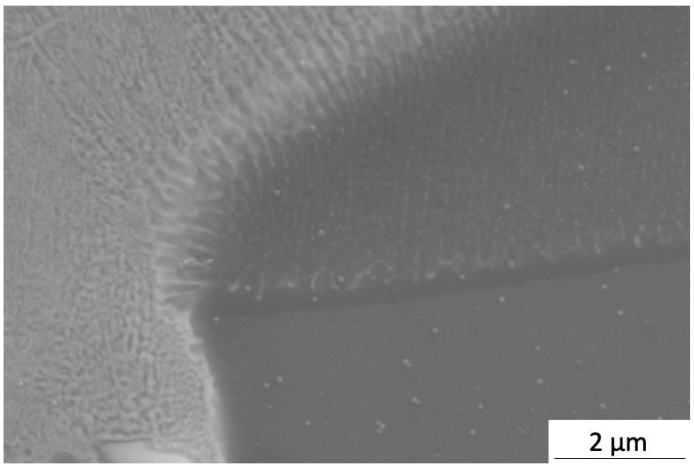

Figure 23 SEM BSE image reveailing a Cu depleated region at onset of RS grwoth into the melt pool from α-Al denderite of substrate. The bright contrast spherical features presnenting on the a-Al region of the susbtrate and RS grown region are silica nanoparticles remaining as artifacts from the smaple preparation due to imprefect cleangin prior to SEM imaging.

The solidification of the Al-10Cu alloy begins when the excess latent heat from crystallization that evolves upon liquid transforming to solid crystal can be transported in the majority into the solid substrate in addition to the superheat from the liquid melt pool. Solidification proceeds by epitaxial growth of new solid into the liquid along directions nominally perpendicular to the local isotherms. The solid of the substrate in contact with the liquid alloy melt seeds the growth locally. Effects from the compositional heterogeneity of the alloy melt and from the different crystal growth behaviors expected for seeded epitaxial growth from the tow different microconstituents of the alloy substrate have been observed for the solidification microstructures obtained by the single pass scanned laser melting at the higher scan velocities, 1 m/ s $\leq v_L \leq$ 4 m/s (Figure 21, Figure 22, Figure 23).

At the onset of solidification at the perimeter of the melt pools different morphologies which are dependent on the details local alloy substrate microstructure evolve. At the eutectic regions of the substrate, the heat-affected zone in the solid adjacent to the growing melt pool established a solidification microstructure comprised of very fine scale eutectic microconstituent (Figure 21, Figure 22, Figure 23). At some locations where the α-Al cell/dendrites of the substrate were in contact with liquid alloy, a very narrow Cu solute depleted region has been detected, which formed from the liquid prior to a modified eutectic product with a cellular growth morphology involving an α-Al phase matrix and secondary and discontinuous fine scale θ-Al_2Cu phase (Figure 21, Figure 22, Figure 23). The latter growth morphology, previously termed α-cells, has been reported for rapid solidification microstructures in Al-Cu alloys [9], [14], [76]–[78]. After crystal growth for about the first 10 – 15 μm the microstructure consists of mixed α-Al cell and fine θ-Al_2Cu, Figure 21. It is clear from these example observations that the initial stages of solidification after single pass scanned laser melting at the higher scan velocity in the range of, 1 m/s ≤ v_L ≤ 4 m/s, are affected significantly by the heterogeneity existing at the solid-liquid interface.

For the high velocity scan rates and a power of 380W in the nominally 100 μm width laser beam the resulting solidification microstructures revealed effects from the very significant compositional changes in the eutectic and pro-eutectic regions of the as-cast Al-10Cu alloy substrates. The single melt traces applied at these high scan speeds, which are required to attempt accessing crystal growth regimes that approach or extend beyond the limit of coupled multi-phase growth in the hypoeutectic multicomponent Al-10Cu alloy, maintain the melt for insufficient time durations to achieve complete compositional mixing of the Al and Cu atoms in the liquid state prior to solidification. As a result, the compositional heterogeneity that persists within the melt pool is reflected in the solidification microstructure. Hints of the convectional mass transport in

the liquid alloy melt appear to be preserved as frozen-in compositional variations evident in the atomic-number and orientation sensitive BSE SEM micrographs of Figure 21, Figure 22 and Figure 23. Hence, the fast scan laser velocity, 1 m/s $\leq v_L \leq$ 4 m/s, cannot work properly with a single trace of for Al-10Cu system if the characteristic scale of the hypoeutectic microstructure corresponds to a significant fraction, i.e., on the order of 1/10 or larger, of the cross-sectional dimensions of the laser irradiation induced melt pool. This has implications for example in SLM additive manufacturing where constraints on compositional mixing by thermo-capillary convection plays an important role in single layer built components [79].

Thus, in order to form rapid solidification microstructure that follows predictions associated with assumption of a liquid of homogeneous composition, i.e., to observe the characteristic transitions of planer/cellular, cellular/dendritic, columnar growth with continuous/discontinuous Al_2Cu and eventually banded region as the solidification rate increases, it is necessary to avoid any complex effects from compositional variations at length scales that exceed those characteristic of the evolving RS microstructure morphologies. Since the latter involve micrometer scale refinements after transition from planar interface morphology to dendritic cells it implies that the microstructural scale of the substrate from which seeded growth initiates should be self-similar in morphology and average composition at the micrometer length scale.

4.4 Rapid Solidification Microstructures for Multiple Pass High Scan Velocity Laser Remelting

The rapid solidification microstructures evolving after surface remelting of the as-cast Al-10Cu alloy by a single trace at high laser scan velocity, 1 m/s $\leq v_L \leq$ 4 m/s, developed complex microstructural features (see section 4.3). These features have been attributed to effects from the relatively large scale of the compositionally significantly different pro-eutectic and eutectic microconstituents in the as-cast state of the hypoeutectic Al-10Cu alloy, which were associated with insufficient compositional mixing in the alloy melt prior to re-solidification and heterogeneity during the seeded epitaxial crystal growth from the solid substrate into the alloy melt pool. Due to the significance of constitutional (composition) effects the simple relationship of a monotonically increasing solid-liquid interface velocity, v_{SL}, as the solid-liquid interface migrates towards the center of the melt pool, which held to good approximation for most of the rapid solidification microstructure developed in the case of scanned laser surface remelting with a slow scanning speed of $v_L = 0.003$ m/s, (see section 4.2), is no longer easily applicable for single pass scanned laser remelting at high scanning speeds, 1 m/s $\leq v_L \leq$ 4 m/s, of the as-cast Al-10Cu alloy. It is proposed here that mitigation against such undesirable effects from the microstructure of the as-cast Al-10Cu alloy on the evolution of the resulting rapid solidification microstructure requires an alloy melt that is very well mixed compositionally. A liquid alloy melt with a homogeneous composition would support conditions in the liquid ahead of the growing solid that are self-similar everywhere along the perimeter of the evolving melt pool and minimize the effects of differences in the thermal and compositional fields in the liquid on the solidification behavior. Furthermore, establishing a refined microstructural scale in the solid alloy substrate that affects the seeded epitaxial growth at

the onset of re-solidification is desirable (see section 4.3). It would enable a quick transition of the growth conditions at the solid-liquid interface to a state where thermal effects become dominant over constitutional (composition) effects. In combination the improved compositional homogeneity of the liquid alloy and the refined scale microstructure of the solid substrate would facilitate experimental investigation of the relationships between the solidification rate, the different rapid solidification microstructure morphologies resulting for characteristic critical solidification rates and the associated mechanical properties of the multicomponent and multiphase Al-10Cu alloy for the high solidification velocity regime of $v_{SL} \geq 0.5$m/s. For the hypoeutectic alloy Al-10Cu crystal characteristic growth mode transitions have been shown to occur at critical solidification interface velocities, v_{Sl}, e.g., for transition from the regime of coupled-phase growth to single-phase growth for $v_{SL} \approx 0.8$m/s [3]. To facilitate solidification behind solid-liquid interfaces migrating at rates approaching 1m/s it is necessary to apply scanned laser remelting scan speeds at rates on the order of 2m/s to 4m/s, see equation (4-2).

Figure 21, showed that for a single pass of the scanned laser a scan velocity of 2m/s resulted in the optimum hemispherical shape melt pool for the Al-10Cu alloy. Furthermore, Figure 21 illustrated that the rapid solidification microstructure exhibits a significantly refined scale when compared to the as-cast state bulk substrate. Since increased time duration in the liquid state prior to solidification permits for more time for mixing it is expected to improve the alloy melt compositional homogeneity. This is confirmed by Figure 21, which shows that for a scan velocity of 1m/s the melt pool had developed the highest level of homogeneity when compared to the cases of 2m/s and 4m/s scan velocity. Two different multi-pass scanned laser surface remelting strategies have been employed here to facilitate formation of rapid solidification structures by the migration of a monotonically accelerating solid-liquid interface into a liquid alloy that has a homogenous

composition (is compositionally mixed very well). One strategy applied multiple scanned laser-melting passes with a fixed laser velocity of 2m/s and constant power of 370Watt. This approach would increase the total time available for mixing in the liquid state and would advantageously utilize refined microstructural scales in the remelted solid. The multiple remelting strategy with a constant scan velocity will help development of understanding of the effect of the seeded growth from the Al-10Cu cast material on the rapid solidification microstructure evolution involving liquid alloy melts with different levels of compositional mixing. A second multi-pass scanned laser surface remelting strategy involved two different scan speeds. First, using a lower scan speed of 1m/s a larger melt pool has been created and application of multiple passes is expected to deliver enhanced the compositional mixing in the melt and refinement of the scale of the RS microstructure. Subsequently, multiple laser scans at a higher scan speed of 2m/s or 4m/s have been applied to create shallower melt pools. Seeded epitaxial growth of the new solid from the refined scale microstructure established by the 1m/s laser remelting scans would then facilitate the RS microstructure formation in response to the 2m/s and 4m/s scanned laser remelting. Hence, the role of the microstructural refinement of the solid substrate that seeds the growth of the RS microstructure can be evaluated and contrasted with the RS microstructures formed from the coarser scale as-cast alloy substrate. Table 5 (which is repeated here as new table from prior sections, i.e., Table 1: EOS nine laser traces conditions in section 3.2, for convenience) summarizes relevant parameters applied to create the nine different scanned laser surface remelting traces developed under this plan.

Table 5 EOS nine laser traces conditions (repeated here as new table from prior sections; i.e. table 1 in section 3.2).

Single laser trace				
Trace #	laser scan speed	# of passes		
1	2 m/s	2		
2		4		
3		6		
Two laser traces on top each other				
	larger melt pool		smaller melt pool	
Trace #	laser scan speed	# of passes	laser scan speed (m/s)	# of passes
4	1 m/s	3	2 m/s	1
5		6	4 m/s	
6		3	2 m/s	2
7		6	4 m/s	
8		3	2 m/s	3
9		6	4 m/s	

This chapter presents and discusses experimental studies of the effect of the laser scan velocity changes on surface remelting Al-10Cu hypoeutectic alloy with specific focus on analyses of the solidification rate and solidification microstructure morphology transitions, as well as the impact of the scale of the solid substrate microstructure on the resulting resolidified microstructures. Section 4.4.1 discuss the effect of multiple laser scan at fixed velocity on the RS microstructure evolution. Two cross sections will be analyzed, namely, transverse cross section and longitudinal cross section, to develop full understanding of the melt pool formation. The subsequent section (4.4.2) examine the effect of having multiple concentric melt pools created at different velocities by having SEM BSE imaging of transverse cross section.

4.4.1 Microstructure Changes as Function of Growth Velocity in Multi-Component Alloy for Multiple Scanned Laser-Melting Passes at Fixed Laser Velocity of 2m/s

In rapid solidification (RS), the heating source movement during scanned laser surface remelting causes complex convection behavior in the interaction volume of the laser beam with the material, which invokes drag forces and strongly influences the solid-liquid (S/L) interface growth direction. Since the scanned laser beam, i.e., the moving heating source, has a power density with a Gaussian profile, different mutually orthogonal cross-sectional views of the rapid solidification microstructure are required to study the microstructure evolution. Here, transverse cross section and longitudinal cross section views have been used to investigate the RS microstructure evolution during multiple laser scan velocity at fixed velocity of 2m/s. The transverse cross section is perpendicular to the laser scan direction and the longitudinal cross section is parallel to the laser direction. The laser traces labeled as #1, #2 and #3 in Figure 24 have been obtained by exposure to scanned surface remelting with a scan speed of 2m/s for 2, 4 and 6 consecutive scan passes, respectively. The average melt pool depth and width established by the multi-pass scanned surface remelting at scan speed of 2m/s have been determined as 70±10μm and 125±10μm, respectively. The maximum dimensions and shapes of the melt pools appear to be largely unaffected by the number of scan passes. The melt pool dimension is a function of laser scan speed, shape and power density. These parameters are kept fixed for each scan pass at a given scan speed. However, the number of laser scan passes performed at constant velocity, beam diameter and power affected the compositional homogeneity of the resulting final RS microstructure. The rapid solidification microstructure evolved from the melt pool produced by two consecutive scans at 2m/s scan speed, trace #1, is very inhomogeneous (Figure 24a). In the

composition and orientation sensitive BSE SEM images of trace #1 signatures of convection loops in the liquid present in the form of the strong composition related contrast (Figure 24a). The total fraction of regions of the RS microstructure with signatures of compositional inhomogeneity in the BSE contrast SEM images decreased for the traces #2 and #3 after application two and four additional scanned laser remelting cycles (Figure 24b and c). For trace#2 and trace#3 the regions exhibiting contrast signatures in the BSE SEM images associated with compositional inhomogeneity extended by up to 36μm and up to 22μm from the boundary with the as-cast substrate into the re-solidified microstructure. These linear dimensional measurements were taken from the bottom perimeter of melt pool centerline of the transverse cross sections. After two scan passes, i.e., for trace#1, significant effects from the bulk-substrate alloy microstructure are discernible in the rapid solidification (RS) microstructure (Figure 24a). At the onset of solidification seeded growth from the eutectic and the primary α-Al dendrites of the as-cast alloy substrate results in morphologically distinct features within the RS microstructure. The compositional mixing in the liquid alloy adjacent to the solid α-Al dendrites was incomplete prior to solidification which results in signatures in the RS microstructure that are complex and deviate from microstructural morphologies expected for directional RS growth normal to the thermal field contours (isotherms). The region affected by constitutional effects stemming from the compositional differences of the microconstituents of the as-cast substrate microstructure extends essentially across the entire RS microstructure established from the melt pool generated by two consecutive laser scans at speed of 2m/s (trace#1, Figure 24a). These undesirable effects from incomplete compositional mixing and lack of homogenization in the melt are minimized in the RS microstructures resulting after six scan passes at 2m/s scan speed (trace#3, Figure 24c). For trace#3 the region affected by the compositional variations of the microconstituents in the as-cast alloy

substrate and a lack of mixing in the melt affect only a narrow band extending at most 22μm from the substrate into the RS microstructure (Figure 24). The RS microstructures of trace#2 and trace#3 are comprised mostly of regions that have formed by directional α-cellular solidification. The α-cells are comprised of a matrix of supersaturated α-Al(Cu) solid solution and intracellular Al_2Cu phase that form by coupled growth with a morphologically cellular solid-liquid interface [3]. This type of microstructure forms in Al-10Cu alloys for solid-liquid interface velocity in the range of $\approx 0.3\text{m/s} \leq v_{SL} \leq 0.8\text{m/s}$ [3]. Small volumes of the RS microstructure of trace#2 and #3 also developed banded region morphology, which were more pronounced in trace#3 after a total of six scanned laser melting passes than in trace#2 after 4 laser melting events (Figure 24b, c). The absence of banded region in trace#1 and presence of increasing volumes of banded region in the RS microstructures of trace#2 and trace#3 indicates that the growth velocity (v) has reached critical values larger than 0.8m/s for the latter two and not for the former. RS after scanned laser remelting refines the scale of the microstructure relative to the as-cast state. The second laser scan pass melts the refined scale RS microstructure from the first scanned laser remelting pass, and so forth for consecutive scanned laser remelting passes. Also, compositional differences and variation are reduced to much smaller spatial length scale in the RS microstructure than in the as-cast microstructure. The reduced length scale for the composition variations reduces the time required for compositional mixing in the liquid state. Therefore, the RS microstructure shows the effects of the improved mixing and homogeneity achieved in the melt as the number of consecutive scan passes performed for scan speed of 2m/s increases. Local differences in the growth conditions at the migrating solid-liquid interface are reduced to smaller spatial length scales. This results in higher probability for the migrating solid-liquid interface to reach higher and even critical growth velocity over larger fractions of the migrating interface sections and to transition from the coupled

two-phase growth regime to the single-phase growth at the onset of banded region formation [43]. For the more scale refined RS microstructures larger fractions of the melt pool can reach these higher growth rates with little affect from the coarse substrate microstructure Figure 24.

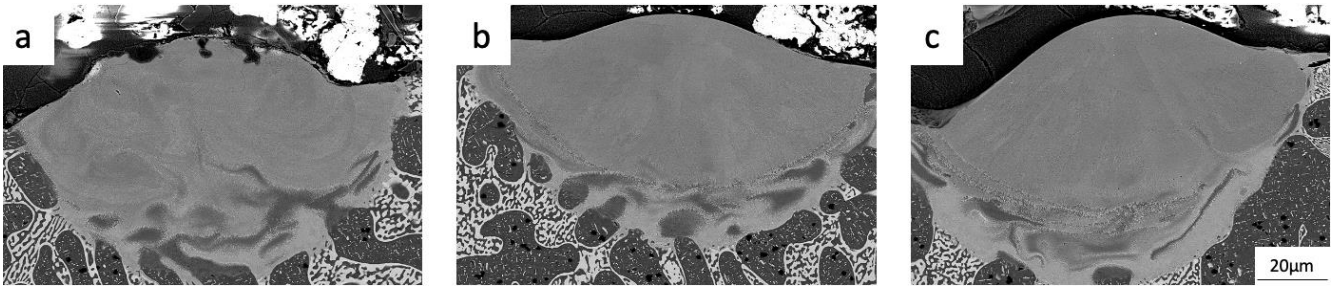

Figure 24. SEM micrographs presentign overviws of transverse cross sections for three RS microstructures and associated melt pools resulting from single trace laser scan melting with systematically varied scan speed for Trace#1, 1m/s, in (a), Trace#2, 2m/s, in (b) and Trace#3, 4m/s, in (c).

To reveal the RS microstructure growth relative to the isotherms in the melt pool formed by the scanned laser irradiation as the moving heat source investigation of the longitudinal cross sections, the (x-z)-plane in Figure 9d, is required. The montage micrograph of Figure 25 shows an example of the longitudinal cross section which was taken from near the center line of trace#3. In this montage figure the laser scanning direction is horizontal from left to right, which is equivalent to the x-axis in Figure 9d. Two morphologically distinct zones evolved as depicted in Figure 25. In zone 1, covering about the first 16µm of the rapid solidification microstructure forming from the as-cast alloy substrate as a solid seed, the morphology is highly affected by the inherent inhomogeneity of the composition in the liquid alloy that is inherited from the as cast microstructure. Insufficient melt flow dynamics and effects from Marangoni convection, where in this Al-Cu hypoeutectic alloy the solute is heavier and less mobile than the solvent, hindered complete mixing in the melt prior to solidification in the vicinity to the solid alloy substrate. For

example, in Figure 25 area (a) the α-Al solid solution dendrite has been melted and then resolidified rapidly before allowing for perfect composition mixing with adjacent Cu-richer neighboring regions, which have a lower alloy melting temperature. However, in area (b) marked in Figure 25 the eutectic microstructure has been significantly refined with lamellar wavelength of $\lambda \approx 20$ nm, while maintaining a lamellar morphology. Solidification of the latter alloy region can be suitably rationalized following the classic Jackson-Hunt model for a eutectic, which is applicable to small and moderate undercooling [44]. Establishing scale refined lamellar eutectic with 20nm wavelength implies local growth rate reaching about 0.2m/s (see section 4.2.2, Fig. 15). Zone 2 of the RS microstructure in Figure 25 was seeded from the strongly scale refined and morphologically homogeneous anomalous eutectic cells of α-Al matrix phase with mostly discontinuous Al_2Cu phase, which has been developed in the preceding scanned laser melting trace, and involved more controlled growth into a compositionally better homogenized alloy melt. Zone 2 of the solidification microstructure is located at larger distances from the solid alloy substrate than the microstructure observed in zone 1. Hence, zone 2 microstructure formed from alloy melt that remained liquid for longer durations and exhibited better composition mixing than zone 1 prior to re-solidification. As a result, the solidification microstructure of the alloy is less affected by the as-cast structure and is more homogeneous. The growth started with a cellular/dendritic growth mode for the primary α-Al and associated intercellular and/or interdendritic Cu-enriched and scale refined eutectic for about the first 2μm of the re-solidification microstructure (double dashed line in Figure 25). As the solidification interface accelerated during the directional solidification, morphologically modified or anomalous eutectic cell growth with α-Al matrix phase and increasingly discontinuous Al_2Cu phase of refined scale as secondary phase developed. These latter columnar growth regions dominate most of the zone 2 solidification microstructure. These

two-phase columnar grains or cells are characteristic of rapid solidification microstructures in Al-Cu alloys and have been referred to in the literature as α-cells, which form in Al-11Cu hypoeutectic alloy for solidification rates between ≈0.3m/s to 0.8m/s [16].

The longitudinal cross section view of the RS microstructure confirmed that the large scale of the compositional variations of the microconstituents of the as-cast alloy microstructure reduces the homogeneity. It also revealed the effectiveness of multi scan passes to enhance the composition mixing prior to RS. However, the complicated nano-scale RS microstructure developing due to the high growth rates greater than 0.1m/s prevent the reliable distinction between individual columnar morphology grains that develop across the melt pool during RS as the local solidification rate increases nominally from the bottom to the top of the longitudinal cross-section (Figure 25). This contrasts starkly with clear distinguishable changes in local growth direction of the a-Al cells for the low growth velocity regime with maximum growth reaching $\approx 2.7 \times 10^{-3}$ m/s explored for the low scan speed surface remelting, section 4.2, Figure 12b. In the low growth velocity regime, the changes in the cell growth direction clearly followed the thermal field gradients in the melt pool enabling a reliable determination of the velocity field across the longitudinal cross-section of the RS microstructure. The angle between cell growth direction and the laser scan direction changed from ≈90°to 23° across the depth z of the melt pool. In the low solidification rate regime, the evolving velocity field is stretched out over the depth dimension of the melt pool and relatively small changes in growth velocity occurred over relatively large distance in the RS microstructure. The effects of the local solidification rate changes are resolvable in the microstructure. This is not the case for the RS microstructures develop in the shallower depth melt pools obtaining for the higher laser scan velocity of 2m/s and 4m/s, respectively. very steep and difficult to be noticed

Considering application of equation (4-2) to estimate the changes in the local growth direction with the changes in local solidification rate for these large scan speeds shows that the angle θ between the nominal growth direction for the cell tips and the laser scanning direction for V_L= 2m/s ranges between ≈ 88° > θ > 66° for the RS microstructural regions observed in Figure 25. This represents a much smaller change in growth direction across the depth of the melt pool during RS, which therefore would be more difficult to detect than in the case of the low solidification rate regime. Furthermore, any slight inclination during longitudinal cross section preparation relative to the actual centerline plane of the laser trace (e.g., dashed line markers in the schematic of Figure 9d) decreases the accuracy of angle measurement. The finer scale of the RS microstructure additionally complicates attempts for tracing and detection of individual cells growing across the depth of the melt pool. Hence, unlike in the case of the lower solidification rate regime, for the higher solidification rate regime inspection and analysis of the RS microstructures in the longitudinal cross section view are not instructive.

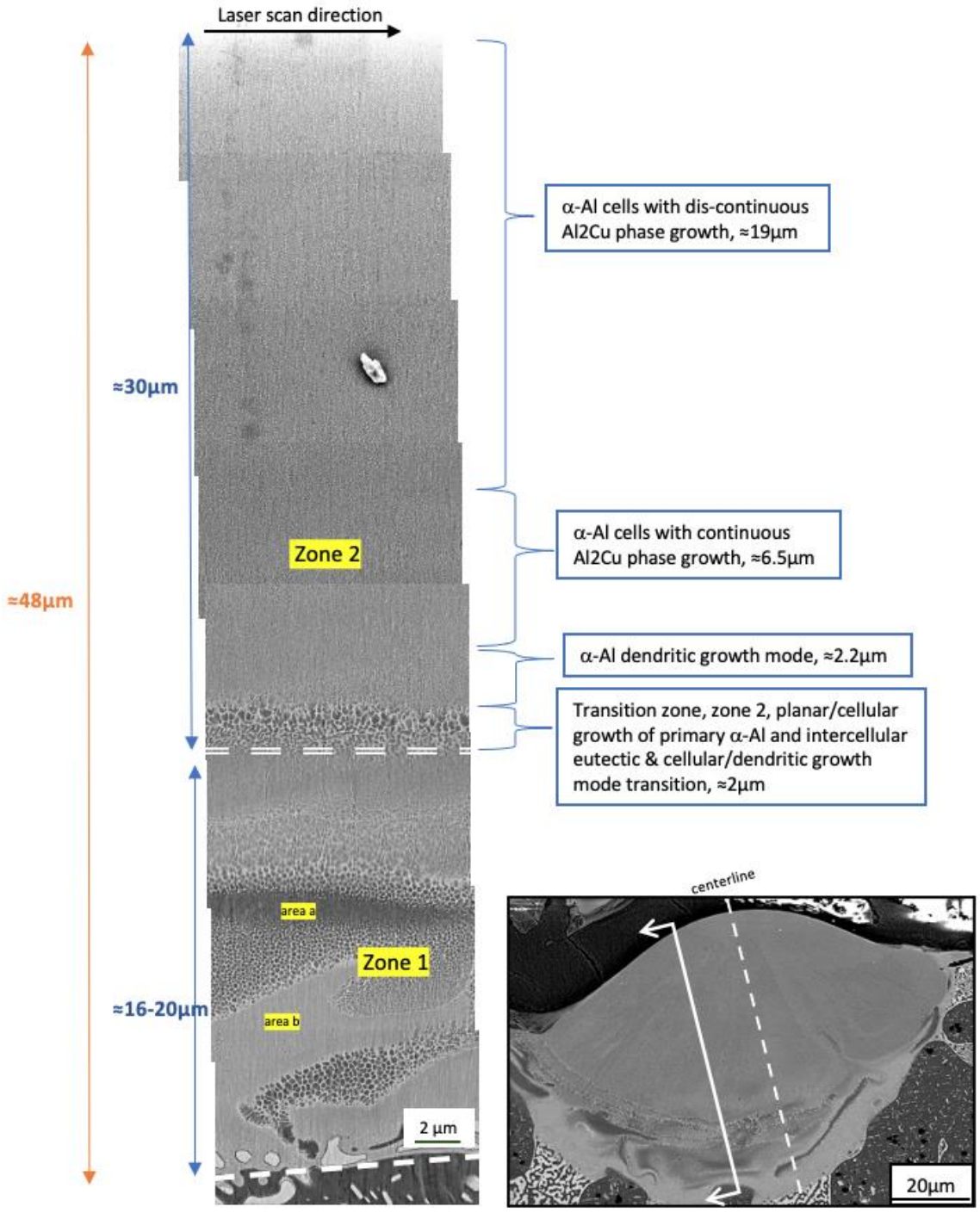

Figure 25: Montage of SEM micrographs of the longitudinal cross section of RS microstructure for single laser trace performed with 4m/s scan speed showing the microstructure evolution and morphology transitions from bottom to top as solidificaiton rate increases. The scanned laser passed across the horizontal dimensions of the field of view, 12µm, within 3µs=3x10^{-6}s.

4.4.2 Effect of Multi-Pass Scanned Laser Surface Remelting at Two Different Scan Speeds on the RS Microstructure

The microstructures of the laser traces#4 to #9 were developed by overlapping laser scan passes that employ different scan speeds while keeping power and spot size of the laser constant. First a large melt pool is created at 1m/s scan speed followed by creation of smaller melt pools in subsequent scans at higher scan speed. The higher scan speed for the smaller melt pool creations was 2m/s for traces #4, #6 and #8 (for brevity set#1 hereon, Table 6) and 4m/s for traces #5, #7 and #9 (for brevity set#2 hereon, Table 6), respectively. The transverse cross sections show two distinct concentric melt pool boundaries (marked as dashed line in Figure 26 a). The large melt pools are featuring keyhole defect geometry and had dimension averages of about 186±10μm in depth and 232±13μm in width for traces #4 to # 7, respectively (Table 6). The dimensions of traces #8 and #9 differ from those of traces#4 to #7 (Table 6), being 125±5μm deep and 200±5 for trace#8 and 60±5μm deep and 155±5μm wide for trace#9, respectively. Since nominally the same scan speed, laser power and spot size have been used for creation of the large melt pools this difference in dimensions is unexpected. The significant changes in dimensions for the large melt pools for traces#8 and #9 relative to those of traces #4 to #7 has been attributed to artifacts from technical issues experienced with the EOS SLM instrument operation during these latter surface remelting experiments. The regions that experienced a lack of compositional mixing in the liquid alloy prior to solidification extend approximately up to 50±10μm into the RS microstructure in the central region near the bottom of the resolidified regions where convection loops can be seen (Table 6, Figure 26 a-f). Increasing the number of repeated scanned remelting events for the creation of the large melt pools by increasing the number of consecutive laser scans from 3 scans (trace #4 and

#6) to 6 scans (traces #5 and #7) (see Table 5) reduced the lack of compositional mixing zone by on average 10 μm (Table 6). The RS microstructure established from the large melt pools consists primarily of columnar morphology grains with a modified eutectic cell structure.

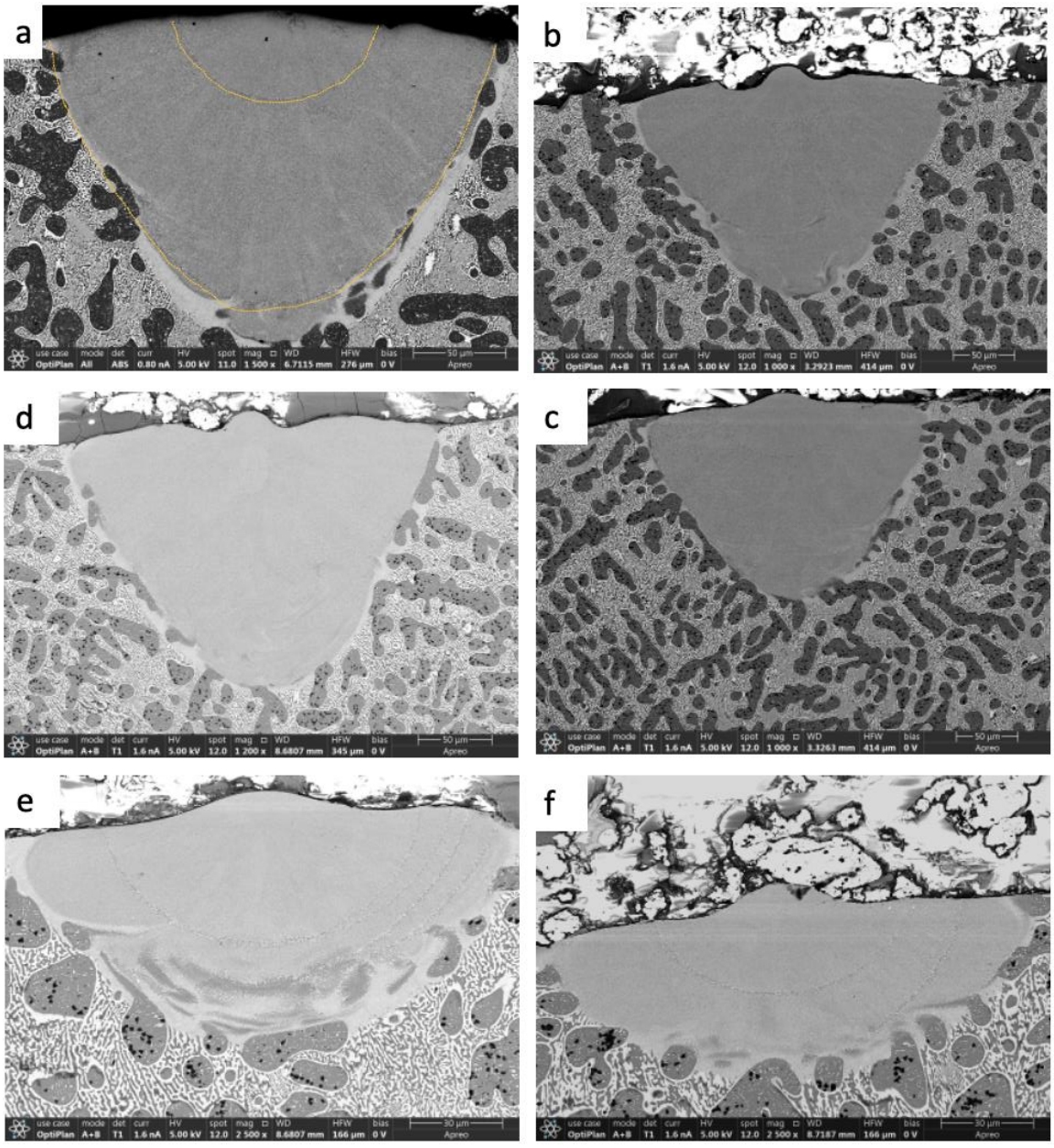

Figure 26 SEM micrograph of transverse cross section for the RS microstructures evolved for six systematically varied laser scanning schema (see Table 6) from the melt pools of Trace#4 in (a), Trace#5 in (b), Trace#6 in (c), Trace#7in (d), Trace#8 in (e), and Trace#9 in (f)

Table 6 Large melt pool created at 1m/s detailed measurments

Trace #	Large meltpool		Lack of compositional mixing at melt pool boundry (μm)
	Depth (μm)	width (μm)	
Trace 4	176±8	236±6	up to 53 μm at large melt pool
Trace 5	190±10	253±10	up to 40 μm at large melt pool
Trace 6	180±6	225±6	up to 60 μm at large melt pool
Trace 7	200±8	250±8	up to 54 μm at large melt pool
Trace 8	125±5	200±5	up to 42 μm at large melt pool
Trace 9	60±5	155±5	up to 42 μm at large melt pool

The refined scale of RS microstructure with the columnar α-cells established by the 1m/s scan speed re-melting in the larger melt pools acted as the solid substrate for seeded growth during RS for the smaller melt pools resulting from the subsequent re-melting at the higher laser scan speeds of 2m/s and 4m/s. The fine scale of the substrate microstructure reduced the length scale for compositional and morphological differences in the solid adjacent to the liquid at the RS growth interface. Thus, at an approximately micrometer length scale on average self-similar thermal and constitutional conditions at the solidification interface developed. The small melt pools of the scanned laser surface remelting of the traces of set#1 (traces#4, #6, #8) have been obtained for 2m/s scan speed and had average dimensions of 50±2μm in depth and 102±3 in width. The small melt pools of the scanned laser surface remelting of the of set#2 (traces#5, #7, #9), which were created at 4m/s, had on average depth of 38±3μm and width of 92±8μm. The increase in laser scan speed from 2m/s to 4m/s reduced by about 24% and 10% the depth and width dimensions of the melt pool. These dimensions are very close to the melt pool dimensions attained for scanned laser surface remelting using a single laser scan at 2m/s and 4m/s reported in section 4.3, Table 4. Therefore, it can be concluded that the power imparted to the Al-10Cu alloy during surface

remelting by the scanned laser irradiation for creation of the smaller melt pools is not affected significantly by the modification of the microstructure in the irradiated trace resulting from application of the initial scans at the lower laser scan speed that created the larger melt pools.

The seeded growth from the refined scale microstructure substrate established in the larger melt pool yielded characteristic RS microstructure morphologies in the small melt pools obtained for the fast laser scan velocities of 2m/s (set#1, Table 7) and 4m/s (set#2, Table 7) equivalent to those observed in pulsed laser induced RS experiments of nanoscale thickness alloy thin films of hypoeutectic Al-Cu alloys with a nanoscale polycrystalline substrate [3], [9], [14]. The growth modes of the solid-liquid interface transition from initially planar to cellular, then to dendritic, back to cellular and then finally again to planar as the interface velocity increases from the initially stationary state with zero velocity [3], [14], see section 2.3. The morphological changes associated with these growth mode transitions can be observed in the RS microstructures of hypoeutectic Al-Cu alloys as typically four morphologically distinct zones: 1) A heat affected zone (HAZ) where only partial melting occurred, 2) an initial transition zone comprised of primary α-Al grains and Al2Cu phase containing secondary solidification product, 3) a columnar grain zone established by cellular growth of modified eutectic cells, and 4) banded region grains [3]. These morphologically distinct zones can also be identified for the RS microstructures of the small melt pools obtained for 2m/s scan speed (set#1, traces #4, #6, #8) and 4m/s scan speed (set#2, traces #5, #7 and #9) for the bulk Al-10Cu alloy studied here. For set#1 of the small melt pools the first morphological changes in the RS microstructure are associated with the planar/cellular transition of the solidification interface and have been observed to occur after the first $\approx 0.5\pm0.1\mu m$ of crystal growth (see marker in Figure 27). Subsequent RS microstructure morphology changes are observed after an additional $\approx 0.25\pm0.05\mu m$ of crystal growth, which are attributed to the cellular/

dendritic transition. The initial about ≈1μm of the RS microstructure of the set#1 small melt pools is equivalent to the transition zone or zone 2 of the distinct microstructural zones reported for hypoeutectic Al-Cu alloys in prior studies of pulsed laser induced RS in thin films [3]. A columnar grain morphology with columnar α-cells comprising continuous θ-Al_2Cu phase presents for up to ≈ 8±3μm in the RS microstructure (Figure 27). This is followed by columnar α-cells with discontinuously distributed (θ/θ')-Al_2Cu phase for typical growth distances of ≈ 25±6μm up into the melt pools (Figure 27).The columnar grain morphology region is equivalent to the zone 3 microstructure reported in prior research of Al-Cu thin film RS microstructure evolution [3]. The very upper regions of the RS microstructure of the different set#2 melt pools show banded regions with total area ranging from 133 μm^2 to 227 μm^2 (Figure 26, Figure 27). For the small melt pools of set#2 qualitatively the same morphologically distinct regions as for the set#1 RS microstructures have been observed. Namely, first a transition zone, where the initially planar and subsequent cellular-dendritic growth transition to cellular growth of the two-phase α-cells in the second zone of columnar grains and finally banded grain regions. The planer/cellular transition has been observed after 0.4±0.05μm, followed by transition to cellular/dendritic growth over an additional ≈ 0.3±0.05μm (e.g. Figure 27).The columnar α-cells with continuous θ-Al_2Cu phase changed after ≈ 3±2μm to columnar α-cell with discontinuous (θ/θ')-Al_2Cu phase, which grew for ≈ 18±10μm prior to formation of banded region area of ≈ 140, ≈ 170 and ≈ 700 μm^2 for traces#5, #7 and #9, respectively. Measurements of the dimensions associated with these morphologically distinct microstructure zones, the transition zone, which includes the planar/cellular and the cellular/dendritic growth mode transitions, the columnar zone, which includes the regions with continuous and discontinuous Al_2Cu phase in the α-cells, and the banded regions are collated in

Table 7. The growth mode transitions are accomplished at alloy composition dependent characteristic and critical values of the solid-liquid interface velocity [3].

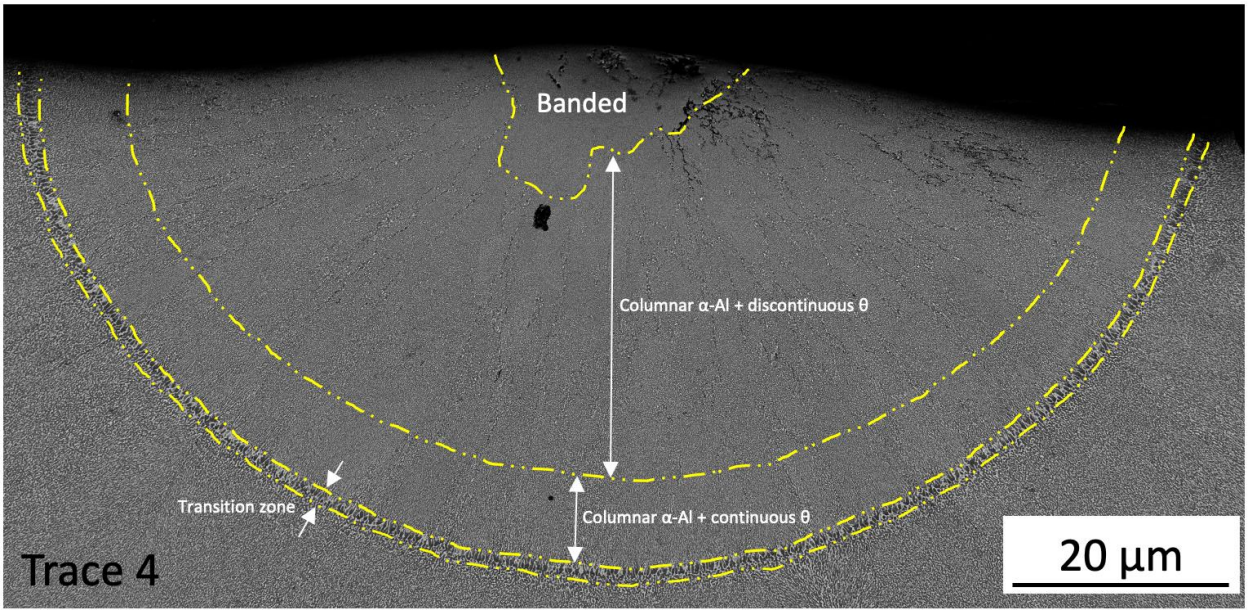

Figure 27 SEM BSE micrograph depiciting and overviwe of the RS microstructure developed for the Small melt pool created at 2m/s from the microstructure established in the larger melt pool attained for 1m/s laser scan speed.

Based on prior research the ranges of solid-liquid interface velocity, v, for the morphologically distinct RS microstructure regions in Al-11Cu alloy have been determined as $v < 0.25$m/s for the transition region with planar/cellular growth modes and transition to dendritic, followed by zone 3 morphology of the columnar grain regions ensuing as $v \approx 0.3$m/s [3]. The columnar morphology grains have been reported to grow for interface velocity in the range of $\approx 0.3\text{m/s} \leq v \leq \approx 0.8\text{m/s}$, with α-cells with continuous θ-Al_2Cu for $0.3\text{m/s} \leq v \leq 0.55\text{m/s}$, and then with discontinuous (θ/θ')-Al_2Cu for $0.55\text{m/s} \leq v \leq 0.8\text{m/s}$, followed finally by and banded region

for $v \geq v_a \approx 0.8$m/s [3]. Using the growth rates reported in prior research on hypoeutectic Al-11Cu alloy RS and the laser scan speed for each of the laser traces in set#1, created at 2m/s, and set#2, created at 4m/s, the ranges of the angles for the growth direction, θ, perpendicular to the isotherms in the melt pool behind the moving laser beam spot can be calculated using equation (4-2), $v=v_{scan}\cos\theta$, and are also shown in Table 7. The values for the angle, θ, between the growth direction and the scan direction of the scanned laser beam are large, falling in the range of $\approx 66^{\circ} \leq \theta \leq \approx 86^{\circ}$. Most of the RS microstructure observed in the transverse cross section views, i.e., with exception of the banded region, has approximately grown in the plane of the micrograph, i.e., from the bottom to the top of the melt pool when considering the centerline of the melt pools (Figure 26). The cellular growth of the two-phase α-cells of the columnar grain regions does not change growth direction (angle) dramatically as was observed in the RS microstructures obtained for surface remelting with the much smaller laser scanning speed of 0.003m/s discussed in section 4.2 (e.g., Figure 12). This has also been shown by characterization of the longitudinal cross section Figure 25.

The laser surface remelting scheme of using two different scan speeds, first a smaller scan speed to create a larger region of refined scale RS microstructure and then secondly larger scan speeds to create smaller regions of melt surrounded by solid RS microstructure, enabled the formation of RS microstructures in the Al-10Cu alloy that can be interpreted to good approximation by the assumption of directional crystal growth along the thermal gradients in the melt pool. At a length scale of about 1μm segments of the solidification interface experienced on average identical conditions during the RS microstructure formation due to the refined scale of the growth seeding solid substrate microstructure and the good compositional mixing in the liquid of the melt pool. This enables correlation with prior studies on geometrically controlled directional

RS in nanoscale thickness thin film alloys, which provided experimental measurements of the local solidification interface velocity during formation the multiphase RS microstructure with its characteristic morphologically distinct regions (e.g. Figure 8). The multi-pass scanned laser surface remelting with the multiple scan speeds provides larger scale bulk forms of RS microstructures equivalent to those observed by in-situ TEM in nanoscale thin films and, therefore, can facilitate experimental research to determine the mechanical properties of these non-equilibrium transformation products in the Al-Cu alloys.

Table 7 RS microstructure metrics for the regions in the small melt pools and calculated growth angle, q, between direction of average local soldification rate, $V=V_{SL}$, and the direction of the laser scan velocity, V_L, based on the location specific morphology.

Trace #		small meltpool		Morphology changes lengths at smallest melt pool from bottom of melt pool (μm), z									
				planer/cellular		cellular/dendritic		columnar cell w/ cont. θ		columnar cell w/ dis. cont. θ		Banded	
		Depth (μm)	width (μm)	v = 0.25 m/s		v = 0.3 m/s		0.3 < v < 0.55		0.55 < v < 0.8		v > 0.8 m/s	
				z	growth angle θ	z	growth angle θ	z	growth angle θ	z	growth angle θ	z	growth angle θ
set#1	Trace 4	48	105	0.6		0.3		11±1		22±5		190	
	Trace 8	50	102	0.4	82.8	0.3	81.4	6±1	81.4 > θ > 74.0	23±2	74.0 > θ > 66.4	227	θ < 66.4
	Trace 6	52	100	0.4		0.2		8±3		31±1		113	
set#2	Trace 9	35	85	0.3		0.3		1±1		9±2		700	
	Trace 5	40	100	0.45	86.4	0.3	85.7	4±1	85.7 > θ > 82.1	25±4	82.1 > θ > 78.5	140	θ < 78.5
	Trace 7	40	90	0.4		0.3		3±1		19±2		85 / 170	

4.5 Mechanical Properties Variation as Function of Microstructure Morphology

It is impossible to successfully study the hardness contributions of the morphologically distinct regions and the characteristic non-equilibrium features developing across the rapid solidification microstructure of Al-10Cu hypoeutectic alloy for laser scan speeds larger than 1m/s by conventional microhardness testing due to the refined microstructure scale. Thus, in analogy to the mechanical testing experimentation performed for the low scanning speed laser surface

remelting related solidification microstructures (section 4.2), spatially resolved mechanical property measurements have been performed for the morphologically distinct regions that formed in the rapid solidification microstructures by a combination of instrumented nanoindentation and SEM imaging. A goal of this experimentation is the study of relationships between the local solidification conditions, e.g., solidification interface velocity, the distinct and characteristic microstructure morphology and scale, and the associated mechanical properties. Here, the nanoindentation measurements of the RS microstructure were classified based on the solidification growth rate. The nanoindentation measurements were conducted on the transverse cross sections then only the indent represents the morphology accurately will be considered.

Typical load-displacement curves for the RS microstructure in the as cast α-Al and across different regions of the RS microstructure established from the melt pools are compared in Figure 28. The unloading curves did not trace the loading curves for all indents, e.g., see Figure 28. This suggests that the indented phase exhibited ductility and plastic deformation occurred. For the load-displacement curves discontinuity have been observed which are called pop-ins. The pop-in phenomenon has been reported in studies of nanoindentation in Al alloys and is associated with dislocation nucleation and mobility [47]. Multiple nanoindentation arrays have been performed for the as-cast and the RS microstructures of the Al-10Cu samples used in the scanned laser surface remelting in the high scan speed regimes of 1m/s to 4m/s. The hardness value of as-cast α-Al solid solution dendrites has been found to be H=1.03±0.05GPa, consistent with literatures data [80], [81] and the nanoindentation experiments performed at the smaller laser scan speeds (sections 4.2, 4.3). The increased in hardness of the α-Al solid solution dendrites compared to pure Al (H = 0.7 GPa [55]) stems from the substitutional Cu solute atoms, which interact with the mobile dislocations via solute strengthening [64]. For the RS microstructure of the Al-10Cu alloy

established for the laser scans with scan speed 1m/s to 4m/s, the hardness values increased significantly. In the fine eutectic morphology resolidified region, the hardness (H) values have been determined to be in the range of 4.1 GPa ≤ H ≤ 4.6 GPa, with hardness depending on the lamellar wavelength, λ. Based on results reported for lamellar eutectics in Al-Cu these hardness values are consistent with the empirical relationship to the lamellar wavelength and imply λ in the range of 70nm to 85nm [15]. Lamellar eutectic with refined scale on the order of 70-85nm would be expected to form for local solidification rates of about 0.01m/s=1cm/s to 0.02m/s=2cm/s.

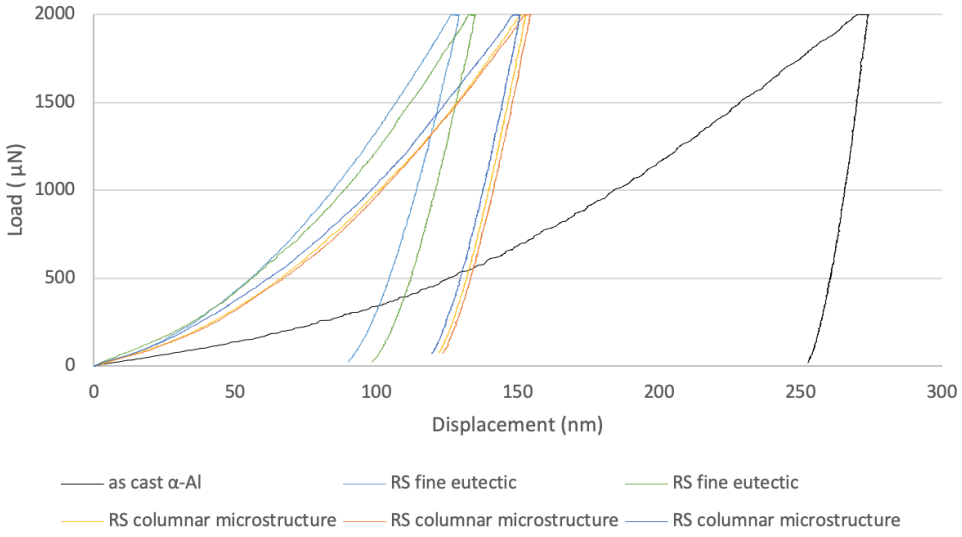

Figure 28 Typical load–displacement curves for α-Al phase of the as-cast and the RS microstructure.

To determine the mechanical properties of the different characteristic RS morphology regions the indents should plasticly deform each morphology alone without any interference from neighboring different morphology or grain boundaries. The relatively small area of high solidification rate morphologies and the low magnification of the optical microscope in the nanoindentation instrument reduce the success rate for the indents to encounter the specific area of interest. However, the fact that each indent is representative of the deformed area that has been

probed it is possible to capture a few successful experiments, which then represent an accurate representation of each morphology. Thus, a relatively small number of on the order of five successful indentation experiments have been considered here to be adequate to reveal the hardness of that specific microstructure morphology. Multiple indents were performed on the small melt pools of the traces#4 to #9 to assess the mechanical properties for the morphologically distinct regions in the RS microstructures of the Al-10Cu alloy. The hardness measurement variations in the melt pool ranged from H= 2.7 to 4.7GPa, see Figure 29 a. This represents hardness increases of about 258% to 571% compared to the pure Al and 145% to 327% compared to the as-cast α-Al(Cu) solid solution. The hardness values measured for the different regions of the Al-10Cu RS microstructure are similar to hardness of lamellar Al-Cu eutectic [15]. For instance, a hardness value of 4.25GPa encountered in the region of Banded morphology grains is equal to hardness of lamellar Al-Cu eutectic with inter-lamellar spacing of ≈80nm [15].

Indents at the perimeter of the small melt pool encounter mostly α-Al cell/dendrite and θ-phase in the transition zone (Figure 27). The hardness (H) ranged from 2.7GPa when a relatively large α cell is probed (see Figure 29b) to 4.7GPa when the indent encountered large intercellular θ-phase during deformation. Several indents located deeper in the interior of the melt pool probed the RS microstructure region associated with the columnar cells with continuous θ-phase. Here the H measurements ranged from ≈ 3GPa to 3.68GPa (e.g., see the two circles annotated in Figure 29a and Figure 29c as enlarged image). For this RS microstructure region, the differences in H values were mainly due to the characteristic spatial distribution, the wavelength (λ), of the wavey continuous θ-phase, which showed lowest H at λ≈230nm and highest at λ≈150. These values are quite similar to the hardness that would be predicted for the regular lamella eutectic with equivalent spacings of 230nm with H= 3.0GPa GPa and 150nm with H= 3.4GPa, respectively [15]. The

columnar grain regions with discontinuous θ' showed a smaller H values and a smaller range of H values than the former morphology, i.e., $2.76 \leq H \leq 3.2$GPa (see arrows in Figure 29a). The alternating layers of single-phase Al(Cu) solid solution and two-phase with Al(Cu) and discontinuous θ/ θ' in the banded region have significant effect on the divergence of H values; $2.8\text{GPa} \leq H \leq 3.6\text{GPa}$. The highest H values for the banded region are measured when the indent completely measures a two-phase band (Figure 29d) and lowest value results when most of the indent is located in the single-phase α-Al(Cu) bands (Figure 29e). No indent was successfully performed to measure only a single-phase band because the single-band width was fixed and too small, unlike the two-phase band width, which starts with large width and decreases as growth rate increases. Table 8 summarize the hardness measurements as averages determined by the nanoindentation experiments performed for the RS microstructures evolved in the small melt pools of traces#4 to #9 for the distinct RS microstructure morphologies.

The mean values of the hardness for the columnar morphology grains with continuous θ, columnar morphology grains with discontinuous θ, and for the banded morphology grains distinguishing between the two-phase bands and the combination of two-phase and single-phase bands, were tested using the two-means t-test to verify their statistical significance. The computer software Minitab [Minitab® Statistical Software, Web App, accessed May/ Jun 2022] has been used for these numerical assessments of the experimentally measured data sets. The null hypothesis used in the test is H_o: $\mu_1 = \mu_2$ a, and the alternative hypothesis is H_1: $\mu_1 \neq \mu_2$. Here, μ_1 and μ_2 are values of the means that are compared by the t-test. The significance level was set to α=0.05. Based on the p values, i.e., the probability values calculated via t-test, the null hypothesis was rejected in the case of columnar morphology grains with continuous θ and columnar

morphology grains with discontinuous θ. This confirms that the mean hardness values of these two morphologically distinct RS microstructure regions are different within a 95% confidence interval. Also, the t-test analysis rejected the null hypothesis for the hardness values measured for the single-phase bands and with combined two-phase and single-phase bands. Table 9 summarize the two-means t-test results for the four morphologically different regions of the RS microstructure of the Al-10Cu alloy.

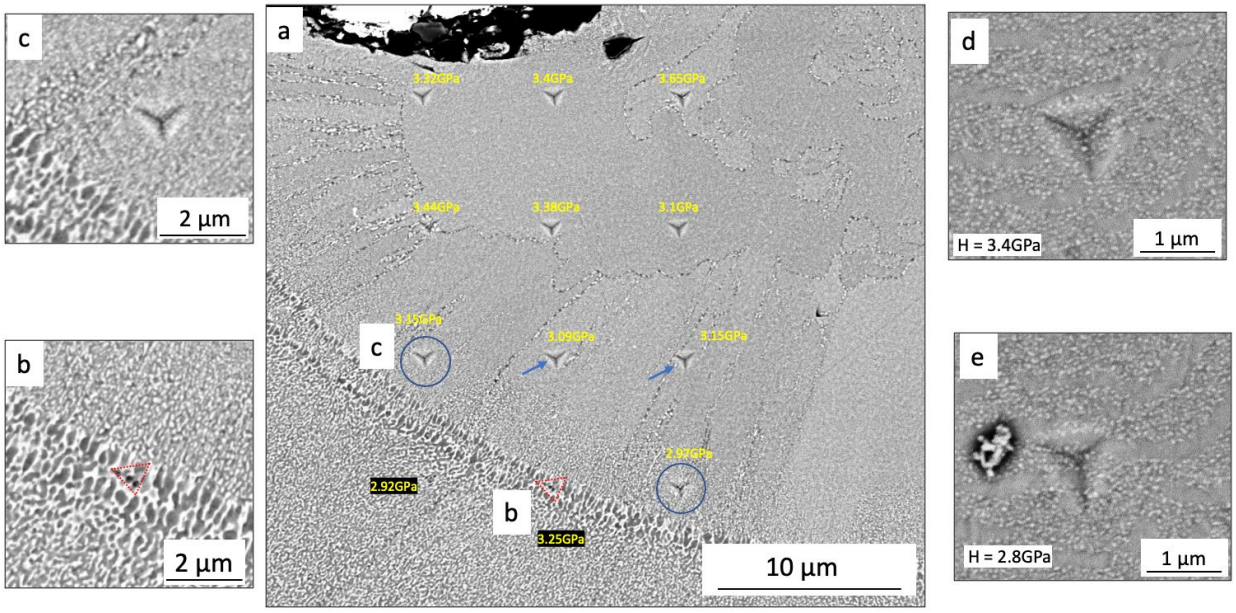

Figure 29 a) SEM BSE micrograph example of nanoindentation array performed on the RS microstructure established in melt pool created at 4m/s scan speed with the H values of the indent marked, b) and c) enlarged images of some example indents shown in a), d) and e) enlarged images of indents from different melt pool at banded region.

Table 8 Average hardness measurments at different solidification growth velocity

	Growth rate (m/s)	V < 0.3	0.3< V <0.55	0.55< V <0.8	V > 0.8	
Morphology	RS regular eutectic	planer => cellular => dendritic	columnar cells w/ cont. Θ	columnar cells w/ discont. Θ	Banded (two phase band)	Banded (both bands)
Hardness (GPa)	4.35	2.28	3.32	2.98	3.35	2.95
Standard deviation	0.35	0.20	0.16	0.14	0.24	0.23

Table 9 Comparison of two-means T-test results for four distinct RS morphologies (also see Appendix A for more detail)

	columnar cells w/ cont. Θ	columnar cells w/ discont. Θ	Banded (two phase band)
columnar cells w/ cont. Θ			
columnar cells w/ discont. Θ	$\mu1 \neq \mu2$		
Banded (two phase band)	$\mu1 = \mu2$	$\mu1 \neq \mu2$	
Banded (both bands)	$\mu1 \neq \mu2$	$\mu1 = \mu2$	$\mu1 \neq \mu2$

The hardness in the cellular eutectic region of the α-cells with continuous θ-phase, average H=3.32 GPa, and with discontinuous θ/θ'-phase, H=2.98GPa, are significantly smaller than maximum harnesses measured for the fine scale lamellar eutectic regions, H=4.35GPa (Table 8). This can be attributed to the more refined scale of the composite like microstructure of the lamellar eutectic regions with α-Al lamellae of width below 100nm when compared to the columnar morphology grains of the two-phase α-cells in the RS microstructures. The slip distances for dislocations between the Al_2Cu intermetallic phase obstacles are larger in the α-Al phase for the α-cells of the columnar morphology regions of the RS microstructure than in the fine scale lamellar eutectic with $\lambda \approx$ 80nm. The average width of α-Al phase separated by the continuous Al_2Cu intermetallic phase in the columnar morphology region, which extends about 3μm into the RS microstructure form the transition region (see Figure 29), has been determined to be in the range of 150nm to 260nm using a line intercept analysis of select regions (e.g., see enlarged insets shown in Figure 29). For the region with the discontinuously dispersed Al_2Cu intermetallics dislocations

can bow out between these glide obstacles, which would be expected to result in a reduction of the hardness compared to the composite-like morphology with continuous hard obstacles of wavy or regular lamellar eutectic morphology. Furthermore, the discontinuously dispersed Al_2Cu intermetallics in the α-cells have been shown to be θ'-phase with non-equilibrium spheroidal rather than plate shape. Unlike the θ-Al_2Cu, which is the equilibrium phase and incoherent with the α-Al lattice, the θ'-phase forms coherent interface sections with α-Al phase. When θ'-phase precipitates form during low temperature aging of supersaturated Al(Cu) solid solutions via a solid state transformation plate shapes with small incoherent interface sections perpendicular to the large coherent interface section parallel to the basal planes with an orientation relationship of (001)θ' || (001)α are preferred to minimize effects from strain and interfacial energy. The discontinuous θ'-phase with spheroidal shape might act as a weaker type of obstacle for dislocation glide than the completely incoherent θ-phase that requires bowing via the Orowan mechanism, since shearing/cutting might be possible for the coherent interface segments.

As the solidification velocity increases during RS the amount of solute trapped in the α-Al(Cu) phase is expected to increase well beyond equilibrium solid solubility. Also, for the regions of RS microstructure formed by coupled two-phase growth the secondary Al_2Cu phase would be expected to decrease in size while presenting with increasing the number density. Since the scale of the α-Al and Al_2Cu phases are the coarsest and α-Al(Cu) exhibits the least amount of Cu solute trapping, the RS microstructures formed at the melt pool perimeter shows the smallest hardness of 2.7GPa. This value increased by up to 21% in the columnar α-cell with discontinuous θ/θ'-particles. The variation of hardness in the discontinuous θ/θ' zone of the RS microstructure results from differences in the size and density of the second phase Al_2Cu intermetallics encountered

during the respective indentation experiments. However, the experimentally measured hardness value variation in the banded region of the RS microstructure originates from the alternation of layers of α-Al(Cu) single phase solid solution and two phase α-Al/Al_2Cu bands. Most of the time the indents encounter both layers and showed the smallest hardness value when plasticly deformed volume captured the α-Al(Cu) layer. The highest hardness in the banded regions of 3.6GPa was observed when the indent fully deformed only a two-phase band.

4.6 Effect of Isothermal Annealing of the Rapid Solidification Microstructure

The RS microstructure established in hypoeutectic Al-10Cu after scanned laser surface melting with scan speeds of 2m/s to 4m/s consists of metastable supersaturated α-Al solution, nano-meter scale refined θ-Al_2Cu and metastable nano-scale spheroidal shape θ'-Al_2Cu. The RS microstructure of the Al-10Cu alloy represent a non-equilibrium state which can undergo additional transformations. Post-solidification annealing heat treatment can provide the thermal activation required to initiate diffusion facilitated evolution of the non-equilibrium RS microstructure of the Al-10Cu alloy. The full precipitation sequence for the thermally activated transformations of supersaturated α-Al(Cu) solid solution can involve formation of the metastable GP zones, θ''-phase, θ'-phase and finally the thermodynamically stable θ-phase (see e.g., Fig. 2 and Fig. 3). Since nanoscale refined θ'-phase and θ-phase already exist in most of the morphologically distinct regions of the RS microstructure of the Al-10Cu alloy, these phases would be expected to coarsen during aging treatment to reduce the Cu solute concentration in the surrounding supersaturated Al(Cu) solid solution. Nucleation and growth of GP zones would have to compete with these coarsening processes of the thermodynamically more stable phases. In regions of the RS microstructure that are free of precipitates, e.g., the single phase bands of the banded regions and some of the larger nearly micron-scale α-Al(Cu) cells formed the early stage of RS in the transition zone along the perimeter of the melt pool nucleation and growth of the coherent GP zones and θ''-phase, which have lower nucleation barriers than the partially coherent θ'-phase and the incoherent θ-phase, would appear feasible under the appropriate annealing conditions. The transformation of θ'-phase into θ-phase requires nucleation of the latter. This can be achieved via heterogeneous nucleation more effectively than by homogeneous nucleation. The

interfaces between grains of α-Al and the α-Al matrix and the discontinuously dispersed θ'-phase in the columnar grain region and the banded region are potent sites for heterogeneous nucleation of the stable θ-phase. More specifically, it can be envisaged that localized heterogeneous nucleation of θ-phase occurs at suitable surface steps of the θ'-phase interface with α-Al. Subsequently, local short-range diffusional rearrangements at the interface between θ-phase and the θ'-phase allows for rapid growth of the thermodynamically more stable θ-phase at the expense of the compositionally equivalent metastable θ'-phase. This thermally activated transformation process for θ-phase formation is facilitated and limited by local solid Cu diffusion, i.e., no long-range lattice diffusion through the α-Al lattice is required. Therefore, the transformation kinetics associated with aging of the non-equilibrium RS microstructure are expected to deviate and be more rapid than those established for aging of supersaturated α-Al(Cu) solid solution alloys with more dilute Cu content (e.g. Figure 3).

To derive an estimate for reasonable isothermal annealing condition to study aging behavior and associated mechanical property changes for the RS microstructures it is useful to calculate expected diffusion distances for some temperature ranges below the θ'-phase solvus (Figure 2). The approximate diffusion distance at different temperatures can be calculated as follow:

The diffusion coefficient (D) is given by

$$D(T) = D_o e^{\frac{-Q}{RT}} \quad \textbf{(4-9)}$$

and the diffusion distance (x) in three dimensions is given by

$$x = \sqrt{6Dt}$$

(4-10)

where, D_o is the temperature - independent preexponential for diffusion of Cu in fcc Al, D_o = 6.5x10^{-5} m^2/s, Q is the activation energy for Cu diffusion in fcc Al, Q= 1.36x10^5 J/mol, R = 8.314 J/mol-K is the gas constant, T is the absolute temperature (K) and t is diffusion time (s) [74]. Figure 30 shows the times required to achieve desired diffusion distances at several isotherms (180, 230, 250, 280^{o}C) for long-range lattice diffusion of Cu in fcc Al.

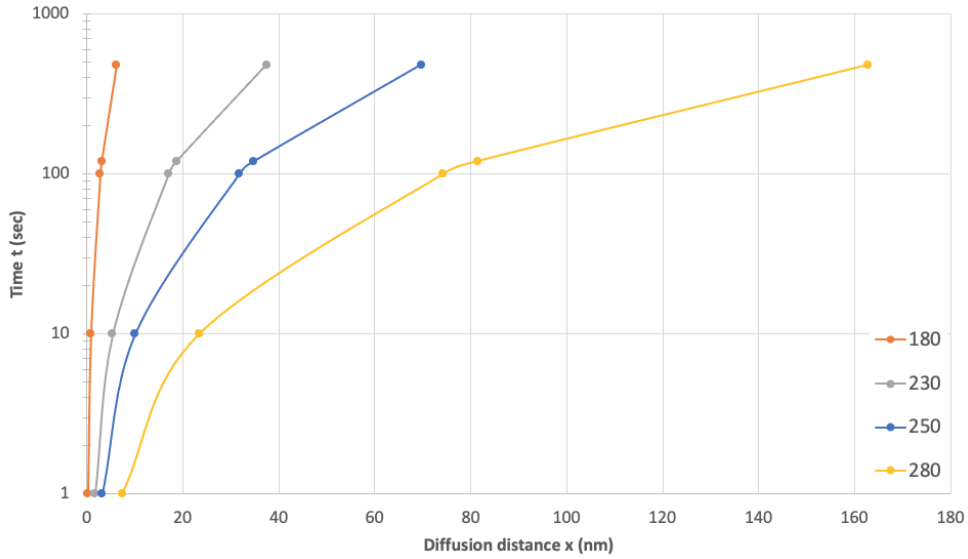

Figure 30 Predicted diffusion distance at isotherms 180, 230, 250 and 280^{o}C.

Experimentally it is difficult to control isothermal annealing holds for times shorter than about 1 minute=60s. Considering annealing times for isothermal holds of 120s duration Fig. 30 shows that diffusion distances on the order of 3nm for 180˚C and about 80nm for 280˚C would be reasonably expected. Hence, annealing times of 120 sec (2 minutes) and up to 480 sec (8 minutes) have been selected as the minimum and maximum annealing times. Based on the scale of the two-phase regions of the RS microstructure, e.g., discontinuously distributed θ'-phase with a spatial

separation of ≈150nm to 260nm, is expected that for annealing at 280˚C Cu diffusion from the supersaturated a-Al(Cu) crystal between the Al_2Cu related phases facilitates coarsening and transformation of latter. For a short annealing time fine scale incoherent θ-phase may be expected to form at high density and the semi-coherent θ'-phase may only partially dissolve, while for the increased annealing time of 8 minutes the θ-phase will continue coarsen and all of θ'-phase should be dissolved, while the Cu solute concentration in the α-Al lattice reaches equilibrium. This would represent a coarsened and thus overaged state. The aging induced changes in the alloy microstructure should affect the mechanical properties. Intermediate states of aging prior to reaching an overaged state with coarsened θ-phase in α-Al with equilibrium solute concentration can then be studied using lower annealing temperatures, e.g., 180 ºC to 230 ºC. This chapter will discuss the annealed microstructures (section 4.6.1) and its mechanical properties (4.6.2).

4.6.1 Microstructure of RS Changes After Annealing

The resultant microstructure after annealing process has unusual population and size of stable and metastable Al_2Cu phases. For example, Figure 31 shows the difference of metastable Al_2Cu phases before annealing, as RS state, (Figure 31a) and after 8 minutes of isothermal annealing at 280ºC (Figure 31b).

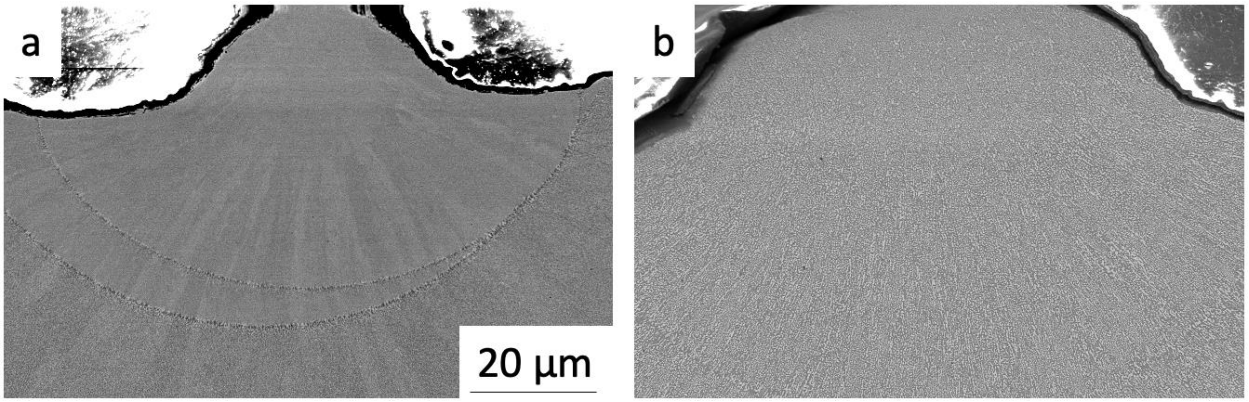

Figure 31 Overview SEM BSE comparing RS microstructure in a) with annealed state after 8 min at 280˚C. Both micrographs have the same scale marker.

From equation (4-10), the diffusion distance of 100nm can be reached at 280ºC annealing for about 170 seconds, while after 120s a diffusion distance of about 80nm is predicted. However, at this much higher solute content, the apparent diffusion coefficient must be sufficient to achieve in 120 seconds copper transport over the distances around 100nm between the individuals Al_2Cu phases distributed in the RS microstructure before annealing. During annealing, there was nucleation and growth of second phase particle across the melt pool. For example, in the single-phase band where we still can recognize the partitionless region after 120 seconds at 130ºC, we can see regions with finer scale and others with coarser scale particles (Figure 32c). The ones with finer scale are the original single-phase region where nucleation was required where in the coarser scale was just growth of existing θ or θ' phase. At higher isotherms and longer time (i.e. 280ºC (2 min and 8 min) and 230ºC (8 min)) mostly growth was going on. The summary table in Figure 32g shows the inter particles distances (λ) for as RS and after annealing experiments.

Figure 33 shows the columnar RS microstructure during annealing in the area consist of discontinuous region and Figure 34 shows the melt pool onset where continues θ are captured in

RS (Figure 34f) and after 180ºC annealing for 8min (Figure 34e), however, after 120 sec at 230ºC annealing (Figure 34c) the melt pool mostly transformed into stable phase were dissolution of θ' occurred and stable θ grew. Figure 35 shows low magnification after 8 min annealing at 280ºC where most of the melt pool consist of stable θ.

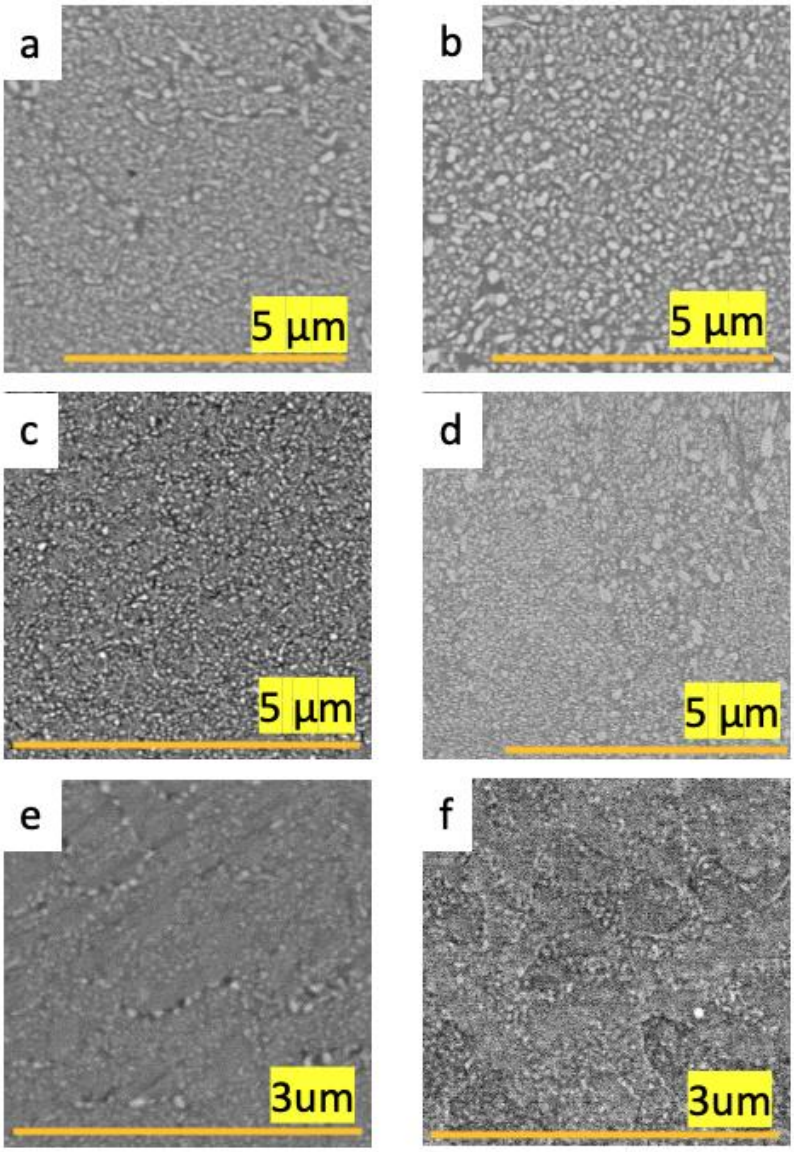

g

	2min	8min
280	λ ≈ 217nm	λ ≈ 268nm
230	λ ≈ 168nm	λ ≈ 300nm
180	no data	λ for both bands ≈ 225nm
		λ of two phase band ≈ 84nm
RS	λ for both bands ≈ 228 nm	
	λ of two phase band ≈ 95nm	

Figure 32 SEM BSE micrographs of the changesin the Banded region during annealing a) 280ºC for 2 min, b) 280ºC for 8 min, c) 230ºC for 2 min, d) 230ºC for 8 min, e) 180ºC for 8 min, f) as RS (no heat treatment) and g) summary of averages for second phase spacing λ for all the different states of banded region in a) – e).

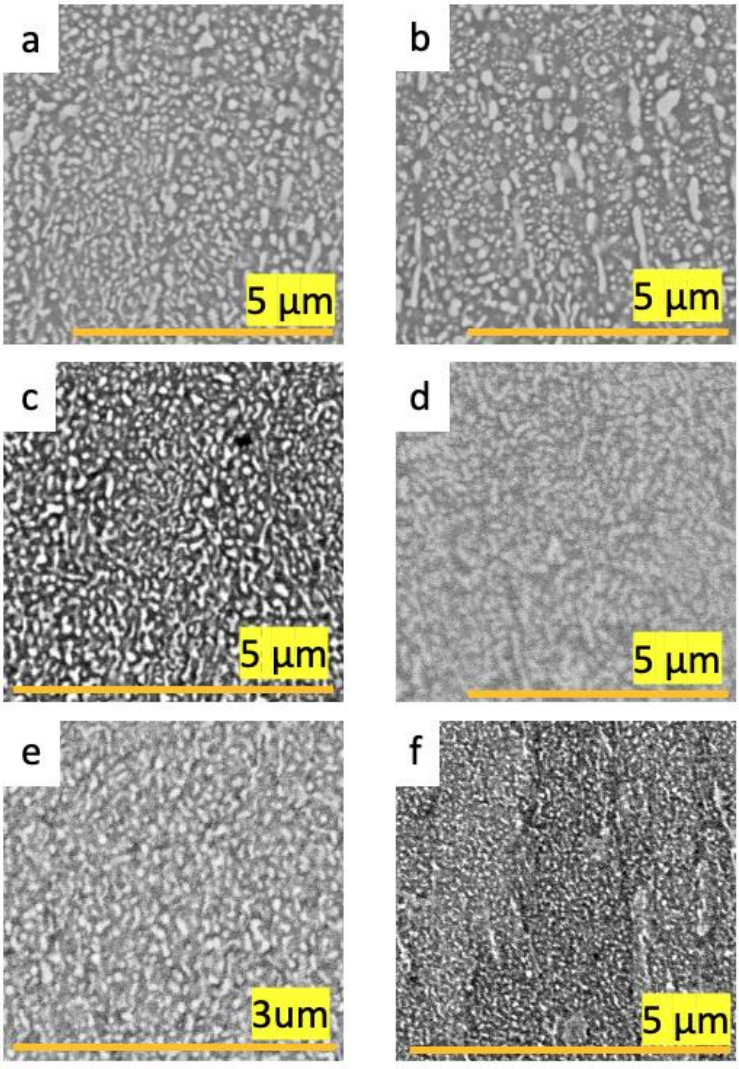

g

	2min	8min
280	λ ≈ 252nm	λ ≈ 300nm
230	λ ≈ 246nm	λ ≈ 390nm
180	no data	λ ≈ 157nm
RS	λ ≈ 200nm	

Figure 33 SEM BSE micrographs of the changes in the columnar grain regions with discontinuous dispersion during annealing a) 280°C for 2 min, b) 280°C for 8 min, c) 230°C for 2 min, d) 230°C for 8 min, e) 180°C for 8min, f) as RS (no heat treatment) and g) summary of averages for second phase spacing λ for all the different states of columnar grains in a) – e).

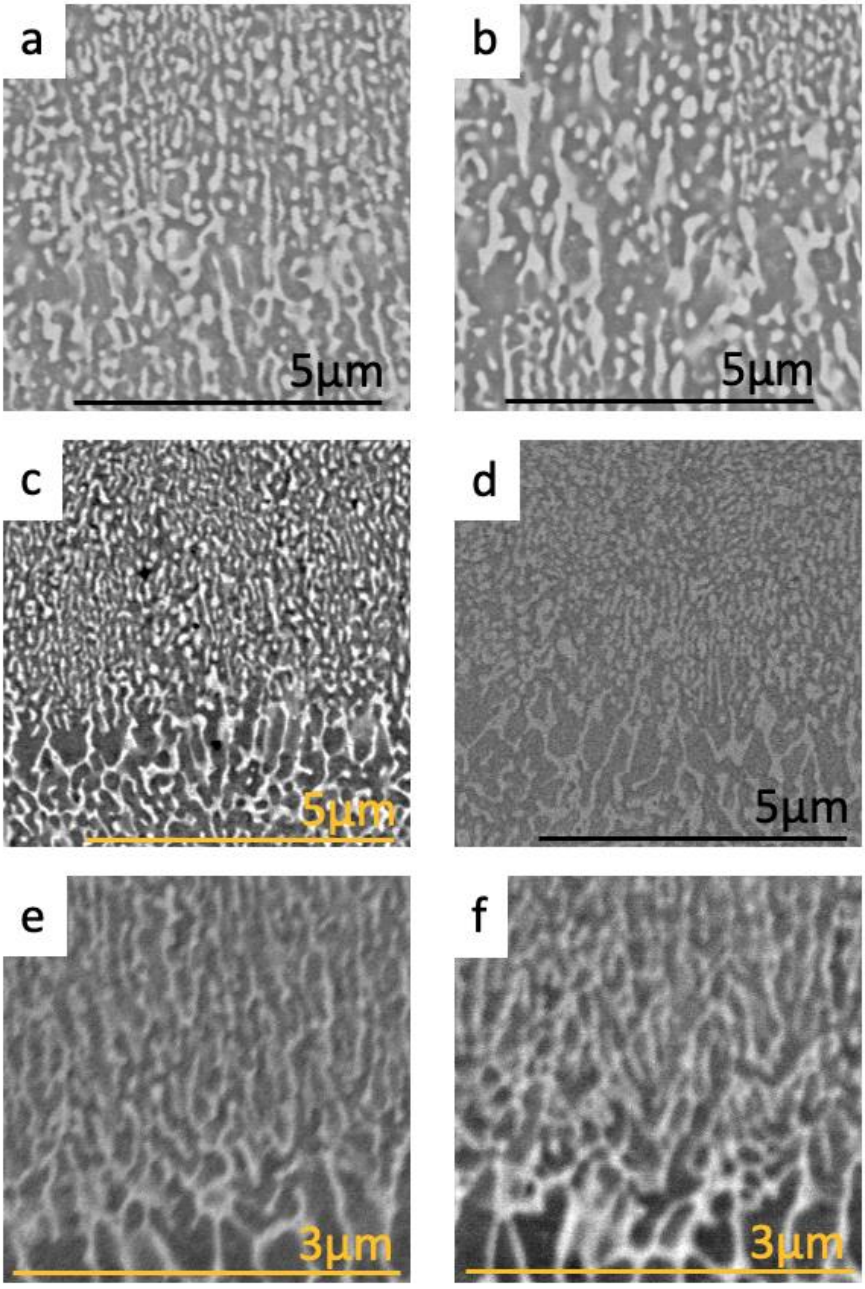

Figure 34 SEM BSE micrographs of the changes in the columnar grain regions with initially continuous dispersion in RS during annealing a) 280ºC for 2 min, b) 280ºC for 8 min, c) 230ºC for 2 min, d) 230ºC for 8 min, e) 180ºC for 8 min, f) as RS (no heat treatment). The transition regions of the RS microstructure at the melt pool perimeters are also shown.

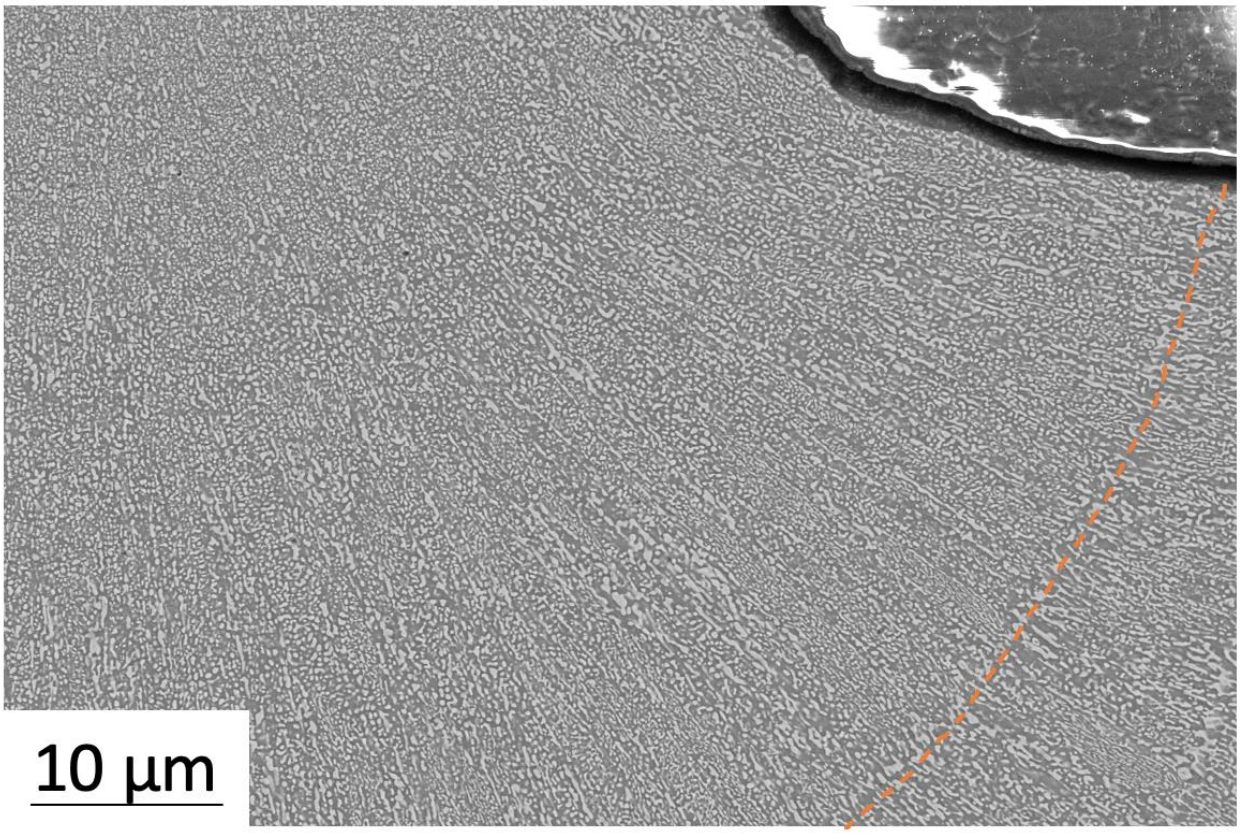

Figure 35 Low magnification SEM BSE micrograph of RS microstructure after 480 seconds of annealing at 280°C.

To build quantitative metrices for the microstructural changes during annealing from the RS microstructure, a manual image analysis via line intercept approach was adopted, since computational image analysis using common and popular image analysis software proved too challenging given the complex nature of the origins of the SEM BSE image contrast encountered. Applying this method revealed significant effects of heat treatment on the second phase spatial distributions and periodicity for the different isotherms explored. Specifically, the occurrence of coarsening could be identified. Figure 36 shows the relationship between

interparticle/interlamellar spacing (λ) and the microstructure morphology after the isothermal annealing for both columnar grain region and the banded region. Here the columnar λ values are measured mostly from the discontinuous θ/θ’ morphology, which is dominant in the RS microstructures formed from the respective melt pools and after annealing (see. Figure 35). Most of the continuous θ-phase regions formed over relatively short growth distances at the beginning of the α-cell region disappeared in the annealed states, since they decompose into discontinuous θ or become very wavy eutectic (Figure 34). Hence, obtaining reliable λ data for continuous θ in the α-cell regions proved challenging. As shown in Figure 33and Figure 36, λ minimum value in the columnar grain obtained for annealing at 180ºC after 8 min. As the temperature and time of annealing increase, the λ increases due to mainly coarsening of θ’ and nucleating of θ. At 230ºC for 8 min, the λ reached a maximum, λ ≈ 400 nm. Increasing the isothermal annealing temperature to 280ºC for 2 min reduces λ by 38%. This can be attributed to nucleation of newer θ and retention of only the largest scale θ’. Increasing the annealing time at the 280˚C isotherm led to completion of the dissolution of θ’ and additional coarsening of the θ, resulting in an increase in the spacing λ. The banded region follows a comparable trend to the columnar grain region as far as the evolution of the spacing λ is concerned. In general, λ in the banded region is smaller than for the columnar grain region. After annealing at 180ºC for 8 min the banded region shows λ ≈ 84 nm, i.e., at this temperature and time the banded region explicitly showed still the two-band morphology of single α-Al phase and two-phase bands. Thus, this small value of λ ≈ 84 nm results only from the two-phase bands (Figure 32). The average spacing for the banded region including both single-phase and two-phase bands is larger at ≈225nm (Figure 32).

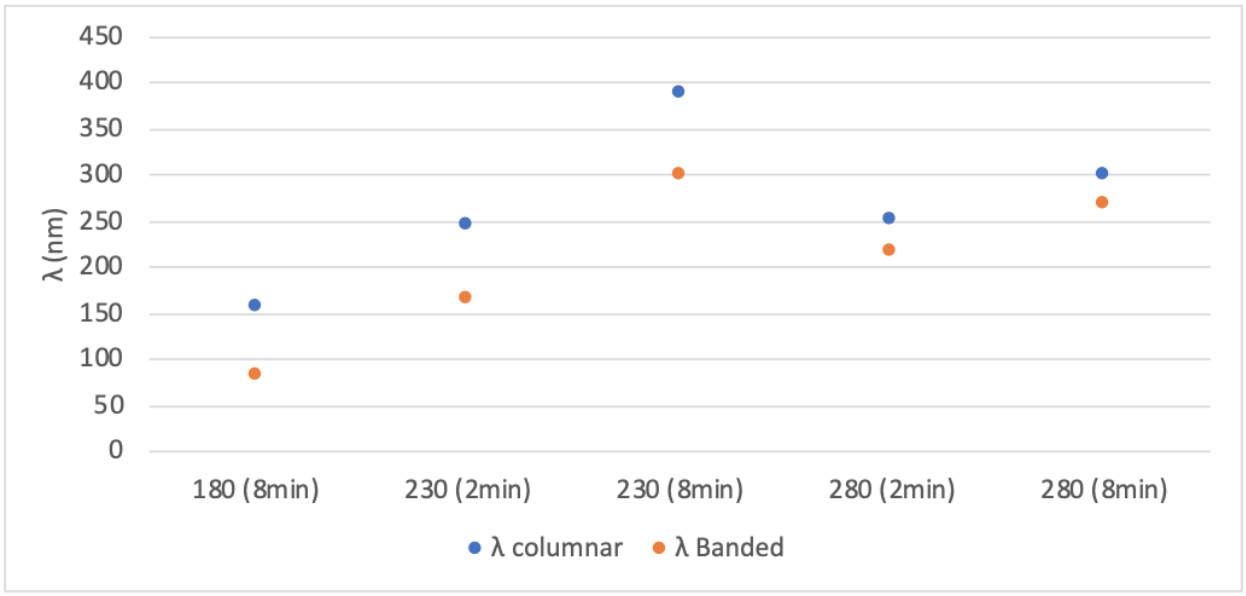

Figure 36 Correlation between inter-particle spacing (λ) and the microstructure morphology after annealing for the columnar grain region and the banded grain region.

4.6.2 Mechanical Properties of RS Changes After Annealing

The nanoindentation hardness (H) measurements show significate differences between as RS microstructure and as annealed states. The average H increased by 9.3% after 8 minutes of annealing at 180ºC in cellular eutectic of the columnar grains or α-cells and by about 21% in the banded region compared to as solidified RS state. For annealing at the higher temperature isotherms of 230˚C and 280 ˚C, the H dropped significantly. The hardness in the columnar grains or α-cells reduced from 3.11±0.16GPa to 2.38±0.12GPa after 2 minutes of annealing at 230ºC. The H decreased to a minimum of 1.87GPa after 8 minutes of 280ºC annealing. This is about 40% of the hardness of the RS microstructure. The H did not change much after annealing at 230ºC for 2 minutes and 280ºC for 2 minutes. In the banded region, in general, a similar behavior for the

hardness evolution during the isothermal annealing treatments was observed. The minimum in H occurred after of annealing for 8 minutes at 280ºC. However, the hardness changes observed during annealing at 230ºC and 280ºC did not show significant differences for the banded region microstructure evolution. The bar chart in Figure 37 summarizes the evolution of the average hardness of the RS microstructure region of the columnar grain region and the banded grain region for the isothermal annealing experiments performed here.

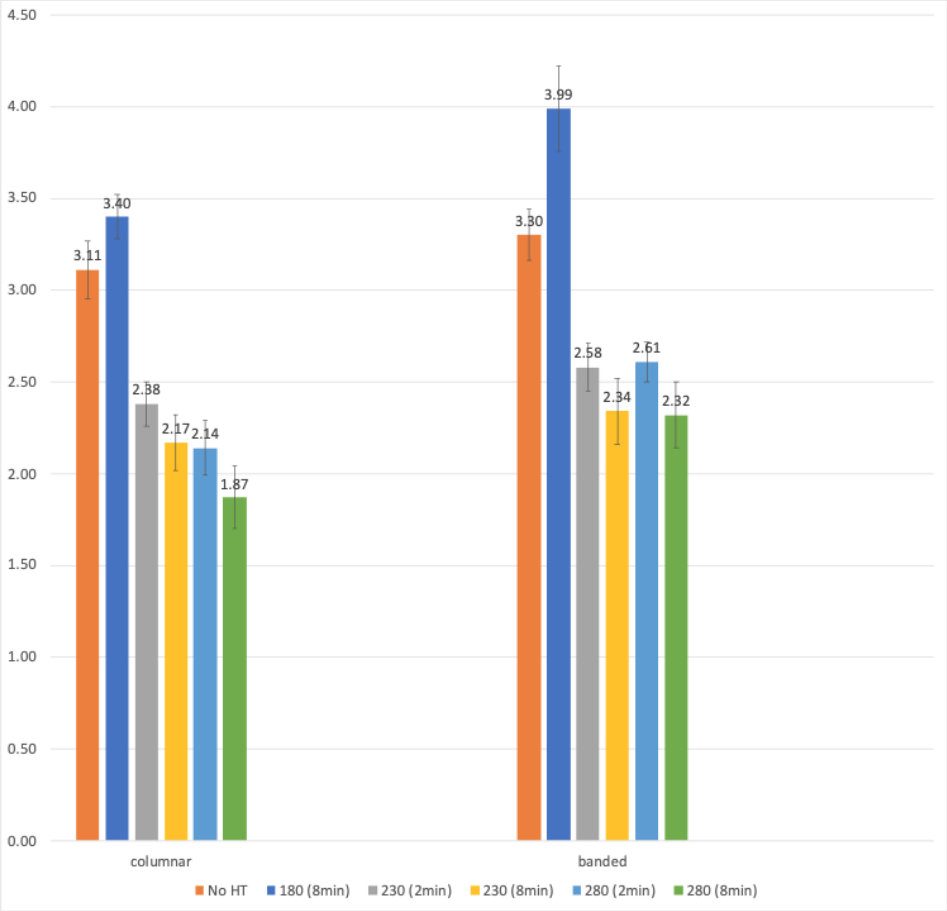

Figure 37 Bar chart of the mean or average of the hardness measurmed prior to (RS state, No HT) and after isothermal annealing for 2min or 8min at 180˚C, 230˚C and 280˚C, respectively.

Applying the two-means t-test to the hardness measurements of the annealed samples facilitated assessment of the statistical significance of the different mean hardness values obtained experimentally for the different annealing states. The null hypothesis is, $\mu_1-\mu_2= 0$, the alternative hypothesis is $\mu_1-\mu_2 \neq 0$, with $\alpha = 5\%$. Here, μ_1 and μ_2 are the mean hardness values for the two data sets form the annealing states to be compared and a is the selected significance level. With respect to the columnar region, it was found that the differences of hardness mean for the RS columnar regions prior to annealing (in the RS state), μ_1, and after annealing at 180ºC for 8min, μ_2, are statistically significant, i.e., $\mu_1 \neq \mu_2$. The t-test also confirmed that the experimentally measured hardness means for the banded region prior to annealing in the RS state and after annealing at 180ºC for 8min are statistically significant. Notably, the average hardness of the columnar regions and banded region for the RS microstructure prior to annealing are based on the average of all hardness values from the columnar region, including continuous and discontinuous θ for the columnar grains, and for the banded region including both two-phase band and combined single-phase and two-phase bands (Table 8). The t-test revealed statistically significant differences for the means of the hardness measurements for the columnar grain regions and the banded grain regions obtained for 2 min and for 8 min annealing at 230˚C. Similarly, the t-tests revealed that mean hardness values are statistically different for 2 min and 8 min of annealing at 280ºC for the columnar grain and banded grain regions, respectively. In summary, the t-tests confirm the differences of the experimentally measured hardness mean values graphically represented in the bar chart of Figure 36 are significant.

Considering the evolution of the microstructural metric of the inter-particle spacing (λ) (section 4.6.1), the hardness of the two-phase microstructure in the columnar grain and banded regions established after RS related inversely with λ (see Figure 37, Figure 38a). The straight

dashed lines in Figure 38a are linear fits to the experimental data sets for the hardness, H, and spacings, λ, are shown to guide the eye-of-the-reader and are included for illustration purpose only. The highest H valued relates to the smallest λ; i.e., at λ ≈ 85nm ➔ H ≈ 4 GPa, Figure 38a. Isothermal annealing at 180ºC shows highest H and smallest λ in banded (85nm and 4GPa, respectively) and columnar grain regions (157nm and 3.4GPa, respectively). However, the largest λ ≈ 390nm did not show the lowest H. There are additional inconsistencies regarding the inverse relationship between hardness, H, and particle spacing, λ, displayed in the date of Figure 38a. For instance, H values are similar after annealing at 230ºC (2min) and 280ºC (2min) in the banded region, even though the average λ is larger by ≈ 30% at 217nm for the 280˚C annealed state relative 168nm of the 230˚C annealed state. Although the spacings, λ, are similar (λ ≈ 300nm) after annealing at 280ºC (8min) for the columnar region and for 230ºC (8min) in the banded region, the H of the later is larger by 25%. However, taken as individual measurements for the two-phase microstructure metric, λ, and the mechanical property, H, in general, these values are consistent with recent published hardness measurements for regular lamellar eutectic of Al-Cu alloy [15], see Figure 38b. However, it was clearly shown in the discussion in the preceding section on the hardness-morphology-interparticle spacing relationships that there are not just scale effects but also morphology effects that have to be considered for the evolution of the RS microstructure and its hardness during annealing. Figure 38c shows the inter-particles spacing evolution during annealing by sorting λ values in ascending order. Clearly, annealing the RS microstructure at 180ºC for 8 min produces the minimum λ and at annealing at 230ºC for 8 min shows highest λ values. This is an apparent anomaly, since coarsening of a two-phase microstructure would be expected to yield the largest value of spacing between the second phase particles for the longest annealing time for the highest isotherm. However, rather than being an artifact, this unexpected

behavior could be potentially related to the effect from the required phase transformation of the metastable θ'-phase in the RS microstructure to establish the thermodynamically stable θ-phase via nucleation and growth. It can be envisaged that a state evolved for the 230˚C isotherm where most of the θ'-phase particles, preferentially the smaller ones have been dissolved with some larger remaining, while θ-phase has also formed in significant fraction but has not had enough time to coarsen enough to reduce the hardness in accordance with the increased spacing values to be consistent with the behavior of the other two isotherms.

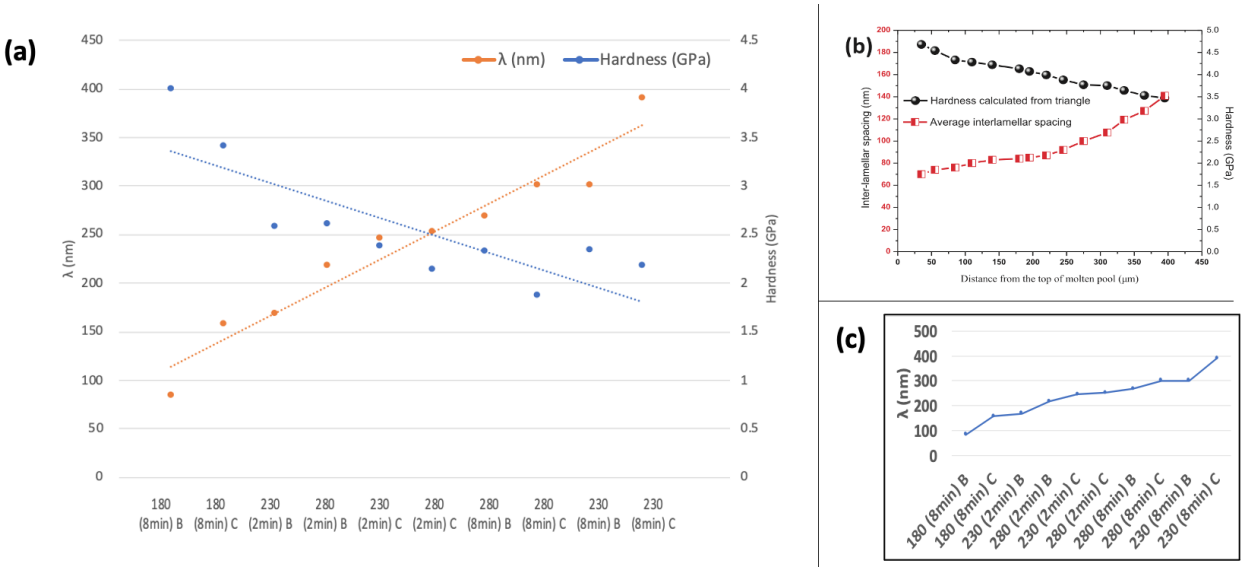

Figure 38 a) the plot relate second phase particles spacing λ vs hardness with respect to annealed microstructure morphology (i.e. C: columnar and B: banded region), b) hardness vs eutectic frequancy (λ) adopted from [15] and c) a plot shows the second phase particles spacing λ ranked from smallest λ to largest λ with respet to annealed microstructure morphology.

The reductions in H values after annealing could be attributed to the type of second phase particle, i.e. θ or θ', as well as the size and distribution. For example, at 280ºC and 2 minutes annealing, based on the highly irregular shapes that are encountered for many of the second phase

particles it can be concluded that most of the existing particles transformed to θ phase. However, some θ’ phase may persist as they did not dissolve and slightly grew. Thus, the H values is higher compared to state after 8 minutes annealing where all the particles transformed into θ phase. This type of behavior is also noticeable in the banded region where θ and θ’ phases co-existed at both annealing time which always was showing slight increase in H compared to cellular eutectic region. The H reduction at 8 minutes where the θ phase has overaged can be attributed to the larger distance between particles which governs the Orowen mechanism where in banded region we still have a combination of large and small semi coherent θ’ phase which is shearable and θ phase with larger density, see Figure 39 to Figure 41. These are speculative arguments and additional work is required to elucidate in more detail these differences in microstructure-property relations for the evolving RS microstructure regions, especially for the transitions stages when multiple different phases may be present in the populations of hardening inducing dislocation glide obstacles, in response thermal annealing.

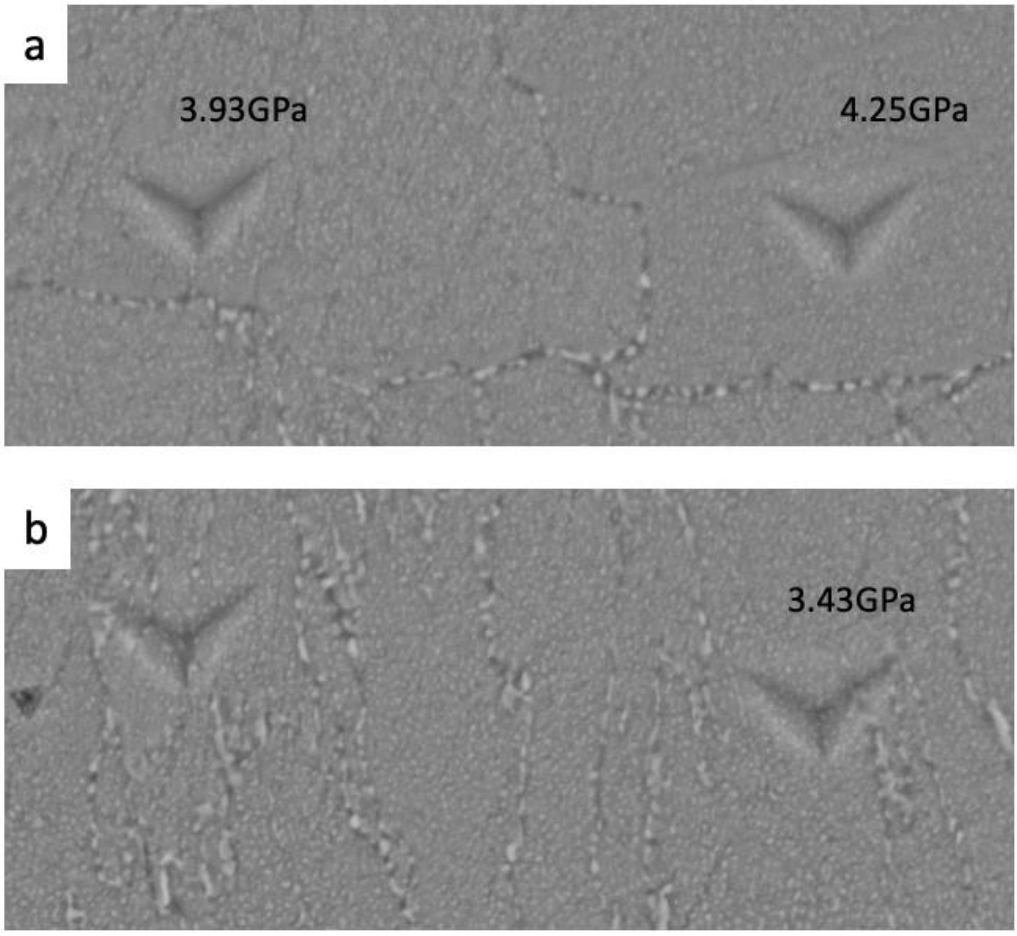

Figure 39 SEM micrographs show sample of the indents on RS microstructures annealed at 180C for 8 min. a)banded region and b) columnar cell.

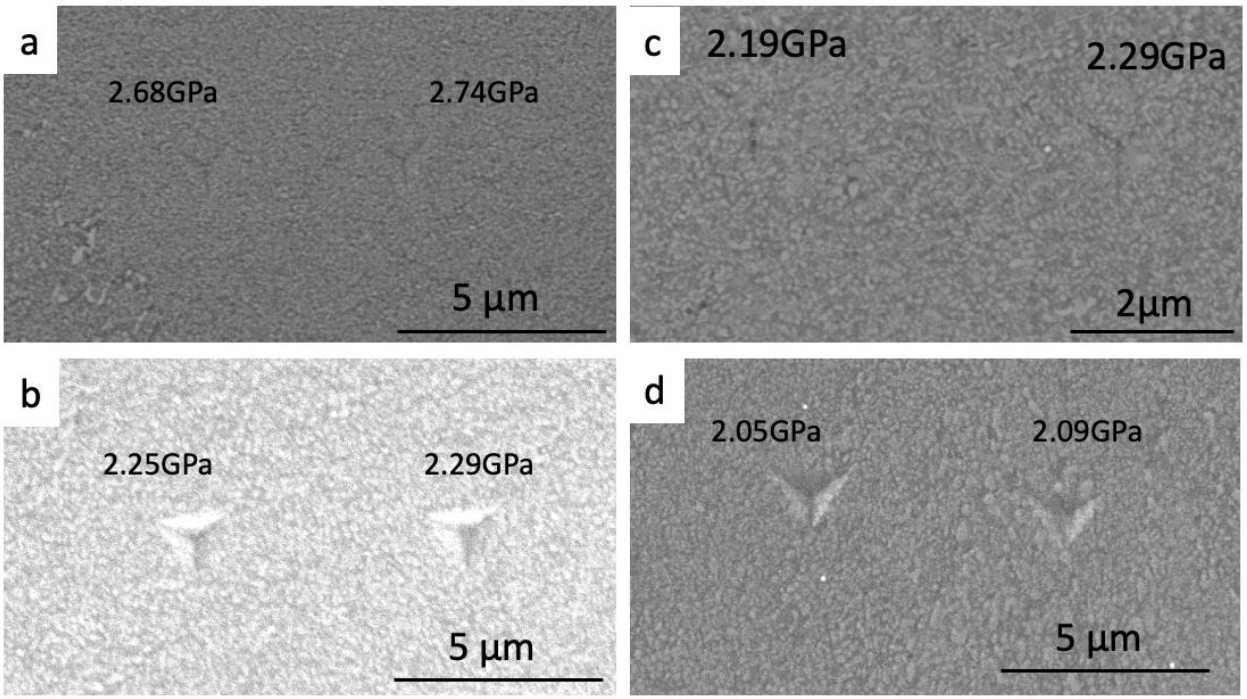

Figure 40 SEM micrographs show sample of the indents on RS microstructures annealed at 230C. a) banded region annealed for 2 min, b) columnar cell annealed for 2 min, c) banded region annealed for 8 min and d) columnar cell annealed for 8 min

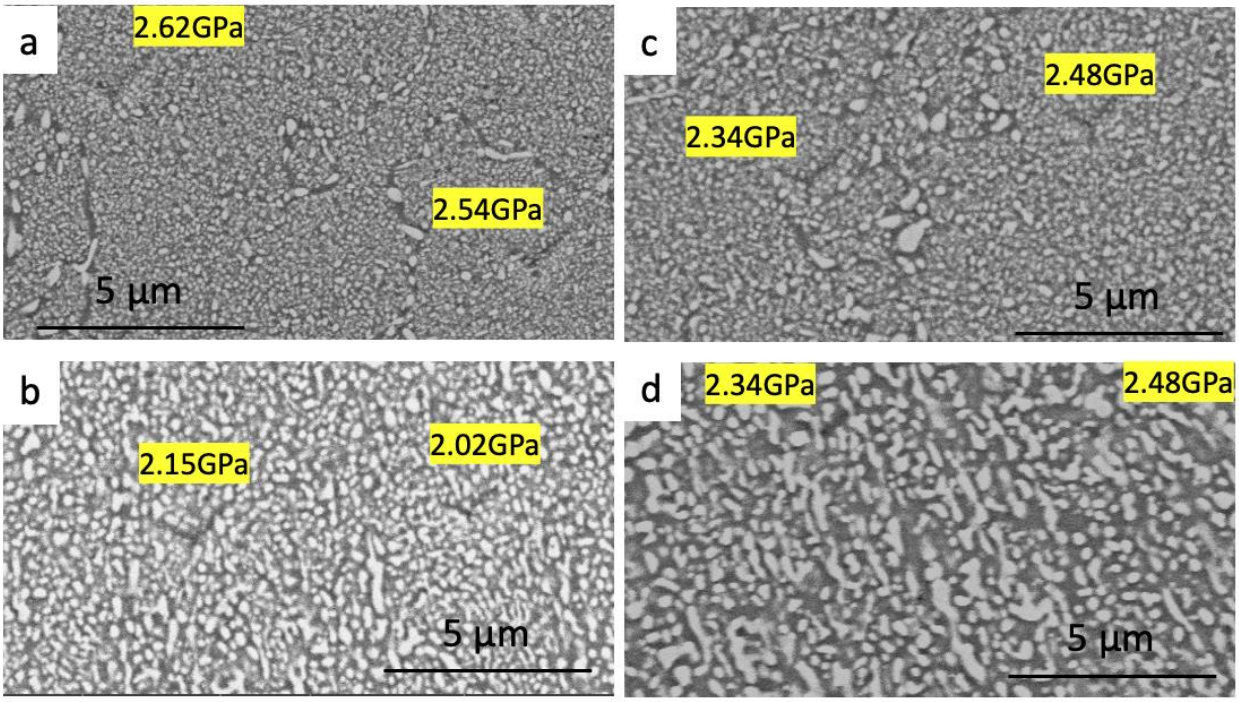

Figure 41 SEM micrographs show sample of the indents on RS microstructures annealed at 280C. a) banded region annealed for 2 min, b) columnar cell annealed for 2 min, c) banded region annealed for 8 min and d) columnar cell annealed for 8 min

4.7 Conclusion

Scanned laser melting (SLM) and subsequent re-solidification results in the formation of solidification microstructures that form under continuously changing conditions. The solidification starts via growth of new solid seeded by the supporting bulk solid substrate behind a solid-liquid interface that migrates at an increasing rate. Increasing the solidification and crystal growth rate leads to changes in the resulting microstructure. For hypo-eutectic Al-Cu alloy, these changes include the initial transition of a planar growth interface morphology to cellular growth, from cellular to dendritic, and as the growth rate increases further to cellular and finally planar growth and banded region. After laser melting rapid solidification (RS) the microstructures of these multicomponent alloys exhibit morphological gradients, scale refinement, non-equilibrium phases and solute trapping, and associated property changes.

In this study scanned laser melting was performed on Al-10% at.Cu. The developed RS microstructure at scanned laser velocity of ≈ 3mm/s formed mostly via a cellular growth mode for the primary α-Al phase and exhibited significant rapid solidification behavior. The solute trapping in α-Al cells increased by ≈ 20% compared to the equilibrium solid solubility limit of ~2.5at% and showed microstructure refinement from several tens of μm to 1-2 μm. Examining the mechanical properties of RS α-Al(Cu) cells showed hardness enhancement by 36% compared to the equilibrium solute content of the α-Al(Cu) in the as-cast state. Using established strengthening models for Al alloys the observed hardness increase of the scale refined and solute supersaturated α-Al(Cu) cells has been attributed to a combination of approximately equal contributions of solute and grain size hardening.

Increasing the laser velocity to the range of $1m/s \leq V_L \leq 4ms$, allowed us to achieve higher solidification rates and distinct microstructure morphologies that are characteristic of hypo-eutectic Al-Cu alloys are revealed. For the Al-10Cu alloy the liquid/ solid interface velocity reached critical values that are associated with the transition of the solidification interface morphology from cellular to dendritic, dendritic to cellular and from cellular to planar with maximum V_{SL} approaching V_L at the top of the melt pool, i.e., increases of $V_{SL} \geq 0.8m/s$ are observed. The nanoindentation measurements showed hardness increases in the melt pool of about 258% to 571% compared to the pure Al and 145% to 327% compared to the as-cast α-Al(Cu) solid solution. These hardness measurements were similar to the hardness of lamellar Al-Cu regular eutectic. Also, the mechanical properties of the non-equilibrium multi-phase microstructure region of the columnar grains of α-cells and the banded region were identified.

Heat treatment annealing of the RS microstructure was conducted at different isotherms (180ºC, 230ºC and 280ºC) to examine the effects of the scale and nature of the Al_2Cu-based population of second phases (i.e., θ' and θ) in the melt pool. During annealing, there was nucleation and growth of second phase particles across the melt pool. For example, in the single-phase band where we still can recognize the partitionless region after 120 seconds at 130ºC, we can see regions with finer scale and others with coarser scale particles. The ones with finer scale are the original single-phase region where nucleation was required whereas in the coarser scale was just growth of the existing θ or θ' phase. At higher isotherms and longer time (i.e. 280ºC (2 min and 8 min) and 230ºC (8 min)) mostly growth was going on. The mechanical property evolution for morphologically distinct regions in the alloy microstructure during annealing (aging) has been determined. For the banded region of the RS microstructure during annealing at 180˚C an age-hardening behavior has been observed, while softening was the case even for the shortest times

during annealing at the higher annealing temperatures, The other morphologically distinct regions exhibited softening during the annealing treatments. Transformation of the supersaturated solid solution α-Al(Cu) phase volumes presenting in the single-phase bands of the banded regions to two-phase regions comprised of nano-scale Al_2Cu phase and α-Al(Cu) phase has been proposed as the origin for the initial age-hardening observed for 180˚C annealing. Softening has been attributed to coarsening of the continuous θ-Al_2Cu and the dis-continuous θ'-Al_2Cu and transformation in the columnar of the metastable θ'-Al_2Cu to θ-Al_2Cu.θ-Al_2Cu and the dis-continuous θ'-Al_2Cu and transformation in the columnar of the metastable θ'-Al_2Cu to θ-Al_2Cu.

5.0 Achievements and Outlook

This work is driven by two main aspects:

1- Impact the fundamental of basic materials science knowledge.

2- Developing and evaluation an experimental method approach to measure the mechanical properties of metastable microstructure produced by rapid solidification.

Based on the results shown and discussed in this dissertation, it can be summarized as follow:

- Laser surface remelting has been used to produce rapid solidification microstructure of showing planar to cellular, cellular to dendritic, dendritic to cellular, and cellular to planar then banded region in hypoeutectic Al-10Cu alloy.
- The methodology of using nanoindentation method has successfully proven it can measure the mechanical properties of different RS microstructure morphologies long as the indent size is smaller than desired morphology.
- The heat treatment experiments at different isotherms (180ºC, 230ºC and 280ºC) shows rapid θ` to θ transformation. The nanoindentation testing followed that shows significant hardness, H, variation at 180ºC isotherm compared to as rapid solidified microstructure and other isotherms.

5.1 Future Work

Having deformed microstructure from high concertation α-Al(Cu) region and unusual population of second phase θ’ with spheroidal shape. To see how the dislocation interact with the obstacles present by extracting FIB lamella.

Also, an FIB micropillars and using SEM to make compression testing from different regions. Then, creates FIB section from these deformed micro pilers to study the compression induced deformation response of that microstructure.

Appendix A Two-Means T-Test Reports

Method

μ_1: population mean of 180-Col

μ_2: population mean of average noHT columnar

Difference: $\mu_1 - \mu_2$

Equal variances are assumed for this analysis.

Descriptive Statistics

Sample	N	Mean	StDev	SE Mean
180-Col	17	3.398	0.148	0.036
average noHT columnar	30	3.119	0.218	0.040

Estimation for Difference

Difference	Pooled StDev	95% CI for Difference
0.2789	0.1964	(0.1588, 0.3990)

Test

Null hypothesis $H_0: \mu_1 - \mu_2 = 0$

Alternative hypothesis $H_1: \mu_1 - \mu_2 \neq 0$

T-Value	DF	P-Value
4.68	45	0.000

Method

μ_1: population mean of 180-Bnad

μ_2: population mean of average banded

Difference: $\mu_1 - \mu_2$

Equal variances are assumed for this analysis.

Descriptive Statistics

Sample	N	Mean	StDev	SE Mean
180-Bnad	3	3.993	0.232	0.13
average banded	15	3.217	0.242	0.063

Estimation for Difference

Difference	Pooled StDev	95% CI for Difference
0.776	0.241	(0.453, 1.099)

Test

Null hypothesis $H_0: \mu_1 - \mu_2 = 0$

Alternative hypothesis $H_1: \mu_1 - \mu_2 \neq 0$

T-Value	DF	P Value
5.09	16	0.000

Method

μ_1: population mean of 230-col-2min

μ_2: population mean of 230-col-8min

Difference: $\mu_1 - \mu_2$

Equal variances are assumed for this analysis.

Descriptive Statistics

Sample	N	Mean	StDev	SE Mean
230-col-2min	18	2.381	0.121	0.029
230-col-8min	14	2.169	0.153	0.041

Estimation for Difference

Difference	Pooled StDev	95% CI for Difference
0.2125	0.1360	(0.1136, 0.3115)

Test

Null hypothesis $H_0: \mu_1 - \mu_2 = 0$

Alternative hypothesis $H_1: \mu_1 - \mu_2 \neq 0$

T-Value	DF	P-Value
4.39	30	0.000

Method

μ_1: population mean of 230-band-2min

μ_2: population mean of 230-band-8min

Difference: $\mu_1 - \mu_2$

Equal variances are assumed for this analysis.

Descriptive Statistics

Sample	N	Mean	StDev	SE Mean
230-band-2min	8	2.584	0.127	0.045
230-band-8min	6	2.337	0.183	0.075

Estimation for Difference

Difference	Pooled StDev	95% CI for Difference
0.2471	0.1530	(0.0670, 0.4271)

Test

Null hypothesis	$H_0: \mu_1 - \mu_2 = 0$
Alternative hypothesis	$H_1: \mu_1 - \mu_2 \neq 0$

T-Value	DF	P-Value
2.99	12	0.011

Method

μ_1: population mean of 280-col-2min

μ_2: population mean of 280-col-8min

Difference: $\mu_1 - \mu_2$

Equal variances are assumed for this analysis.

Descriptive Statistics

Sample	N	Mean	StDev	SE Mean
280-col-2min	35	2.141	0.130	0.022
280-col-8min	18	1.899	0.180	0.042

Estimation for Difference

Difference	Pooled StDev	95% CI for Difference
0.2420	0.1489	(0.1553, 0.3287)

Test

Null hypothesis	$H_0: \mu_1 - \mu_2 = 0$
Alternative hypothesis	$H_1: \mu_1 - \mu_2 \neq 0$

T-Value	DF	P-Value
5.60	51	0.000

Method

μ_1: population mean of 280-band-2min

μ_2: population mean of 280-band-8min

Difference: $\mu_1 - \mu_2$

Equal variances are assumed for this analysis.

Descriptive Statistics

Sample	N	Mean	StDev	SE Mean
280-band-2min	8	2.608	0.106	0.038
280-band-8min	8	2.316	0.180	0.064

Estimation for Difference

Difference	Pooled StDev	95% CI for Difference
0.2913	0.1478	(0.1327, 0.4498)

Test

Null hypothesis	$H_0: \mu_1 - \mu_2 = 0$
Alternative hypothesis	$H_1: \mu_1 - \mu_2 \neq 0$

T-Value	DF	P-Value
3.94	14	0.001

Bibliography

[1] M. A. Otooni, *Elements of rapid solidification: fundamentals and applications*, vol. 29. Springer Science & Business Media, 2013.

[2] S. C. Gill, M. Zimmermann, and W. Kurz, "Laser resolidification of the AlAl2Cu eutectic: The coupled zone," *Acta Metall. Mater.*, vol. 40, no. 11, pp. 2895–2906, Nov. 1992.

[3] V. Bathula, C. Liu, K. Zweiacker, J. McKeown, and J. M. K. Wiezorek, "Interface velocity dependent solute trapping and phase selection during rapid solidification of laser melted hypo-eutectic Al-11at.%Cu alloy," *Acta Mater.*, vol. 195, pp. 341–357, Aug. 2020.

[4] J. D. Roehling *et al.*, "Rapid solidification growth mode transitions in Al-Si alloys by dynamic transmission electron microscopy," *Acta Mater.*, vol. 131, pp. 22–30, Jun. 2017.

[5] J. T. McKeown *et al.*, "Time-Resolved In Situ Measurements During Rapid Alloy Solidification: Experimental Insight for Additive Manufacturing," *JOM*, vol. 68, no. 3, pp. 985–999, Mar. 2016.

[6] M. Zimmermann, M. Carrard, and W. Kurz, "Rapid solidification of Al-Cu eutectic alloy by laser remelting," *Acta Metall.*, vol. 37, no. 12, pp. 3305–3313, 1989.

[7] W. J. Boettinger and S. R. Coriell, "Microstructure Formation in Rapidly Solidified Alloys.," *NATO ASI Ser. Ser. E Appl. Sci.*, no. 114, pp. 81–108, 1986.

[8] M. Rappaz, B. Carrupt, M. Zimmermann, and W. Kurz, "Numerical simulation of eutectic solidification in the laser treatment of materials," *Helv. Phys. Acta*, no. 60, pp. 924–36, 1987.

[9] K. W. Zweiacker, C. Liu, M. A. Gordillo, J. T. McKeown, G. H. Campbell, and J. M. K.

Wiezorek, “Composition and automated crystal orientation mapping of rapid solidification products in hypoeutectic Al-4 at.%Cu alloys,” *Acta Mater.*, vol. 145, pp. 71–83, Feb. 2018.

[10] W. Kurz, B. Giovanola, and R. Trivedi, “Theory of microstructural development during rapid solidification,” *Acta Metall.*, vol. 34, no. 5, pp. 823–830, May 1986.

[11] D. W. Heard, R. Gauvin, and M. Brochu, “Non-equilibrium solute partitioning in a laser re-melted Al–Li–Cu alloy,” *Acta Mater.*, vol. 61, no. 19, pp. 7432–7436, Nov. 2013.

[12] D. Danilov and B. Nestler, “Phase-field modelling of solute trapping during rapid solidification of a Si–As alloy,” *Acta Mater.*, vol. 54, no. 18, pp. 4659–4664, Oct. 2006.

[13] K. Wang, H. Wang, F. Liu, and H. Zhai, “Modeling rapid solidification of multi-component concentrated alloys,” *Acta Mater.*, vol. 61, no. 4, pp. 1359–1372, Feb. 2013.

[14] J. T. McKeown *et al.*, “In situ transmission electron microscopy of crystal growth-mode transitions during rapid solidification of a hypoeutectic Al–Cu alloy,” *Acta Mater.*, vol. 65, pp. 56–68, Feb. 2014.

[15] Q. Lei, B. P. Ramakrishnan, S. Wang, Y. Wang, J. Mazumder, and A. Misra, “Structural refinement and nanomechanical response of laser remelted Al-Al2Cu lamellar eutectic,” *Mater. Sci. Eng. A*, vol. 706, pp. 115–125, Oct. 2017.

[16] S. C. Gill and W. Kurz, “Rapidly solidified AlCu alloys-I. experimental determination of the microstructure selection map,” *Acta Metall. Mater.*, vol. 41, no. 12, pp. 3563–3573, 1993.

[17] S. J. Wang, D. Y. Xie, J. Wang, and A. Misra, “Deformation behavior of nanoscale Al–Al2Cu eutectics studied by in situ micropillar compression,” *Mater. Sci. Eng. A*, vol. 800, p. 140311, 2021.

[18] Y. Du *et al.*, “Diffusion coefficients of some solutes in fcc and liquid Al: critical evaluation

and correlation," *Mater. Sci. Eng. A*, vol. 363, no. 1–2, pp. 140–151, Dec. 2003.

[19] D. Andre *et al.*, "Dislocation-mediated plasticity in the Al2Cu θ-phase," *Acta Mater.*, vol. 209, p. 116748, May 2021.

[20] J. Emsley, *The Elements*, 2nd ed. Oxford : Clarendon Press, 1991.

[21] D. A. Porter and K. E. Easterling, *Phase transformations in metals and alloys (revised reprint)*. CRC press, 2009.

[22] S. J. Andersen, C. D. Marioara, J. Friis, S. Wenner, and R. Holmestad, "Precipitates in aluminium alloys," *Adv. Phys. X*, vol. 3, no. 1, p. 1479984, Jan. 2018.

[23] H. Fredriksson and U. Åkerlind, *Solidification and Crystallization Processing in Metals and Alloys*. 2012.

[24] K. Carling, G. Wahnström, T. R. Mattsson, A. E. Mattsson, N. Sandberg, and G. Grimvall, "Vacancies in metals: from first-principles calculations to experimental data," *Phys. Rev. Lett.*, vol. 85, no. 18, p. 3862, 2000.

[25] P. Dumitraschkewitz, S. S. A. Gerstl, L. T. Stephenson, P. J. Uggowitzer, and S. Pogatscher, "Clustering in Age-Hardenable Aluminum Alloys," *Adv. Eng. Mater.*, vol. 20, no. 10, p. 1800255, Oct. 2018.

[26] G. E. Dieter, *Mechanical metallurgy*. 2011.

[27] S. Liu, E. Martínez, and J. LLorca, "Prediction of the Al-rich part of the Al-Cu phase diagram using cluster expansion and statistical mechanics," *Acta Mater.*, vol. 195, pp. 317–326, 2020.

[28] J. M. Silcock, T. J. Heal, and H. K. Hardy, "Structural ageing characteristics of binary aluminium-copper alloys," *J. Inst. Met.*, vol. 82, 1954.

[29] J.-H. JANG, D.-G. NAM, Y.-H. PARK, and I.-M. PARK, "Effect of solution treatment and

artificial aging on microstructure and mechanical properties of Al–Cu alloy," *Trans. Nonferrous Met. Soc. China*, vol. 23, no. 3, pp. 631–635, 2013.

[30] P. Yu, C. K. Kwok, C. Y. To, T. K. Li, and D. H. L. Ng, "Enhanced precipitation hardening in an alumina reinforced Al–Cu alloy matrix composite," *Compos. Part B Eng.*, vol. 39, no. 2, pp. 327–331, 2008.

[31] F. R. Brotzen, C. T. Rosemayer, and R. J. Gale, "Mechanical behavior of aluminum and Al-Cu(2%) thin films," *Thin Solid Films*, vol. 166, pp. 291–298, 1988.

[32] G. F. W. and G. Martha, "Precipitation Hardening in the First Aerospace Aluminum Alloy: The Wright Flyer Crankcase," *Science (80-.).*, vol. 266, no. 5187, pp. 1015–1017, Nov. 1994.

[33] J. M. Silcock, T. J. Heal, and H. K. Hardy, "Structural Ageing Characteristics of Binary Aluminium-Copper Alloys," *J. Inst. Met.*, vol. 82, pp. 239–248, 1954.

[34] W. Kurz and D. F. Fisher, *Fundamentals of solidification*. Trans Tech Publications, 1984.

[35] J. A. Dantzig and M. Rappaz, *Solidification: -Revised & Expanded*. EPFL press, 2016.

[36] I. Minkoff, *Materials Processes: A Short Introduction*. Springer Berlin Heidelberg, 2012.

[37] L. Habraken and J. L. de Brouwer, "De Ferri Metallographia Bd. I," *Grundlagen der Metallogr. Eur. Gemeinschaft für Kohle und Stahl*, 1966.

[38] D. M. Stefanescu, *Science and engineering of casting solidification: Third edition*. Springer, 2015.

[39] J. D. Hunt, "Solidification and casting of metals," *Met. Soc. London*, vol. 3, 1979.

[40] W. Kurz and D. J. Fisher, "Dendrite growth at the limit of stability: tip radius and spacing," *Acta Metall.*, vol. 29, no. 1, pp. 11–20, 1981.

[41] D. B. Williams and J. W. Edington, "Microstructural characteristics of splatquenched

aluminium-copper alloys," *J. Mater. Sci.*, vol. 12, no. 1, pp. 126–130, 1977.

[42] R. K. Singh, K. Chattopadhyay, S. Lele, and T. R. Anantharaman, "Impact of substrate temperature on rapid solidification of an Al-Cu eutectic alloy," *J. Mater. Sci.*, vol. 17, no. 6, pp. 1617–1622, 1982.

[43] M. Carrard, M. Gremaud, M. Zimmermann, and W. Kurz, "About the banded structure in rapidly solidified dendritic and eutectic alloys," *Acta Metall. Mater.*, vol. 40, no. 5, pp. 983–996, 1992.

[44] K. A. Jackson and J. D. Hunt, "Lamellar and Rod Eutectic Growth," in *Dynamics of Curved Fronts*, Elsevier, 1988, pp. 363–376.

[45] T. Zheng *et al.*, "Solute trapping in Al-Cu alloys caused by a 29 Tesla super high static magnetic field," *Sci. Rep.*, vol. 9, no. 1, p. 266, Dec. 2019.

[46] N. K. Bhoi, H. Singh, S. Pratap, and P. K. Jain, "Aluminum Yttrium Oxide Metal Matrix Composite Synthesized by Microwave Hybrid Sintering: Processing, Microstructure and Mechanical Response," *J. Inorg. Organomet. Polym. Mater.*, Jan. 2022.

[47] C.-L. Chen, A. Richter, and R. C. Thomson, "Mechanical properties of intermetallic phases in multi-component Al–Si alloys using nanoindentation," *Intermetallics*, vol. 17, no. 8, pp. 634–641, Aug. 2009.

[48] H. Somekawa and C. A. Schuh, "Effect of solid solution elements on nanoindentation hardness, rate dependence, and incipient plasticity in fine grained magnesium alloys," *Acta Mater.*, vol. 59, no. 20, pp. 7554–7563, Dec. 2011.

[49] D. Buchbinder, H. Schleifenbaum, S. Heidrich, W. Meiners, and J. Bültmann, "High Power Selective Laser Melting (HP SLM) of Aluminum Parts," *Phys. Procedia*, vol. 12, pp. 271–278, 2011.

[50] B. Bhushan and M. L. B. Palacio, “Nanoindentation,” in *Encyclopedia of Nanotechnology*, vol. 387, no. 2001, Dordrecht: Springer Netherlands, 2016, pp. 2423–2444.

[51] W. C. Oliver and G. M. Pharr, “An improved technique for determining hardness and elastic modulus using load and displacement sensing indentation experiments,” *J. Mater. Res.*, vol. 7, no. 6, pp. 1564–1583, 1992.

[52] A. C. Fischer-Cripps, *Nanoindentation*. New York, NY: Springer New York, 2011.

[53] M. van Elsen, F. Al-Bender, and J. Kruth, “Application of dimensional analysis to selective laser melting,” *Rapid Prototyp. J.*, vol. 14, no. 1, pp. 15–22, Jan. 2008.

[54] R. Trivedi and W. Kurz, “Dendritic growth,” *Int. Mater. Rev.*, vol. 39, no. 2, pp. 49–74, Jan. 1994.

[55] L. F. Mondolfo, *Aluminum alloys: structure and properties*. Elsevier, 2013.

[56] J. Zander and R. Sandström, “One parameter model for strength properties of hardenable aluminium alloys,” *Mater. Des.*, vol. 29, no. 8, pp. 1540–1548, 2008.

[57] L. B. Ber, “Accelerated artificial ageing regimes of commercial aluminium alloys. II: Al–Cu, Al–Zn–Mg–(Cu), Al–Mg–Si–(Cu) alloys,” *Mater. Sci. Eng. A*, vol. 280, no. 1, pp. 91–96, Mar. 2000.

[58] S. C. Wang and M. J. Starink, “Precipitates and intermetallic phases in precipitation hardening Al-Cu-Mg-(Li) based alloys,” *Int. Mater. Rev.*, vol. 50, no. 4, pp. 193–215, 2005.

[59] J. Noordhuis and J. T. M. de Hosson, “Microstructure and mechanical properties of a laser treated Al alloy,” *Acta Metall. Mater.*, vol. 41, no. 7, pp. 1989–1998, Jul. 1993.

[60] R. Labusch, “A Statistical Theory of Solid Solution Hardening,” *Phys. status solidi*, vol. 41, no. 2, pp. 659–669, 1970.

[61] C. Varvenne, G. P. M. Leyson, M. Ghazisaeidi, and W. A. Curtin, “Solute strengthening in

random alloys," *Acta Mater.*, vol. 124, pp. 660–683, Feb. 2017.

[62] I. Matsui, T. Uesugi, Y. Takigawa, and K. Higashi, "Effect of interstitial carbon on the mechanical properties of electrodeposited bulk nanocrystalline Ni," *Acta Mater.*, vol. 61, no. 9, pp. 3360–3369, May 2013.

[63] G. P. M. Leyson, W. A. Curtin, L. G. Hector, and C. F. Woodward, "Quantitative prediction of solute strengthening in aluminium alloys," *Nat. Mater.*, vol. 9, no. 9, pp. 750–755, Sep. 2010.

[64] G. P. M. Leyson, L. G. Hector, and W. A. Curtin, "Solute strengthening from first principles and application to aluminum alloys," *Acta Mater.*, vol. 60, no. 9, pp. 3873–3884, 2012.

[65] E. O. Hall, "The Deformation and Ageing of Mild Steel: III Discussion of Results," *Proc. Phys. Soc. Sect. B*, vol. 64, no. 9, pp. 747–753, Sep. 1951.

[66] N. J. Petch, "The cleavage strength of polycrystals," *J. Iron Steel InstInst*, vol. 174, no. 19, pp. 25–28, 1953.

[67] N. Hansen, "The effect of grain size and strain on the tensile flow stress of aluminium at room temperature," *Acta Metall.*, vol. 25, no. 8, pp. 863–869, Aug. 1977.

[68] N. Kamikawa, X. Huang, N. Tsuji, and N. Hansen, "Strengthening mechanisms in nanostructured high-purity aluminium deformed to high strain and annealed," *Acta Mater.*, vol. 57, no. 14, pp. 4198–4208, Aug. 2009.

[69] I. Matsui, S. Ono, Y. Hanaoka, T. Uesugi, Y. Takigawa, and K. Higashi, "Contribution of interstitial solute strengthening in aluminum," *Philos. Mag. Lett.*, vol. 94, no. 2, pp. 63–71, Feb. 2014.

[70] M. Dixit, R. S. Mishra, and K. K. Sankaran, "Structure–property correlations in Al 7050 and Al 7055 high-strength aluminum alloys," *Mater. Sci. Eng. A*, vol. 478, no. 1–2, pp. 163–

172, Apr. 2008.

[71] Ø. Ryen, O. Nijs, E. Sjölander, B. Holmedal, H. E. Ekström, and E. Nes, "Strengthening mechanisms in solid solution aluminum alloys," *Metall. Mater. Trans. A Phys. Metall. Mater. Sci.*, vol. 37, no. 6, pp. 1999–2006, 2006.

[72] E. Hornbogen and E. A. Starke, "Overview no. 102 Theory assisted design of high strength low alloy aluminum," *Acta Metall. Mater.*, vol. 41, no. 1, pp. 1–16, Jan. 1993.

[73] R. D. D. Vasudevan, Asuri K., *Aluminum Alloys--Contemporary Research and Applications*. Elsevier, 2012.

[74] W. D. Callister and D. G. Rethwisch, *Materials science and engineering: an introduction*, vol. 9. Wiley New York, 2018.

[75] Q. Guo *et al.*, "In-situ characterization and quantification of melt pool variation under constant input energy density in laser powder bed fusion additive manufacturing process," *Addit. Manuf.*, vol. 28, pp. 600–609, 2019.

[76] K. Zweiacker, "IN-SITU TEM INVESTIGATION OF RAPID SOLIDIFICATION OF ALUMINUM AND ALUMINUM COPPER ALLOYS," 2015.

[77] C. Liu, "in Situ Tem and Continuum Modeling of Laser-Induced Rapid Solidification of Aluminum and Aluminum Copper Alloys," 2017.

[78] J. M. K. Wiezorek, C. Liu, S. Farjami, K. W. Zweiacker, J. T. Mckeown, and G. H. Campbell, "Composition and Crystal Orientation Mapping of nano-scale multi-phase Rapid Solidification Microstructures in hypo-eutectic Al-Cu Alloy Thin Films," *Microsc. Microanal.*, vol. 23, no. S1, pp. 1078–1079, Jul. 2017.

[79] Y.-J. Liang, X. Cheng, and H.-M. Wang, "A new microsegregation model for rapid solidification multicomponent alloys and its application to single-crystal nickel-base

superalloys of laser rapid directional solidification," *Acta Mater.*, vol. 118, pp. 17–27, Oct. 2016.

[80] S. W. Youn, P. K. Seo, and C. G. Kang, "A study on nano-deformation behavior of rheo-formed Al–Si alloy based on depth-sensing indentation with three-dimensional surface analysis," *J. Mater. Process. Technol.*, vol. 162–163, pp. 260–266, May 2005.

[81] S. Nayak, L. Riester, and N. B. Dahotre, "Instrumented indentation probing of laser surface-refined cast Al alloy," *J. Mater. Res.*, vol. 19, no. 1, pp. 202–207, 2004.